JETP Letters, Vol. 79, No. 2, 2004, pp. 57–61. Translated from Pis'ma v Zhurnal Éksperimental'noĭ i Teoreticheskoĭ Fiziki, Vol. 79, No. 2, 2004, pp. 65–69.

Mixing Rules for Group Velocities in Nanocomposite Materials and Photonic Crystals

A. M. Zheltikov

International Laser Center, Physics Department, Moscow State University, Vorob'evy gory, Moscow, 119899 Russia

e-mail: zheltikov@top.phys.msu.su

Received December 3, 2003

Mixing rules for group velocities in nanocomposite materials with different architecture, including lamellar-inhomogeneous nanotextures, Maxwell Garnett structures, and one-dimensional photonic crystals, are derived and analyzed. The group velocity can be controlled for such composite structures by changing nanocrystal sizes and varying the dielectric properties and the content of the constituent materials. The interference of scattered waves in structures with a spatial scale of optical inhomogeneities comparable to the radiation wavelength gives rise to new physical phenomena that cannot be described in terms of the effective-medium approximation. © *2004 MAIK "Nauka/Interperiodica".*

PACS numbers: 42.65.Wi; 42.70.Qs

Nanocomposite materials open new unique opportunities in laser physics and optical technologies. Nanopowder materials in particular are at the heart of lasers [1] and optical frequency converters [2] of a new architecture. Nano- and mesoporous semiconductor materials can radically enhance nonlinear-optical interactions of laser pulses [3]. Photonic-crystal structures [4, 5] are intensely used to control radiative processes and are considered as promising candidates for the creation of a new generation of components and devices for telecommunications, laser physics, and nonlinear optics [6].

Many remarkable properties of nonlinear-optical interactions in nanocomposite materials are due to the local-field enhancement [7] and the possibility of tuning the effective refractive index of such materials by changing the dielectric properties, the content, and the sizes of nanoinclusions [3]. Recent experiments have demonstrated that nanocomposite materials offer much promise for nonlinear-optical frequency conversion of ultrashort pulses [2, 8]. Tunability of the group velocity is one of the key problems in femtosecond nanophotonics, which deals with the development of highly efficient and compact photonic devices for the control of ultrashort laser pulses based on nanocomposite materials. This work suggests strategies to solve this problem. We will derive and analyze mixing rules for group velocities in nanocomposite materials with different architecture, including lamellar nanotextures, Maxwell Garnett structures, and one-dimensional photonic crystals.

We start our analysis with a lamellar-inhomogeneous nanotexture (see the inset in Fig. 1). Nanocomposites of such an architecture consist of parallel nanosheets of material with a dielectric constant $\varepsilon_1 = n_1^2$ embedded in a medium with a dielectric constant $\varepsilon_2 = n_2^2$ (n_1 and n_2 are the refractive indices of the constituent materials). Optical properties of such a structure have been analyzed in the literature since the 19th century. Lord Rayleigh, in particular, has highlighted [9]

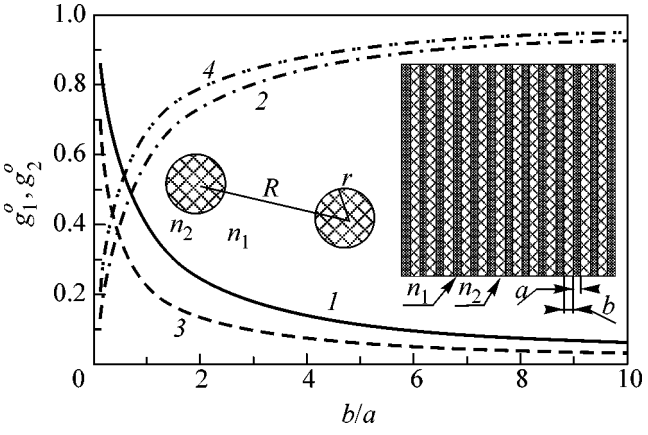

Fig. 1. The weight factors g_1^o (curves *1* and *3*) and g_2^o (curves *2* and *4*) for an ordinary wave in a lamellar-inhomogeneous nanocomposite material as functions of the ratio of layer thicknesses b/a. The ratio of the refractive indices of the layers forming the structure is $n_2/n_1 = 1.5$ (*1*, *2*) and 3.0 (*3*, *4*). The insets show different architectures of nanocomposite materials: a lamellar-inhomogeneous nanotexture (right) and a Maxwell Garnett nanocomposite (left).

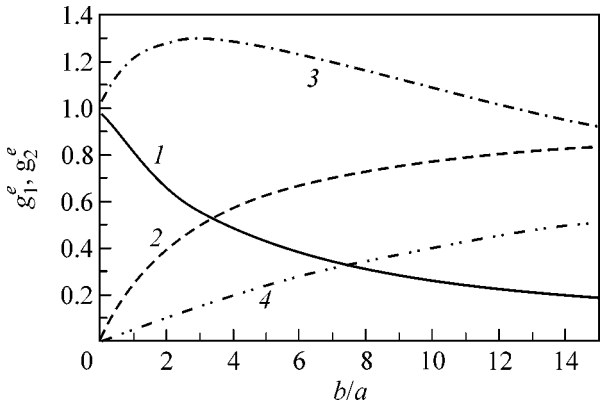

Fig. 2. The weight factors g_1^e (curves *1* and *3*) and g_2^e (curves *2* and *4*) for an extraordinary wave in a lamellar-inhomogeneous nanocomposite material as functions of the ratio of layer thicknesses b/a. The ratio of the refractive indices of the layers forming the structure is $n_2/n_1 = 1.5$ (*1*, *2*) and 3.0 (*3*, *4*).

a form birefringence of such a layered structure. As understood later, this form birefringence can be used to radically enhance nonlinear-optical processes in nanostructured materials [10] and multilayer waveguides [11] due to improved phase matching between the pump field and the nonlinear signal.

Assuming that $\omega n_1 a/c$, $\omega n_2 b/c \ll 1$, where ω is the radiation frequency and a and b are the thicknesses of alternating layers of isotropic materials with refractive indices n_1 and n_2, respectively, we can represent the effective refractive indices for ordinary and extraordinary waves in a periodic layered nanotexture shown in the inset to Fig. 1 as [12]

$$n_o^2 = \frac{a}{d}n_1^2 + \frac{b}{d}n_2^2, \tag{1}$$

$$\frac{1}{n_e^2} = \frac{a}{d}\frac{1}{n_1^2} + \frac{b}{d}\frac{1}{n_2^2}, \tag{2}$$

where $d = a + b$. Formulas (1) and (2) define the mixing rules for the refractive indices of the constituent materials in the case of ordinary and extraordinary waves in lamellar-inhomogeneous nanocomposites. To find the corresponding mixing rules for the group velocities of light pulses in such a nanostructure, we differentiate Eqs. (1) and (2) with respect to frequency. This operation yields

$$\frac{1}{v_o} = \frac{1}{d^{1/2}(an_1^2 + bn_2^2)^{1/2}}\left(\frac{an_1}{v_1} + \frac{bn_2}{v_2}\right), \tag{3}$$

$$\frac{1}{v_e} = \frac{d^{1/2}}{\left(\frac{a}{n_1^2} + \frac{b}{n_2^2}\right)^{3/2}}\left(\frac{a}{n_1^3}\frac{1}{v_1} + \frac{b}{n_2^3}\frac{1}{v_2}\right), \tag{4}$$

where $v_i = (\partial k_i/\partial\omega)^{-1}$ are the group velocities in the constituent materials ($i = 1, 2$).

In the limiting case of $n_1 = n_2$ and $v_1 = v_2 = v$, Eqs. (3) and (4) are reduced to the expressions for the group velocity of light in an isotropic medium: $v_o = v_e = v$. Generally, the group-velocity mixing rules for ordinary and extraordinary waves in a lamellar-inhomogeneous medium, as follows from Eqs. (3) and (4), can be written as

$$\frac{1}{v_{o,e}} = \frac{g_1^{o,e}}{v_1} + \frac{g_2^{o,e}}{v_2}. \tag{5}$$

The weight factors $g_i^{o,e}$ ($i = 1, 2$) in Eq. (5) depend only on the ratio b/a of layer thicknesses and the ratio n_2/n_1 of the refractive indices of the constituent materials. Figures 1 and 2 display the dependences of the weight factors $g_i^{o,e}$ for the ordinary and extraordinary waves in a lamellar-inhomogeneous material on the ratio b/a of layer thicknesses. For the ordinary wave (Fig. 1), the weight factors g_i^o are monotonic functions of the ratio b/a. The contribution of each of the materials to the group velocity of light in a nanocomposite monotonically decreases as the content of this material is reduced. In the case of the extraordinary wave (Fig. 2), the weight factors g_1^e may nonmonotonically depend on the ratio b/a. Analysis of Eqs. (4) and (5) shows that the factor g_1^e is a monotonic function of b/a for $n_2^2/n_1^2 < 3$ (curve *1* in Fig. 2). With $n_2^2/n_1^2 > 3$, this factor reaches its maximum (curve *3* in Fig. 2) at the following value of the ratio b/a:

$$\left(\frac{b}{a}\right)_{\max} = \frac{1}{2}\frac{n_2^2}{n_1^2} - \frac{3}{2}. \tag{6}$$

Thus, we found that the inverse effective group velocity in a nanotextured material can be represented as a sum of inverse group velocities in each of the materials, taken with weight factors controlled by the optical properties of materials forming the nanostructure and by the nanocomposite architecture. Such a mixing rule for group velocities is characteristic of effective-medium models. Strong coupling and interference of scattered waves, as will be shown below, lead to deviations from this mixing rule.

The Maxwell Garnett model [13] gives an effective dielectric constant of a nanocomposite structure (inset in Fig. 1) consisting of a material with dielectric constant $\varepsilon_1 = n_1^2$ with nanoscale spherical inclusions of a material with dielectric constant $\varepsilon_2 = n_2^2$ and volume filling fraction p. This model assumes that the distance

R between the nanoinclusions is much larger than their radius r, $R \gg r$ (see inset in Fig. 1). The Maxwell Garnett mixing rule for the dielectric constants in a nanocomposite material is written as

$$\varepsilon_{MG} = \varepsilon_1 + 3p\varepsilon_1\frac{\varepsilon_2 - \varepsilon_1}{\varepsilon_2 + 2\varepsilon_1}. \quad (7)$$

Differentiating Eq. (7) with respect to frequency, we arrive at the following mixing rule for the group velocities in the Maxwell Garnett model:

$$v_{MG}^{-1} = n^{-1}(n_2^2 + 2n_1^2)^{-2} \times\left\{[2((2-3p)n_1^4 + (1+3p)n_2^4 + 2(2-3p)n_1^2n_2^2]\frac{n_1}{v_1} + 9pn_1^4\frac{n_2}{v_2}\right\}. \quad (8)$$

Thus, similar to the case of a lamellar-inhomogeneous nanotexture, the inverse effective group velocity can be represented, within the framework of the Maxwell Garnett model, as a sum of weighted inverse group velocities of individual materials forming a nanostructure:

$$\frac{1}{v_{MG}} = \frac{g_1^{MG}}{v_1} + \frac{g_2^{MG}}{v_2}. \quad (9)$$

The ratio of weight factors in Eq. (9), $F_{MG}(p, n_2/n_1) = g_2^{MG}/g_1^{MG}$, is written as

$$F_{MG}\left(p, \frac{n_2}{n_1}\right) = \frac{9p}{2(2-3p) + (1+3p)\left(\frac{n_2}{n_1}\right)^4 + 2(2-3p)\left(\frac{n_2}{n_1}\right)^2}\frac{n_2}{n_1}. \quad (10)$$

Since p is small, the dependence of the factor F_{MG} on the volume filling fraction of nanoinclusions is close to a linear function. The dependence of F_{MG} on the ratio n_2/n_1 of refractive indices is nonmonotonic. For small n_2/n_1, the factor F_{MG} linearly increases with the growth in the ratio of refractive indices. The maximum value of F_{MG} is achieved, independently of p, at $n_2/n_1 = (2/3)^{1/2}$. For large ratios n_2/n_1, the refractive index and the group velocity in a nanocomposite material of this class tend to the following limiting values: $n = n_1(1 + 3p)^{1/2}$ and $v = v_1(1 + 3p)^{-1/2}$.

Photonic crystals [4–6] are materials where the refractive index is periodically modulated in one, two, or three dimensions on a characteristic spatial scale providing strong coupling of scattered electromagnetic waves. The electromagnetic radiation field has the form of Bloch waves in such structures. In the elementary case of an ideal one-dimensional photonic crystal equivalent to an infinite periodic stack of layers with refractive indices n_1 and n_2 and thicknesses a and b (see inset in Fig. 1), the Bloch wave number K meets the following dispersion relation:

$$\cos(Kd) = \cos\left(\frac{\omega}{c}n_1a\right)\cos\left(\frac{\omega}{c}n_1b\right) - \Delta\sin\left(\frac{\omega}{c}n_1a\right)\sin\left(\frac{\omega}{c}n_2b\right), \quad (11)$$

where $\Delta = (n_1^2 + n_2^2)/2n_1n_2$. Differentiating Eq. (11) with respect to frequency, we derive the mixing rule for group velocities in a one-dimensional photonic crystal:

$$\frac{1}{v_{PBG}} = \frac{g_1^{PBG}}{v_1} + \frac{g_2^{PBG}}{v_2}, \quad (12)$$

where

$$g_1^{PBG} = \frac{a}{d|\sin Kd|} \times\left[\sin\left(\frac{\omega}{c}n_1a\right)\cos\left(\frac{\omega}{c}n_2b\right) + \Delta\cos\left(\frac{\omega}{c}n_1a\right)\sin\left(\frac{\omega}{c}n_2b\right)\right], \quad (13)$$

$$g_2^{PBG} = \frac{b}{d|\sin Kd|} \times\left[\sin\left(\frac{\omega}{c}n_1a\right)\cos\left(\frac{\omega}{c}n_2b\right) + \Delta\cos\left(\frac{\omega}{c}n_1a\right)\sin\left(\frac{\omega}{c}n_2b\right)\right]. \quad (14)$$

In the limiting case of $\omega n_1a/c$, $\omega n_2a/c \ll 1$, Eqs. (12)–(14) yield formulas (1) and (2) for the effective group velocity in a lamellar-inhomogeneous medium. Generally, however, the mixing rule for group velocities in a photonic crystal, as follows from the comparison of Eqs. (1), (2) and (12)–(14), qualitatively differs from the mixing rules for group velocities in a lamellar-inhomogeneous nanotexture or a Maxwell Garnett nanocomposite. In contrast to effective-medium models corresponding to the electrostatic approximation, the mixing rule for group velocities in a one-dimensional photonic crystal explicitly involves the dependence on the radiation frequency (Fig. 3). The group velocity in a photonic crystal is controlled not only by the dispersion properties of each of the materials constituting the photonic crystal and the morphology of the nanostructure but also the dispersion of Bloch waves (inset in Fig. 3), which may radically differ from the dispersion of each of the constituent materials.

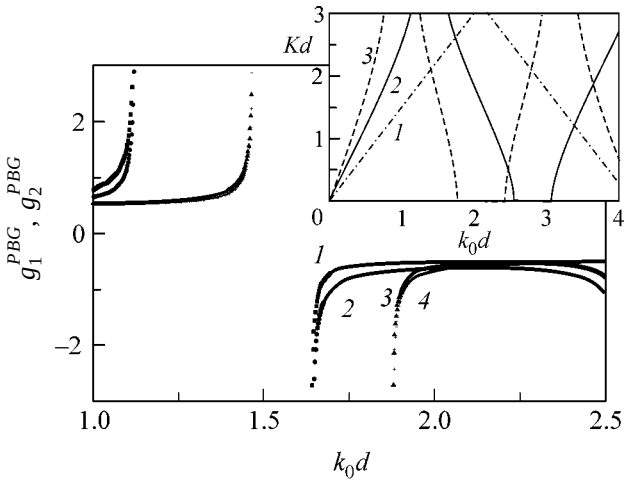

Fig. 3. The weight factors g_1^{PBG} (curves *1* and *3*) and g_2^{PBG} (curves *2* and *4*) as functions of the dimensionless frequency k_0d ($k_0 = \omega/c$) in a one-dimensional photonic crystal with layer thicknesses $a = b = 100$ nm and refractive indices $n_1 = 1.5$ and $n_2 = 2$ (*1*, *2*) and 1.5 (*3*, *4*). The inset shows the dispersion of a one-dimensional photonic crystal consisting of periodically alternating layers with equal thicknesses, $a = b$, and the ratio of refractive indices $n_2/n_1 = 1$ (*1*), 2 (*2*), and 3 (*3*).

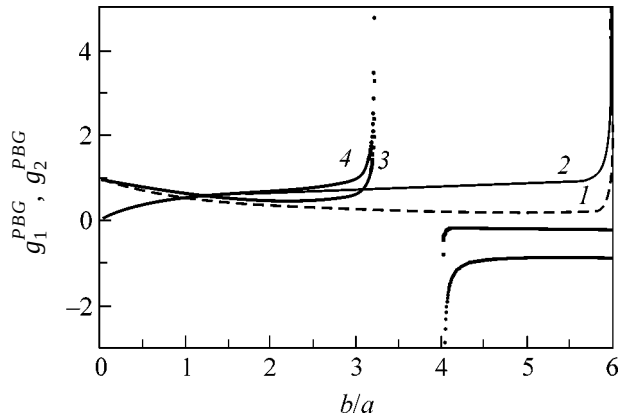

Fig. 4. The weight factors g_1^{PBG} (curves *1* and *3*) and g_2^{PBG} (curves *2* and *4*) in a one-dimensional photonic crystal as functions of the ratio of layer thicknesses b/a for a periodic multilayer structure with $a = 100$ nm, $n_1 = 1.5$, and $n_2 = 2.25$ (*1*, *2*) and 3.375 (*3*, *4*).

Physically, the difference between the mixing rules for group velocities in nanocomposite materials described in terms of the electrostatic effective-medium approximation and the mixing rules for photonic crystals originates from the interference of light waves scattered from refractive-index inhomogeneities. Such interference phenomena are especially pronounced around photonic band gaps of periodic structures, i.e., in the frequency ranges where the scattered waves are strongly coupled to the forward wave (inset in Fig. 3). One of the most prominent effects observed under these conditions is the lowering of the group velocity. Near the edges of photonic band gaps, at $Kd \longrightarrow \pi$, we have $v_{PBG} \longrightarrow 0$ (Figs. 3, 4). The group velocity in this regime is much lower than the group velocities in each of the materials. Such phenomena are never observed in lamellar-inhomogeneous media, where the spatial scale of refractive-index modulation is much lower than the radiation wavelength (cf. Figs. 1, 2, 4). The role of interference phenomena is insignificant in such materials, and their dispersion can be adequately described within the framework of effective-medium models (Eqs. (1), (2)). Inside photonic band gaps, the procedure of group-velocity calculation should be carefully modified. A comprehensive, methodologically consistent analysis of this issue is provided by Yariv and Yeh [12].

We have derived and analyzed the mixing rules for group velocities in nanocomposite materials with different architecture, including lamellar-inhomogeneous nanotextures, Maxwell Garnett structures, and one-dimensional photonic crystals. We have shown that the group velocity can be controlled for such nanocomposite structures by changing nanocrystal sizes and varying the dielectric properties and the content of the constituent materials. The interference of scattered waves in structures with a spatial scale of optical inhomogeneities comparable with the radiation wavelength gives rise to new physical phenomena that cannot be described in terms of the effective-medium approximation. Energy exchange between strongly coupled forward and reflected waves in photonic crystals may substantially lower the group velocity of electromagnetic radiation, giving rise to a strong local-field enhancement of nonlinear-optical interactions.

This work was supported in part by the President of Russian Federation (Grant MD-42.2003.02), the Russian Foundation for Basic Research (project nos. 02-02-17098 and 03-02-16929), and the Civilian Research and Development Foundation (project no. RP2-2558).

REFERENCES

1. N. M. Lawand, R. M. Balachandran, A. S. L. Gomes, and E. Sauvain, Nature **368**, 436 (1994).
2. S. O. Konorov, D. A. Sidorov-Biryukov, I. Bugar, *et al.*, Appl. Phys. B **78**, 73 (2004).
3. P. K. Kashkarov, L. A. Golovan, A. B. Fedotov, *et al.*, J. Opt. Soc. Am. B **19**, 2273 (2002).

4. J. D. Joannopoulos, R. D. Meade, and J. N. Winn, *Photonic Crystals: Molding the Flow of Light* (Princeton Univ. Press, Princeton, 1995).
5. K. Sakoda, *Optical Properties of Photonic Crystals* (Springer, Berlin, 2001).
6. *Nonlinear Optics of Photonic Crystals*, Ed. by C. M. Bowden and A. M. Zheltikov, Feature issue of J. Opt. Soc. Am. B **19** (9) (2002).
7. J. E. Sipe and R. W. Boyd, Phys. Rev. A **46**, 1614 (1992).
8. S. O. Konorov, A. B. Fedotov, A. A. Ivanov, *et al.*, Opt. Commun. **224**, 309 (2003).
9. Lord Rayleigh, Philos. Mag. **34**, 481 (1892).
10. L. A. Golovan, V. Yu. Timoshenko, A. B. Fedotov, *et al.*, Appl. Phys. B **73**, 31 (2001).
11. A. Fiore, V. Berger, E. Rosencher, *et al.*, Nature **391**, 463 (1998).
12. A. Yariv and P. Yeh, *Optical Waves in Crystals: Propagation and Control of Laser Radiation* (Wiley, New York, 1984; Mir, Moscow, 1987).
13. J. C. Maxwell Garnett, Philos. Trans. R. Soc. London **203**, 385 (1904).

Translated by A. Zheltikov

JETP Letters, Vol. 79, No. 2, 2004, pp. 62–65. Translated from Pis'ma v Zhurnal Éksperimental'noĭ i Teoreticheskoĭ Fiziki, Vol. 79, No. 2, 2004, pp. 70–74.

Localization of Light Energy on the Nanometer Scale in a Silicon Cone

T. I. Kuznetsova* and V. S. Lebedev**

Lebedev Physical Institute, Russian Academy of Sciences, Leninskiĭ pr. 53, Moscow, 119991 Russia

**e-mail: tkuzn@sci.lebedev.ru*

***e-mail: vlebedev@sci.lebedev.ru*

Received October 27, 2003; in final form, December 9, 2003

The spatial structure of light fields in a metallized cone filled with a medium with complex dielectric function was studied on the basis of the exact solution of the eigenwave problem. It is suggested that silicon can be used as a core of optical probe in the visible spectral region. It is shown that the density of light energy at the output of optical probe can be drastically increased if silicon is used instead of glass fiber. © *2004 MAIK "Nauka/Interperiodica".*

PACS numbers: 42.81.Qb; 42.81.Dp

The generation of highly localized light fields has provided the basis for optical studies with subwavelength resolution and for local action on the matter. Using the light concentrated on the subwavelength scale, it has been possible to go far beyond the classical diffraction restrictions in many directions of the optical experiment [1–7].

The use of a tapered metal-coated glass fiber is the most popular way of producing highly localized fields (see [8] and literature cited therein). Another type of optical probe is based on the scattering of an external radiation by metallic needle (see, e.g., [9]). A drawback of the scattering probe consists in a high level of the background light. On the other hand, the output radiation intensity in the case of glass fiber is not sufficiently high (because of the low probe transmittance).

Much work has been devoted to improving the transmittance of tapered optical waveguides (see, e.g., [10–16]). Several approaches to the solution of this problem have been proposed. It was suggested, e.g., that the waveguide fields should be transformed into surface plasmon modes more efficiently, that the taper angles should be increased, and that the profile of the probe should be optimized near its apex. Recently, the tendency to use probe materials with a high refractive index has been envisaged. In this respect, silicon attracts particular attention. The merits (compared to glass) of using silicon (having a high refractive index) in the infrared region were pointed out in [14]. Experimental works [15, 16] with silicon were also made only in the infrared spectral region.

The possibility of using silicon in the visible region has not even been discussed to date. The problem is that the absorption is strong in this spectral region. However, it is not clear, in advance, whether it is possible to obtain high output intensity in the presence of strong absorption in a medium with high refractive index or not. The purpose of this work is to answer this question.

Let us consider a cone with ideally reflecting walls. The dielectric function of a medium in the cone is $\varepsilon = \varepsilon' + i\varepsilon''$ and its magnetic permeability is $\mu = 1$. In the calculations, we will use material constants corresponding to silicon. For the case of a real dielectric constant, the expressions for the cone eigenwaves of the electric and magnetic types with arbitrary mode indices are given in [12]; the corresponding bibliography is also given in that work. In the case of complex dielectric function, we restrict ourselves only to the azimuthally symmetric electric wave. A monochromatic wave with frequency $\omega = 2\pi c/\lambda$ is considered, where c is the speed of light and λ is the wavelength in vacuum. In the spherical system of coordinates (r is the distance from the cone apex and θ and φ are the polar and azimuthal angles, respectively), the solution to the Maxwell equations for the TM wave, i.e., for the electric wave, in the case of $\partial/\partial\varphi = 0$ has only three nonzero components E_r, E_θ, and H_φ:

$$E_r = \frac{\nu(\nu+1)}{r^2}\mathcal{R}(r)P_\nu(\cos\theta),$$
$$E_\theta = \frac{1}{r}\frac{\partial\mathcal{R}(r)}{\partial r}\frac{\partial P_\nu(\cos\theta)}{\partial\theta}, \quad (1)$$

$$H_\varphi = i\frac{\omega(\varepsilon' + i\varepsilon'')}{c}\frac{1}{r}\mathcal{R}(r)\frac{\partial P_\nu(\cos\theta)}{\partial\theta}. \quad (2)$$

0021-3640/04/7902-0062$26.00 © 2004 MAIK "Nauka/Interperiodica"

Here, $P_\nu(\cos\theta)$ is the ν-degree Legendre function of the first kind. The radial dependence of fields is described by the function

$$\mathcal{R}(r) = Crj_\nu(kr), \tag{3}$$

where C is an arbitrary constant, $j_\nu(z)$ is the Bessel spherical function of the first kind with complex argument z and noninteger index ν, and k is the wavenumber

$$k = \sqrt{\varepsilon' + i\varepsilon''}(\omega/c), \quad \sqrt{\varepsilon' + i\varepsilon''} = n + i\kappa. \tag{4}$$

The boundary condition at the cone walls is $P_\nu(\cos\theta_0) = 0$, where $2\theta_0$ is the cone angle. This condition defines the set of eigenvalues $\nu_s(\theta_0)$ ($s = 1, 2, \ldots$); we consider below the wave corresponding to the lowest eigenvalue. The Bessel function of the first kind is chosen in Eq. (3) because the field is almost totally reflected from the aperture of subwavelength size. For this reason, the solution for a closed cone describes, with a good accuracy, the field structure in a frustrum of a cone tapered to subwavelength sizes [12].

The formulas for field components (1) and (2) can be used to calculate the time-averaged energy density for each component; the corresponding values are given by the expressions [17]

$$w_r = \frac{1}{16\pi}\frac{d(\omega\varepsilon')}{d\omega}|E_r|^2, \quad w_\theta = \frac{1}{16\pi}\frac{d(\omega\varepsilon')}{d\omega}|E_\theta|^2, \quad w_\varphi = \frac{1}{16\pi}\frac{d(\omega\mu')}{d\omega}|H_\varphi|^2, \tag{5}$$

where $\varepsilon' = \mathrm{Re}\{\varepsilon\}$ and $\mu' = \mathrm{Re}\{\mu\}$. To determine the transmittance for a tapered optical waveguide, one should evaluate the integrals of w_r, w_θ, and w_φ over the sphere surface area $2\pi r^2\sin\theta d\theta$ with radius r inside the cone ($0 \le \theta \le \theta_0$, $0 \le \varphi \le 2\pi$). The resulting expressions for the integrated electric $W_{el} = W_r + W_\theta$ and magnetic $W_m = W_\varphi$ energy densities are given by

$$W_{el} = \frac{|C|^2}{8}\frac{d(\omega\varepsilon')}{d\omega}\nu(\nu+1)\mathcal{J}_\nu^{(1)}(\theta_0) \times\left[\nu(\nu+1)|j_\nu(kr)|^2 + \left|\frac{\partial[rj_\nu(kr)]}{\partial r}\right|^2\right], \tag{6}$$

$$W_m = \frac{|C|^2|\varepsilon' + i\varepsilon''|}{8}\left(\frac{\omega r}{c}\right)^2\mathcal{J}_\nu^{(2)}(\theta_0)|j_\nu(kr)|^2, \tag{7}$$

$$\mathcal{J}_\nu^{(1)} = \int_0^{\theta_0}[P_\nu(\cos\theta)]^2\sin\theta d\theta, \quad \mathcal{J}_\nu^{(2)} = \int_0^{\theta_0}\left[\frac{\partial P_\nu(\cos\theta)}{\partial\theta}\right]^2\sin\theta d\theta, \tag{8}$$

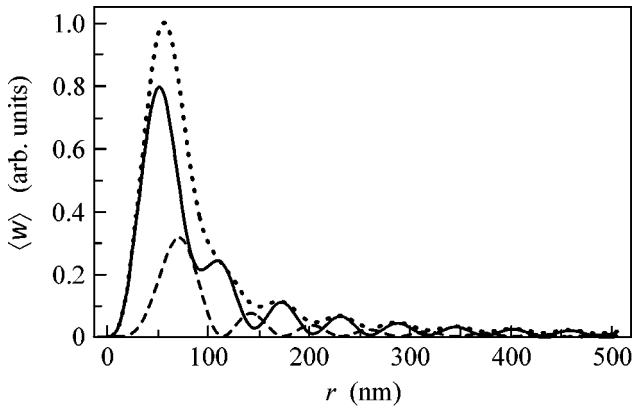

Fig. 1. Polar-angle-averaged field energy density as a function of coordinate r in a Si cone with the apex angle $2\theta_0 = \pi/2$. The solid and dashed curves are, respectively, the contributions from the electric $\langle w_{el}\rangle$ and magnetic $\langle w_m\rangle$ energies of the lowest-index TM wave at $\lambda = 488$ nm. The dotted curve is the total energy density $\langle w_{tot}\rangle = \langle w_{el}\rangle + \langle w_m\rangle$.

with $\mathcal{J}_\nu^{(2)} = \nu(\nu+1)\mathcal{J}_\nu^{(1)}$. By summing expressions (6) and (7), one can obtain the total integrated field energy density $W_{tot} = W_{el} + W_m$ inside the cone.

Let us consider the spatial distribution of electromagnetic energy inside a silicon conical waveguide. In Fig. 1, the calculated energy densities of (solid line) electric $\langle w_{el}\rangle$ and (dashed line) magnetic $\langle w_m\rangle$ field components are shown as functions of the radial coordinate r for $\lambda = 488$ nm. The results are averaged over the polar angle θ and calculated for a cone with apex angle $2\theta_0 = \pi/2$ ($\nu = 2.548$). One can see in Fig. 1 that the energy densities of the electric and magnetic field components show oscillatory behavior at distances r larger than the light wavelength $\lambda_{Si} = \lambda/n_{Si}$ in Si ($n_{Si} = 4.37$ for $\lambda = 488$ nm) and are in antiphase. In the region $r \ll \lambda_{Si}$, both $\langle w_{el}\rangle$ and $\langle w_m\rangle$ decrease rapidly as the cone apex is approached, but the energy density of electric field decreases considerably slower than for the magnetic field. Figure 1 also shows the radial dependence of the θ-averaged total energy density $\langle w_{tot}\rangle = \langle w_{el}\rangle + \langle w_m\rangle$ of the electric and magnetic fields (dotted line). One can see that $\langle w_{tot}\rangle$ has a sharp peak as a function of r before decreasing near the cone apex; i.e., light energy is strongly concentrated.

Let us now consider the transmittance T of a silicon waveguide. The transmission will be determined from the field in near zone. In our case, the transmittance is defined by the ratio $T = W_{tot}^{out}/W_{tot}^{in}$ of the field energy density (integrated over the plane surface of an aperture with radius a) $W_{tot}^{out} \equiv W_{tot}(z_0)$ at the output $z = z_0$ of the frustrum of the cone,

$$W_{tot}^{out} = 2\pi\int_0^a w_{tot}(\rho, z_0)\rho d\rho, \quad a = z_0\tan\theta_0, \tag{9}$$

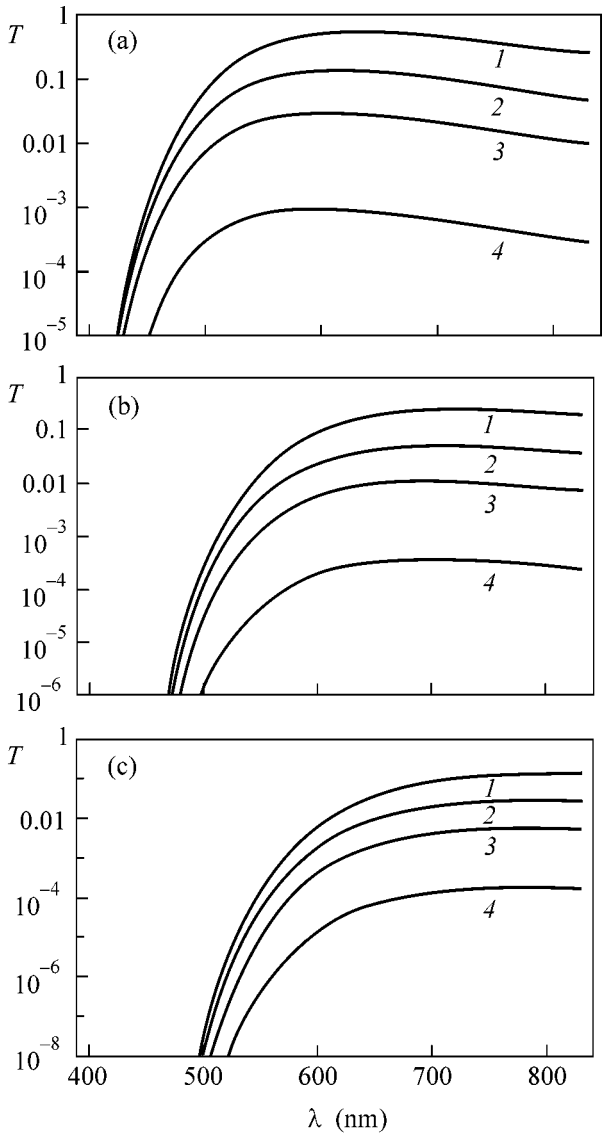

Fig. 2. Spectral dependences for the ratio $T = W_{tot}^{out}/W_{tot}^{in}$ of the integrated energy density of the lowest-index TM wave at the output (Eq. 9) of a conical Si waveguide to the corresponding value at its input (Eq. 10). Panels (a), (b), and (c) correspond, respectively, to the distances r_{in} = 2, 5, and 10 μm from the cone apex with the angle $2\theta_0 = \pi/2$ to the waveguide input. Curves *1*, *2*, *3*, and *4* correspond, respectively, to the diameter d = 100, 70, 50, and 25 nm of the output aperture.

to the total integrated energy density W_{tot}^{in} at the waveguide input

$$W_{tot}^{in} = \alpha 2\pi r^2 \int_0^{\theta_0} w_{tot} \sin\theta d\theta, \qquad (10)$$

$$\alpha = \frac{1}{1 + \exp(-4\kappa\omega r_{in}/c)}.$$

Integration in Eq. (10) goes over the section of spherical surface inside the cone ($0 \le \theta \le \theta_0$, $0 \le \varphi \le 2\pi$) at $r = r_{in}$ (r_{in} is the distance from the cone apex to the waveguide input). The factor α allows for the fact that the input field is a superposition of two counterpropagating traveling waves with amplitudes whose ratio at large distances $r \gg 1/|k|$ from the apex is $\exp(-2\kappa\omega r/c)$. The factor α ($1/2 \le \alpha \le 1$) takes into account the fraction corresponding to the incident wave in the integrated energy density $W_{tot}(r_{in})$ and eliminates the contribution from the reflected wave.

The calculated $T(\lambda)$ dependences are shown in Fig. 2 for r_{in} = 2, 5, and 10 μm in a Si cone with the apex angle $2\theta_0 = \pi/2$. Curves *1*, *2*, *3*, and *4* correspond, respectively, to the diameters d = 100, 70, 50, and 25 nm of the output aperture. According to [18], the refractive index n of light in Si increases monotonically from 3.67 to 5.57 for the wavelengths λ varying from 830 to 400 nm, while the damping coefficient κ increases from 0.005 to 0.387. Therefore, light absorption in Si is rather weak in the near-infrared region. However, it becomes significant in the short-wavelength part of the visible spectrum and results in a drastic decrease in the light transmittance at small λ.

The comparison of Figs. 2a, 2b, and 2c for each value of λ indicates that the transmittance $T(\lambda)$ in a Si cone decreases with increasing the waveguide length r_{in} (contrary to glass fiber [12]). This dependence is relatively weak in the IR region and becomes rather sharp in the short-wavelength part of the visible spectrum. For instance, the transmittance at λ < 500 nm is reduced by several orders of magnitude upon increasing the waveguide length r_{in} from 2 to 10 μm.

One can conclude from the analysis of the above results that the transmittance of a Si optical waveguide is high in both the near IR and visible spectral regions (provided that the waveguide length r_{in} is not too large). For example, one has for λ = 830 nm, taper angle $2\theta_0 = \pi/2$, and r_{in} = 2 μm, $T = 2.9 \times 10^{-4}$, 9.3×10^{-3}, and 4.7×10^{-2} for the diameter of output aperture d = 25, 50, and 70 nm, respectively. Note that the values $T \sim 10^{-2}$ obtained for d = 50–70 nm are in fair agreement with recent measurements [16] of the transmittance of a metallized Si waveguide at λ = 830 nm. In the visible region at a He–Ne laser wavelength (λ = 633 nm), the transmittance increases by one or two orders of magnitude compared to glass fiber; $T = 9.2 \times 10^{-4}$, 2.7×10^{-2}, and 1.2×10^{-1} for the diameters d = 25, 50, and 70 nm, respectively, and for the same angle θ_0 and waveguide length r_{in}. For the Ar^+ laser wavelength (λ = 488 nm), one obtains, in spite of a drastic increase in light absorption in Si, $T = 1.8 \times 10^{-4}$, 4.2×10^{-3}, and 1.5×10^{-2}, respectively, for the same d values. It is significant that all these values sizably exceed the corresponding values of T for a metal-coated tapered glass fiber waveguide.

The results obtained suggest that the use of silicon as a probe material is favorable for obtaining high transmittance not only in the IR but also in the visible spectral region. In particular, the transmittance maximum for a probe length of 2 μm occurs not in the IR region but near $\lambda = 600$ nm.

The properties of waveguides with the silicon core are determined by the competition between two opposite tendencies. A high refractive index reduces the potential barrier for the light wave and favors field leakage through the narrow waveguide section near the output. At the same time, the absorption weakens the field at the input section and, hence, reduces the overall transmittance. Due to the strong spectral dependence of the absorption coefficient and refractive index, the situation becomes different in different wavelength regions. For instance, light absorption in the near-IR region only weakly affects the transmittance of a tapered waveguide, so that, when used in probes, silicon invariably offers an advantage over glass.

In the visible spectral region, the results prove to be highly sensitive to the length of the Si waveguide. For short lengths, the benefits of using silicon become obvious. For example, if the waveguide length does not exceed 2 μm and the diameter of the output aperture is $d = 50$ nm, the transmittance at $\lambda = 633$ nm increases by a factor of 45 as compared to glass fiber.

The main conclusion of this work is that the role of refraction dominates over the absorption in the case of appropriate (and, what is important, realistic) geometric parameters. The use of Si as a core of a waveguide used in near-field microscopy allows simultaneous achievement of high transmittance in visible region and high spatial resolution.

We are grateful to A.G. Vitukhnovskiĭ for discussion. This work was supported by the scientific program “Optical Spectroscopy and Frequency Standards” of the Russian Academy of Sciences and by the Russian Foundation for Basic Research, project no. 02-02-16274.

REFERENCES

1. B. Sick, B. Hecht, and L. Novotny, Phys. Rev. Lett. **85**, 4482 (2000).
2. B. Hecht, H. Bielefeldt, L. Novotny, *et al.*, Phys. Rev. Lett. **77**, 1889 (1996).
3. E. J. Sánchez, L. Novotny, and X. S. Xie, Phys. Rev. Lett. **82**, 4014 (1999).
4. A. Hartschuh, E. J. Sánchez, X. S. Xie, and L. Novotny, Phys. Rev. Lett. **90**, 095503 (2003).
5. A. Bouhelier, M. Beversluis, A. Hartschuh, and L. Novotny, Phys. Rev. Lett. **90**, 013903 (2003).
6. P. C. Chaumet, A. Rahmani, and M. Nieto-Vesperinas, Phys. Rev. Lett. **88**, 123601 (2002).
7. S. M. Huang, M. H. Hong, Y. F. Lu, *et al.*, J. Appl. Phys. **91**, 3268 (2002).
8. E. Betzig, J. K. Trautman, T. D. Harris, *et al.*, Science **251**, 1468 (1991).
9. Y. Inouye and S. Kawata, Opt. Lett. **19**, 159 (1994).
10. L. Novotny, D. W. Pohl, and B. Hecht, Opt. Lett. **20**, 970 (1995).
11. B. Knoll and F. Keilmann, Opt. Commun. **162**, 177 (1999).
12. T. I. Kuznetsova and V. S. Lebedev, Kvantovaya Élektron. (Moscow) **32**, 727 (2002); Kvantovaya Élektron. (Moscow) **33**, 931 (2003).
13. A. Naber, D. Molenda, U. C. Fischer, *et al.*, Phys. Rev. Lett. **89**, 210801 (2002).
14. A. Castiaux, H. U. Danzebrink, and X. Bouju, J. Appl. Phys. **84**, 52 (1998).
15. T. Dziomba, H. U. Danzebrink, C. Lehrer, *et al.*, J. Microsc. **202**, 22 (2001).
16. T. Yatsui, K. Isumi, M. Kourogi, and M. Ohtsu, Appl. Phys. Lett. **80**, 2257 (2002).
17. L. D. Landau and E. M. Lifshitz, *Course of Theoretical Physics*, Vol. 8: *Electrodynamics of Continuous Media*, 2nd ed. (Nauka, Moscow, 1982; Pergamon, Oxford, 1984).
18. D. E. Aspnes and A. A. Studna, Phys. Rev. B **27**, 985 (1983).

Translated by V. Sakun

JETP Letters, Vol. 79, No. 2, 2004, pp. 66–70. Translated from Pis'ma v Zhurnal Éksperimental'noĭ i Teoreticheskoĭ Fiziki, Vol. 79, No. 2, 2004, pp. 75–79.

Generalized Dark States in the System "Bose Atoms and Quantized Field"

A. V. Taĭchenachev[1], A. M. Tumaĭkin[1], and V. I. Yudin[2]

[1] *Novosibirsk State University, ul. Pirogova 2, Novosibirsk, 630090 Russia*
e-mail: llf@admin.nsu.ru

[2] *Institute of Laser Physics, Siberian Division, Russian Academy of Sciences, pr. Lavrent'eva 13/3, Novosibirsk, 630090 Russia*
e-mail: llf@laser.nsc.ru

Received December 23, 2003

Three new classes of dark states describing the coherent population trapping effect in a quantum system of resonantly interacting Bose atoms and electromagnetic field are presented. © *2004 MAIK "Nauka/Interperiodica".*

PACS numbers: 32.80.Qk; 42.50.Ct

1. Coherent population trapping (CPT) in the atomic interaction with a resonant external field is a well-known phenomenon (see review [1] and literature cited therein). It is widely used in various fields of atomic and laser physics, such as ultrahigh-resolution spectroscopy [2], nonlinear optics of resonant media [3, 4], laser cooling [5], and atomic optics and interference [6]. For the resonant excitation from the atomic ground state with angular-momentum degeneracy, general conditions for the occurrence of CPT and the explicit form of dark light-nonscattering states were established in our works [7]. The external field was assumed to be coherent, and the atomic state was taken in the form of *c*-numeral amplitudes of wave-function expansion in the basis of magnetic sublevels.

It was shown in [8] that the laser-field fluctuations of a certain type destruct the dark state, and the CPT effect disappears. This rule, however, is not general. For instance, we have found in [9] that the dark state can arise upon the interaction with an arbitrarily fluctuating monochromatic radiation field. In particular, it has been shown that, for an atom with the ground-state angular momentum $J_g = 1$ and $J_e = 1$ in the excited state, the CPT effect occurs even if the photon spin coherence is fully absent (unpolarized light).

Recent remarkable theoretical works on the problem of dark polariton [10, 11] and the experimental demonstration of the fact that light-carried information is stored in an atomic medium [12] have rekindled our interest in the problem of the general form of dark state in the system atoms + field. It should be noted that the experimental results obtained in [12] seem to be highly important because of their possible extension to the storage of essentially quantum information coded in the nonclassical states of electromagnetic field. In this connection, the following statement of the problem seems to be quite appropriate: how do the conditions for the existence and the form of dark states change [7] if the resonant field is described not by *c*-numeral amplitudes but by the creation and annihilation operators? From this point of view, dark polaritons [11] should represent a special case of the general solution for which one field polarization mode is classical (i.e., is in the coherent state), while another is quantal. Moreover, it is quite possible that, for the long-term storage of quantum information in an atomic medium, it will be necessary to use ultracold atomic ensembles (Bose–Einstein condensates) [13]. In this case, atoms can conveniently be described by the secondary quantized amplitudes—Bose-type creation and annihilation operators [14].

Although we do not intend to solve this problem in the general form, we present in this work three new classes of dark states in a system "Bose atoms + quantized field."

2. Let us consider an ensemble of Bose atoms having two degenerate energy levels with the total angular momenta J_g in the ground state and J_e in the excited state and interacting resonantly with the quantized mode of a monochromatic electromagnetic field. The field spatial distribution in the mode is assumed to be independent of the field polarization (e.g., plane traveling wave); i.e., the field operator can be written in the form

$$\hat{\mathbf{E}}(\mathbf{r}) = \varphi(\mathbf{r})\hat{\mathbf{a}} + \text{h.c.}; \quad \hat{\mathbf{a}} = \sum_{s=\pm 1} \hat{a}_s \mathbf{e}_s, \qquad (1)$$

where $\varphi(\mathbf{r})$ is the field distribution in the mode and $\hat{a}_s$ is the photon annihilation operator in a mode with polarization $\mathbf{e}_s$ ($[\hat{a}_s, \hat{a}_{s'}^\dagger] = \delta_{ss'}$).

Atoms will be described within the framework of the secondary quantization method by the creation $\hat{b}^{\dagger}_{J_n\mu_n}(p_n)$ and annihilation $\hat{b}_{J_n\mu_n}(p_n)$ Bose operators for an atom in the state with energy $E_n(p_n)$, angular momentum J_n, and its projection μ_n, where $n = e, g$. As in the case of field, it is assumed that the wave functions $\psi_{p_n}(\mathbf{r})$ describe the spatial distribution of the probability amplitude in a stationary state with energy $E_n(p_n)$ and do not depend on the projection μ_n of angular momentum. Thus, we are dealing, e.g., with atoms in a free space (in this case, p_n corresponds to the atomic momentum) or with atoms in an isotropic nonresonant optical potential (in this case, the numbers p_n label energy levels) but not with atoms in a magnetic trap.

The excited atomic state is radiatively unstable because of its interaction with the field vacuum modes. The problem is to determine a nontrivial superposition that describes the ground-state atoms and the field-mode excitations and turns to zero the operator (1) of resonant interaction with field at every instant t. Formally, these conditions can be written as

$$\hat{\mathcal{N}}_e|NC\rangle = 0, \quad \hat{H}_{A-F}|NC\rangle = 0; \tag{2}$$

i.e., the dark state is simultaneously an eigenvector with zero eigenvalue for two operators: the operator of the number of excited atoms,

$$\hat{\mathcal{N}}_e = \sum_{p_e,\,\mu_e} \hat{b}^{\dagger}_{J_e\mu_e}(p_e)\hat{b}_{J_e\mu_e}(p_e), \tag{3}$$

and the operator of resonant interaction in the Dirac picture,

$$\hat{H}_{A-F}(t)$$

$$= \sum_{p_e,\,p_g} \exp\{-i\omega t + i[E_e(p_e) - E_g(p_g)]t/\hbar\}R(p_e, p_g) \tag{4}$$

$$\times \langle J_e||d||J_g\rangle \sum_{\mu_g,\,\mu_e,\,s} C^{J_e\mu_e}_{J_g\mu_g 1s}\hat{b}^{\dagger}_{J_e\mu_e}(p_e)\hat{a}_s\hat{b}_{J_g\mu_g}(p_g) + \text{h.c.}$$

Here, the overlap integral $R(p_e, p_g) = \int\psi^*_{p_e}(\mathbf{r})\varphi(\mathbf{r})\varphi_{p_g}(\mathbf{r})d^3r$ describes the photon-absorption recoil effect; $\langle J_e||d||J_g\rangle$ is the reduced matrix element of the dipole moment operator; and $C^{J_e\mu_e}_{J_g\mu_g 1\mu}$ are the Clebsch–Gordan coefficients [15].

For a more compact invariant presentation of the results, it is convenient to discard (for a while) the condition that photons are transverse, i.e., extend the summation over polarizations to three components ($\mu = 0, \pm 1$), omit, for brevity, the indices p_e and p_g, and pass to the effective spin Hamiltonian

$$\hat{H}_{A-F} = \hbar\kappa\sum_{(\mu)} C^{J_e\mu_e}_{J_g\mu_g 1\mu}\hat{b}^{\dagger}_{J_e\mu_e}\hat{a}_{\mu}\hat{b}_{J_g\mu_g} + \text{h.c.}, \tag{5}$$

where κ is the effective coupling constant (one-photon Rabi frequency). In so doing, one should bear in mind that the solutions obtained below to problem (2) are independent of p_e and have the same form for any p_g (i.e., they are not selective to the translational degrees of freedom). It is worth noting that the spin model corresponding to Hamiltonian (5) is also of importance because, in particular, it is isomorphic, in the resonant approximation, with some interaction models describing the nondegenerate n-level atomic systems with a multifrequency radiation field.

3. So, we seek the generalized dark states that represent the nontrivial solutions to problem (2) with the interaction Hamiltonian (5). The first class of such states corresponds to the $J \longrightarrow J$ (J is an integer) and $J \longrightarrow J - 1$ transitions and is a direct generalization of the dark states in a classical external field [7]. To describe it, we introduce the creation operator for an atom in the dark state

$$\hat{\Psi}^{\dagger}_{NC} = \sum_{\mu_g}\hat{\psi}_{J_g\mu_g}(\hat{\mathbf{a}})\hat{b}^{\dagger}_{J_g\mu_g}, \tag{6}$$

where the operator coefficients $\hat{\psi}_{J_g\mu_g}(\hat{\mathbf{a}})$ (components of the irreducible tensor of rank J_g) are the solutions to the system of equations

$$\{\hat{\psi}_{J_g}(\hat{\mathbf{a}}) \otimes \hat{\mathbf{a}}\}_{J_e\mu_e} = 0. \tag{7}$$

Here, the standard notation from [15] is used for the irreducible tensor product. Since the system of Eqs. (7) does not contain noncommuting operators, its solutions can be found by the methods developed in [7]. For the two aforementioned types of transitions, the nontrivial solutions have the form of homogeneous polynomials in the photon annihilation operators $\hat{\mathbf{a}}$. Namely, for the $J \longrightarrow J$ transitions (J is an integer), the solution has the form of a polynomial of (minimal) degree J:

$$\hat{\psi}_J = \{\hat{\mathbf{a}}\}_J; \quad \{\hat{\mathbf{a}}\}_L = \{\hat{\mathbf{a}} \otimes \{\hat{\mathbf{a}}\}_{L-1}\}_L; \quad \{\hat{\mathbf{a}}\}_1 \equiv \hat{\mathbf{a}}. \tag{8}$$

For the $J \longrightarrow J - 1$ transitions, the minimal degree is $(2J - 1)$ (we assume that, in the general case, all three components of the operator $\hat{\mathbf{a}}$ are nonzero). The solution has the form of superposition

$$\hat{\psi}_J = \sum_{L=0(1)}^{2J-1} A_L(\hat{\mathbf{a}}\cdot\hat{\mathbf{a}})^{(2J-1-L)/2}\{Q_J \otimes \{\hat{\mathbf{a}}\}_L\}_J, \tag{9}$$

where the summation goes over the even or odd L, depending on whether J is a half-integer number or an

integer;[1] Q_J is an arbitrary *c*-numeral irreducible tensor of rank J; and the coefficients are

$$A_L = (\sqrt{2})^L \frac{(2L+1)!!}{\sqrt{(2L)!}} \sqrt{\frac{(2J)!(2J+1)!}{(2J-L)!(2J+L+1)!}}.$$

Polynomials (9) form a two-dimensional linear space in the following sense: two linearly independent tensors $Q_J^{(1)}$ and $Q_J^{(2)}$ give two linearly independent solutions $\hat{\psi}_J^{(1)}$ and $\hat{\psi}_J^{(2)}$; any three solutions $\hat{\psi}_J^{(1)}$, $\hat{\psi}_J^{(2)}$, and $\hat{\psi}_J^{(3)}$ are linearly dependent. This is a direct consequence of the fact that the subspace of dark states for the $J \longrightarrow J-1$ transitions is two-dimensional in the classical case [7].

The basis state in the first class can be parameterized by two arbitrary functions f and F:

$$|NC(f,F)\rangle = f(\hat{\Psi}_{NC}^{\dagger})F(\hat{\mathbf{a}}^{\dagger})|\text{vac}\rangle, \qquad (10)$$

where $|\text{vac}\rangle$ is the vacuum state without atoms and photons. One can verify, after the direct substitution, that Eq. (10) is the solution to problem (2) if $\hat{\psi}_{J_g}$ satisfies Eq. (7). Note that, if the function F depends only on $\hat{a}_{-1}$ and $\hat{a}_{+1}$, the condition that photons are transverse will automatically be fulfilled. Evidently, any superposition and incoherent combination of states (10) are also solutions to problem (2); i.e., they are the dark states.

Let us take the simplest example to follow how a singly excited state of a dark polariton [11] arises in our approach. Consider the $1 \longrightarrow 1$ transition; i.e., $\hat{\Psi}_{NC} = \hat{a}_{+1}\hat{b}_{+1}^{\dagger} + \hat{a}_0\hat{b}_0^{\dagger} + \hat{a}_{-1}\hat{b}_{-1}^{\dagger}$. The function $F(\hat{\mathbf{a}})$ is defined as $F = \exp[-|z|^2/2 + z\hat{a}_{+1}^{\dagger}]\hat{a}_{-1}^{\dagger}$. When acting on the vacuum state, F generates a coherent state with amplitude z in the mode with circular polarization (+1) and a single photon in the mode with circular polarization (–1). Assume that the number of atoms is fixed and equal to N; then, the function f is determined unambiguously: $f = (\hat{\Psi}_{NC}^{\dagger})^N/\sqrt{N!}$. The direct calculations by formula (10) yield the result that coincides (except for notation) with $|D, 1\rangle$ in [11]:

$$|NC\rangle = (z|\{N\}_{+1}^{(a)}, \{0\}_{-1}^{(a)}, \{1\}_{-1}^{(ph)}\rangle + \sqrt{N}|\{N-1\}_{+1}^{(a)}, \{1\}_{-1}^{(a)}, \{0\}_{-1}^{(ph)}\rangle)/\sqrt{|z|^2+N},$$

where only those occupation numbers are indicated that change in the course of interaction; $\{N\}_{+1}^{(a)}$ is the number N of atoms in the state $|J_g, \mu_g = +1\rangle$; etc. The choice $F = \exp[-|z|^2/2 + z\hat{a}_{+1}^{\dagger}](\hat{a}_{-1}^{\dagger})^m/\sqrt{m!}$ leads to the m-fold excited states $|D, m\rangle$ of a dark polariton [11].

4. One can see from Eq. (5) that there is a certain symmetry between field and atoms. Indeed, two spinor Bose fields of ranks J_g and 1 are combined into a spinor Bose field of rank J_e. The physical nature of the combined fields is to some extent immaterial in our model. These considerations lead to the second class of dark solutions. The corresponding algebra is similar to the manipulations used above, but with interchanging ground-state atoms and photons. Let us introduce the photon creation operator in the dark state:

$$\hat{A}_{NC}^{\dagger} = \sum_s \hat{w}_s(\hat{b}_{J_g})\hat{a}_s^{\dagger}. \qquad (11)$$

Here, the operator coefficients $\hat{w}_s(\hat{b}_{j_g})$ (components of the vector $\hat{\mathbf{w}}$) satisfy the system of equations

$$\{\hat{\mathbf{w}}(\hat{b}_{j_g}) \otimes \hat{b}_{J_g}\}_{J_e\mu_e} = 0, \qquad (12)$$

which has nontrivial solutions if $J_e < 1$ and $J_g = J_e = 1$, i.e., only for four transitions. Below, we give the explicit form of these solutions. For the $1 \longrightarrow 0$ and $1 \longrightarrow 1$ transitions, the vector $\hat{\mathbf{w}}$ is linear with respect to the vector $\hat{\mathbf{b}} \equiv \hat{b}_{J_g=1}$:

$$\hat{\mathbf{w}} = \mathbf{c} \times \hat{\mathbf{b}} \ (J_e = 0); \quad \hat{\mathbf{w}} = \hat{\mathbf{b}} \ (J_e = 1), \qquad (13)$$

where $\mathbf{c}$ is an arbitrary *c*-number vector. For the $1/2 \longrightarrow 1/2$ and $3/2 \longrightarrow 1/2$ transitions, $\hat{\mathbf{w}}$ depends quadratically on $\hat{b}_{J_g}$:

$$\hat{\mathbf{w}} = \{\hat{b}_{J_g} \otimes \hat{b}_{J_g}\}_1. \qquad (14)$$

Further, by analogy with Eq. (10), the main representative of the second class of dark states is parameterized by arbitrary functions ϕ and Φ:

$$|NC(\phi,\Phi)\rangle = \phi(\hat{A}_{NC}^{\dagger})\Phi(\hat{b}_{J_g}^{\dagger})|\text{vac}\rangle. \qquad (15)$$

It should be pointed out that, for a certain choice of functions f and F in Eq. (10) and functions ϕ and Φ in Eq. (15), the dark states $|NC(f,F)\rangle$ and $|NC(\phi,\Phi)\rangle$ may coincide; i.e., the first and second classes intersect along a certain set of elements. However, the second class also contains elements that do not enter the first class. This becomes most evident for the $1/2 \longrightarrow 1/2$ transition, where there are no dark states of the first class. Consider this case in more detail. We take the function Φ in the form $\Phi = \exp[-|z_+|^2/2 + z_+\hat{b}_{+1/2}^{\dagger}](\hat{b}_{-1/2}^{\dagger})^2/\sqrt{2}$, which corresponds to the Bose condensate of atoms with spin projection (+1/2) (described by the complex order parameter z_+) and two atoms with opposite projections. For simplicity, we choose the function ϕ in the linear form $\phi = \hat{A}_{NC}^{\dagger} =$

[1] We do not rigorously associate the angular momentum with the atomic statistics, with an eye to various circumstances, in particular, to the aforementioned isomorphism of the considered spin models with the models for nondegenerate states.

$(\hat{b}_{+1/2})^2\hat{a}^\dagger_{+1} + \sqrt{2}\hat{b}_{+1/2}\hat{b}_{-1}\hat{a}^\dagger_0 + (\hat{b}_{-1/2})^2\hat{a}^\dagger_{-1}$. The resulting dark state is the superposition

$$|NC\rangle = (z_+)^2|\{2\}^{(a)}_{-1/2}, \{1\}^{(ph)}_{+1}\rangle + 2z_+|\{1\}^{(a)}_{-1/2}, \{1\}^{(ph)}_0\rangle + \sqrt{2}|\{0\}^{(a)}_{-1/2}, \{1\}^{(ph)}_{-1}\rangle,$$

whose coefficients are controlled by the parameter z_+. Such states describe the essentially quantum entanglement of two subsystems (atoms and field) [16]. In the case considered, quantum entanglement is an additional factor that gives rise to the nontrivial dark states.

Turning back to the initial formulation of the problem with a given spatial field distribution (1), one realizes that this photon superposition of all three polarization states, generally speaking, is contradictory to the condition that electromagnetic waves are transverse. However, this problem does not arise for a nondegenerate model of a four-level atom interacting with a three-frequency field. In this case, the operators $\hat{a}^\dagger_{0,\pm1}$ create photons with different frequencies (ω_0 and $\omega_0 \pm \Omega$).

5. It is not evident from general considerations that the first and second classes encompass all possible dark states of our system, thereby motivating a search for the dark states that are different from those considered above. We will seek these solutions in the form

$$|NC\rangle = X(\hat{b}^\dagger_{J_g}, \hat{\mathbf{a}}^\dagger)|\text{vac}\rangle. \quad (16)$$

It is also assumed that the number N of atoms and the number m of photons are specified; then,

$$X = \sum_{(\mu),(s)} \mathcal{X}_{\mu_1,\ldots,\mu_N;\, s_1,\ldots,s_m}\hat{b}^\dagger_{J_g\mu_1}\ldots\hat{b}^\dagger_{J_g\mu_N}\hat{a}^\dagger_{s_1}\ldots\hat{a}^\dagger_{s_m}, \quad (17)$$

where the coefficients $\mathcal{X}_{(\mu),(s)}$ are symmetric about the permutation of any pair of indices $\mu_i \longleftrightarrow \mu_j$ and $s_k \longleftrightarrow s_l$. In addition, due to Eq. (2), the coefficients $\mathcal{X}_{(\mu),(s)}$ must satisfy the system of equations

$$\sum_{(\mu),(s)} C^{J_e\mu_e}_{J_g\mu_1 1 s_1}\mathcal{X}_{\mu_1,\ldots,\mu_N;\, s_1,\ldots,s_m} \times \hat{b}^\dagger_{J_g\mu_2}\ldots\hat{b}^\dagger_{J_g\mu_N}\hat{a}^\dagger_{s_2}\ldots\hat{a}^\dagger_{s_m} = 0. \quad (18)$$

It should be emphasized that the c-number coefficients $\chi_{(\mu),(s)}$ must turn Eq. (18) to the operator identity.

Clearly, the representatives of the first and second classes of dark states can have the form (16), (17) if the functions (f, F) or (ϕ, Φ) are appropriately chosen. To make sure that the form (16), (17) can also describe the dark states that do not belong to the first and second classes, we consider the bright $J \longrightarrow J+1$ transitions, for which there are no dark states of the first two classes. The estimation of the number of unknown coefficients $\mathcal{X}_{(\mu),(s)}$ and the number of linear equations for these coefficients shows that the nontrivial solutions to this problem necessarily exist for $\{N = 1, J + 1 > m\}$ and $\{N = 2, m = 1, J > 0)\}$. Since the number of atoms and photons is quite limited in all the cases, we call the dark states of the third class the ultraquantum states.

Let us clarify the structure of these states. In the case of $N = 1$, $J + 1 > m$, the dark state of the third class can be written as

$$|NC\rangle = (Q_L\{\hat{b}^\dagger_{J_g} \otimes \{\hat{\mathbf{a}}^\dagger\}_m\}_L)|\text{vac}\rangle, \quad (19)$$

where Q_L is an arbitrary tensor of rank $L = J - m + 1$ or $L = J - m$, and the total number of components of these two tensors corresponds to $4(J + 1 - m)$ linearly independent solutions. Note that, by choosing the appropriate linear combination of states (19), one can satisfy (for $J \geq m$) the condition that the photon polarization is transverse. In this case, the number of linearly independent solutions is equal to $(2J + 1 - 2m)$. As an example, we consider the $1 \longrightarrow 2$ transition for $m = 1$, $L = 1$, and $Q_1 = \mathbf{e}_0$ (one of the cyclic unit vectors); then,

$$|NC\rangle = \frac{|\{1\}^{(a)}_{+1}, \{1\}^{(ph)}_{-1}\rangle - |\{1\}^{(a)}_{-1}, \{1\}^{(ph)}_{+1}\rangle}{\sqrt{2}}.$$

In the case of $N = 2$, $m = 1$, and $J > 0$, the number of linearly independent states of the third class equals $J(2J + 1)$. We present only one example of the $1/2 \longrightarrow 3/2$ transition, for which there is only a single solution

$$|NC\rangle = (\{\hat{b}^\dagger_{J_g} \otimes \hat{b}^\dagger_{J_g}\}_1 \cdot \hat{\mathbf{a}}^\dagger)|\text{vac}\rangle. \quad (20)$$

6. Thus, the results presented in this work appreciably extend the family of dark states accounting for the CPT effect in a quantum system of resonantly coupled atoms and field, which is of fundamental importance in quantum optics. In addition, these results can become useful in the statement of experiments with atomic Bose condensates interacting with external fields and also in quantum information science.

We have also found dark states of all three classes in an ensemble of distinguishable atoms and in a fermionic ensemble. The corresponding results will be published elsewhere.

This work was supported by INTAS (grant no. 01-0855) and the Russian Foundation for Basic Research (project nos. 04-02- 16428, 04-02-16488, and 04-02-16525).

REFERENCES

1. E. Arimondo, Prog. Opt. **35**, 257 (1996).
2. P. R. Hemmer, S. Ezekiel, and C. C. Leiby, Jr., Opt. Lett. **8**, 440 (1983); A. Akulshin, A. Celikov, and V. Velichansky, Opt. Commun. **84**, 139 (1991); M. O. Scully and M. Fleischhauer, Phys. Rev. Lett. **69**, 1360 (1992); J. Kitching, S. Knappe, N. Vukicevic, *et al.*, IEEE Trans. Instrum. Meas. **49**, 1313 (2000); M. Stahler, S. Knappe, C. Affolderbach, *et al.*, Europhys. Lett. **53**, 323 (2001).
3. S. E. Harris, Phys. Today **50** (7), 36 (1997).

4. O. Kocharovskaya, Phys. Rep. **129**, 175 (1992); M. O. Scully, Phys. Rep. **129**, 191 (1992).
5. A. Aspect, E. Arimondo, R. Kaiser, *et al.*, Phys. Rev. Lett. **61**, 826 (1988); A. Aspect, E. Arimondo, R. Kaiser, *et al.*, J. Opt. Soc. Am. B **6**, 2112 (1989).
6. P. Marte, P. Zoller, and J. L. Hall, Phys. Rev. A **44**, 4118 (1991); M. Weitz, B. C. Young, and S. Chu, Phys. Rev. Lett. **73**, 2563 (1994); P. D. Featonby, G. S. Summy, C. L. Webb, *et al.*, Phys. Rev. Lett. **81**, 495 (1998).
7. V. S. Smirnov, A. M. Tumaĭkin, and V. I. Yudin, Zh. Éksp. Teor. Fiz. **96**, 1613 (1989) [Sov. Phys. JETP **69**, 913 (1989)]; A. M. Tumaĭkin and V. I. Yudin, Zh. Éksp. Teor. Fiz. **98**, 81 (1990) [Sov. Phys. JETP **71**, 43 (1990)]; A. V. Taichenachev, A. M. Tumaikin, and V. I. Yudin, Europhys. Lett. **45**, 301 (1999); A. V. Taĭchenachev, A. M. Tumaĭkin, and V. I. Yudin, Zh. Éksp. Teor. Fiz. **118**, 77 (2000) [JETP **91**, 67 (2000)].
8. B. J. Dalton and P. L. Knight, J. Phys. B **15**, 3997 (1982).
9. A. V. Taichenachev, A. M. Tumaikin, and V. I. Yudin, Laser Phys. **4**, 124 (1994).
10. I. E. Mazets and B. G. Matisov, Pis'ma Zh. Éksp. Teor. Fiz. **64**, 483 (1996) [JETP Lett. **64**, 515 (1996)].
11. M. Fleschauer and M. D. Lukin, Phys. Rev. Lett. **84**, 5094 (2000); Phys. Rev. A **65**, 022314 (2002).
12. C. Liu, Z. Dutton, C. H. Behroozi, *et al.*, Nature **409**, 490 (2001); D. F. Phillips, A. Fleischhauer, A. Mair, *et al.*, Phys. Rev. Lett. **86**, 783 (2001); A. S. Zibrov, A. B. Matsko, O. Kocharovskaya, *et al.*, Phys. Rev. Lett. **88**, 103601 (2002).
13. E. Cornell, Nature **409**, 461 (2001).
14. G. Juzeliunas and H. J. Carmichael, Phys. Rev. A **65**, 021601(R) (2002).
15. D. A. Varshalovich, A. N. Moskalev, and V. K. Khersonskiĭ, *Quantum Theory of Angular Momentum* (Nauka, Leningrad, 1975; World Sci., Singapore, 1988).
16. I. V. Bagratin, B. A. Grishanin, and V. N. Zadkov, Usp. Fiz. Nauk **171**, 625 (2001) [Phys. Usp. **44**, 597 (2001)].

Translated by V. Sakun

JETP Letters, Vol. 79, No. 2, 2004, pp. 71–75. Translated from Pis'ma v Zhurnal Éksperimental'noĭ i Teoreticheskoĭ Fiziki, Vol. 79, No. 2, 2004, pp. 80–85.

Excitation of Low-Lying Nuclear States by the Ion Line Emission in Femtosecond Laser Plasma

V. V. Bol'shakov, V. M. Gordienko, A. B. Savel'ev*, and O. V. Chutko**

International Laser Center, Faculty of Physics, Moscow State University, Moscow, 119992 Russia

**e-mail: savelev@femto.phys.msu.su*

***e-mail: chutko@mail.ru*

Received November 20, 2003; in final form, December 18, 2003

A scheme of nuclear excitation by the ionic X-ray lines in laser plasma using two femtosecond laser pulses is proposed. The first pulse produces plasma with a given degree of ionization, allowing the X-ray line energies of the target ions to be tuned to resonance with the nuclear transition, while the second pulse generates hot electrons that are necessary for X-ray generation. © *2004 MAIK "Nauka/Interperiodica"*.

PACS numbers: 25.20.Dc; 52.25.Os; 52.38.Ph; 52.50.Jm; 52.59.Px

1. Photoexcitation by plasma intrinsic bremsstrahlung and recombination X-radiation is the main channel for exciting low-lying nuclear states with energies ~1–20 keV in a hot dense plasma produced by a femtosecond laser pulse (femtosecond laser plasma (FLP)) with an intensity of 10^{16}–10^{17} W/cm^2 [1]. In such plasma, the overwhelming contribution to the output of nuclei excited to energies of 1–20 keV is provided by the X-radiation of a hot electronic component [2] which is generated with an efficiency that reaches, for the aforementioned pulse intensities, a few percent [3]. Hot electrons in FLP also induce efficient X-ray fluorescence of the target neutral atoms and ions [4, 5]. The corresponding power spectral density of the characteristic lines can exceed the power density of plasma bremsstrahlung and recombination radiation by several orders of magnitude. In early works [6, 7], it was suggested that nuclei be excited by the X-ray lines of neutral atoms; however, analysis shows that, as a rule, no exact resonance can be obtained for the X-ray line and the nuclear transition in this case.

In this work, it is proposed that the X-ray emission line can be tuned to resonance with the nuclear transition by controlling the degree of laser plasma ionization and, hence, the X-ray line energy [4]. Based on the fact that the plasma ionization state is determined primarily by the thermal electronic component, while an ionic X-ray line emission with an energy higher than 1 keV is induced by the hot electronic component, we suggest the nuclear excitation scheme with two ultrashort laser pulses, taking $^{201}Hg_{80}$ nucleus and quasi-resonance $K\alpha$ radiation of aluminum ion Al^{+9} as an example. The first pulse produces laser plasma that contains the maximal, in time and space, number of ions with the desired degree of ionization, while the second pulse generates hot electrons that are necessary for generating X-ray lines at the instant the fraction of ions with a certain degree of ionization reaches its maximum value in plasma.

2. To compare the excitation efficiencies of low-lying nuclear states by bremsstrahlung and line emission of the hot electronic component, one should take into account the following. First, the nuclear transition radiative width Γ_{rad} equals ~10^{-13}–10^{-10} eV [8], which is much smaller than the typical X-ray line width ΔE_{line} ~ 1–10 eV [9]. In turn, the typical plasma bremsstrahlung width is on the order of the hot-electron temperature T_h ~ 1–10 keV [10]. Second, the cross section $\sigma_{\gamma 0} = \lambda_0^{*2}/2\pi$ for nuclear resonance photoexcitation ($\lambda_0^* = hc/E_0^*$ is the wavelength of X-ray quantum resonant with the nuclear transition to energy E_0^*) is much greater than the cross section σ_{x0} for the "proper" absorption of this quantum by atoms and ions in the medium. Analysis shows [8, 9] that, for the majority of

Quasi-resonant nuclear and atomic transitions (E_0^* is the nuclear transition energy, E_{line} is the X-ray line energy, ΔE_{line} is the X-ray linewidth, ΔE is the detuning between the atomic and nuclear transitions) [8, 9]

Nucleus	E_0^*, eV	Atom/ion, type of line	E_{line}, eV	ΔE_{line}, eV	ΔE, eV
$^{201}Hg_{80}$	1561	Al_{13} ($K\beta_{1,3}$)	1557.5	~1	~4
		Al_{13}^{+9} ($K\alpha_1$)	1561	~1	0
$^{205}Pb_{82}$	2329	S_{16}^{+8} ($K\alpha_1$)	2332	~1	~3
$^{181}Ta_{73}$	6238	Tb_{65} ($L\alpha_2$)	6238	~5	0
$^{57}Fe_{26}$	14412	Am_{95} ($L\alpha_2$)	14412	~15	0

0021-3640/04/7902-0071$26.00

nuclei possessing low-lying states (see table), the ratio $\sigma_{\gamma 0}/\sigma_{x0}$ is on the order of 10^3.

It follows from the above relations that the proper absorption of resonance plasma radiation can be ignored; i.e., all X-ray quanta falling within the nuclear line will be absorbed by the nuclei in the medium. Taking into account that the nuclear transition width is relatively small, the total number N^* of X-ray-excited plasma nuclei can be estimated as

$$N^* \sim P(E_0^*)\Gamma_{\text{rad}}, \tag{1}$$

where $P(E_0^*)$ is the spectral density of resonance photons in plasma. Therefore, the output of excited nuclei can be enhanced by increasing the photon density near the nuclear transition using resonance X-ray lines emitted in laser plasma [4, 5]. The excitation efficiency of nuclear states, compared to the excitation by hot-electron bremsstrahlung, can be increased by

$$\varepsilon^* = \frac{P_{\text{line}}^{\text{opt}}(E_0^*)}{P_{\text{brem}}^{\text{opt}}(E_0^*)} \approx \frac{\eta_{\text{line}}}{\Delta E_{\text{line}}} \Big/ \frac{\eta_{\text{brem}}}{T_h} \tag{2}$$

times, where the indices "line" and "brem" correspond to plasma line emission and bremsstrahlung, respectively, and the index "opt" signifies that the calculations are carried out for the case of maximal output of resonance photons. In Eq. (2), the quantity η_{brem} is the conversion ratio of laser energy into the hot-electron bremsstrahlung. According to the results of [10], η_{brem} equals $\sim 10^{-6}$–10^{-5} at $T_h \sim 5$ keV and is determined by the target material. In the case of nuclear excitation by plasma bremsstrahlung with the power spectral density $\sim\exp(-E/T_h)$, the maximal output of resonance photons corresponding to the nuclear transition with energy E_0^* occurs at $T_h \sim E_0^*$. The quantity η_{line} is the conversion ratio of laser energy into the X-ray line emission. According to the estimates carried out in [5], the maximal value of η_{line} for the $K\alpha$ radiation is $\sim 10^{-5}$–10^{-4}. Therefore, depending on the X-ray line characteristics and the target material, the use of resonance $K\alpha$ radiation ($\Delta E_{\text{line}} \sim 1$ eV) of laser plasma for the excitation of low-lying ($E_0^* \sim 1$–10 keV) nuclear states provides a gain of

$$\varepsilon^* = \frac{P_{\text{line}}^{\text{opt}}(E_0^*)}{P_{\text{brem}}^{\text{opt}}(E_0^*)} \approx \frac{\eta_{\text{line}}}{\eta_{\text{brem}}} \frac{E_0^*}{\Delta E_{\text{line}}} \approx 10^4\text{–}10^5 \tag{3}$$

in the number of excited nuclei, as compared to the bremsstrahlung excitation.

3. Analysis of the literature and the data bases [8, 9] shows that it is quite difficult to find a pair of elements of which one has atomic transition in exact resonance with the nuclear transition of the other element, because, in most cases, energy detuning exceeds the X-ray line width ΔE_{line}. Examples of such coincidences for the $^{57}Fe_{26}$ and $^{181}Ta_{73}$ isotopes are presented in the table. It was suggested in [11] that this detuning can be compensated using atomic transitions from highly excited states, because, among the multitude of these transitions, a resonance with the nuclear transition can always be found. In actuality, the transitions from highly excited states have low oscillator strengths and, as a result, low fluorescence yield. Thus, only the atomic (and ionic) transitions with relatively high oscillator strengths, namely, the $K\alpha_{1,2}$, $K\beta_{1,3}$, and $L\alpha_{1,2}$ lines, among which $K\alpha_{1,2}$ has the maximal (one to three orders of magnitude higher) fluorescence yield, can be of practical interest for enhancing photoexcitation efficiency of low-lying nuclear levels.

For the majority of nuclear transitions, neutral atoms have no X-ray lines that are in exact resonance with these transitions and belong to intense series. However, the X-ray quantum energy increases upon ionization [4]. In addition, the ionic lines in a hot dense laser plasma have a set of satellites [4, 12] that, in particular, are due to the transitions from the doubly excited states and are offset by ~1–10 eV from the main emission line. Consequently, by controlling the degree of ionization and the density of laser plasma, one can accomplish fine tuning of the X-ray line or satellite energy to the resonance with the nuclear transition. Thus, both atomic and ionic X-ray lines can serve as sources for pumping nuclear transition. This appreciably extends the capabilities of the nuclear excitation scheme proposed in this work.

It is worth noting that the maximal intensities of the ionic X-ray lines can be achieved using femtosecond laser pulses [4]. As was noted above, the presence of a large fraction of hot electrons in laser plasma produced by such pulses [5] induces efficient characteristic emission of ions whose degree of ionization is determined by the temperature of plasma thermal electrons.

Let us take, for example, a $^{201}Hg_{80}$ nucleus. The energy $E_0^* = 1561$ eV [8] of its first excited state is close to the energy of the aluminum K series X-ray quanta (table). In a neutral aluminum atom, the $K\beta_{1,3}$ line is detuned by 4 eV, which exceeds the X-ray line width. However, the aluminum $K\alpha$ energy, whose dependence on the degree of ionization is shown in Fig. 1, increases from 1487 eV in a neutral atom to ~1600 eV in a helium-like ion. We calculated this dependence by the Dirac–Fock method using the software package from [13]. As the aluminum ion charge Z increases by unity (starting with $Z = 5$), the $K\alpha$ quantum energy increases, on average, by 15 eV. The Al^{+9} $K\alpha$ quantum energy ~1561 eV is in exact resonance with the transition energy E_0^* of the mercury $^{201}Hg_{80}$ nucleus (within the error of calculations and measurements). Therefore, a $^{201}Hg_{80}$ nucleus can be excited most efficiently by the Al^{+9} $K\alpha$ resonance emission. An analogous situation takes place for the other nuclei. In

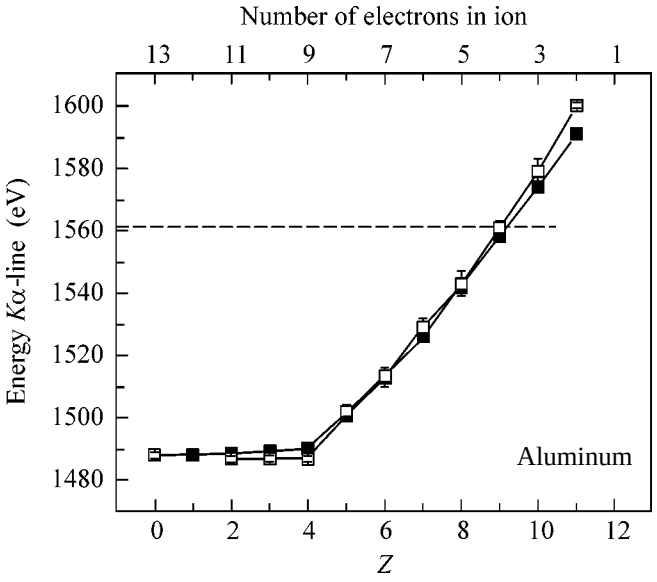

Fig. 1. Energies of the aluminum ion $K\alpha$ quanta. (■) Computational results using the Dirac–Fock software package [13] and (□) results from [4]. The dashed line indicates the $^{201}Hg_{80}$ transition energy (1561 eV).

particular, the $K\alpha$ emission of the sulfur ion S^{+8} at ~2332 eV is quasi-resonant with the $^{205}Pb_{82}$ nuclear transition at 2329 eV (table). In the scheme considered, the nucleus excitation yield is determined by the X-ray-emission intensity of ions with a vacancy in the inner shell, which, in turn, is determined by the fraction of such ions in plasma and by the probability of processes leading to the line emission at a given plasma density and temperature.

4. X-ray lines with a quantum energy above 1 keV are generated in plasma mainly by fast-electron impact ionization of inner ionic and atomic shells. Consequently, to optimize the line emission yield for an ion with charge Z, it is necessary that the maximal number of ions with charge $Z - 1$ and fast electrons for their inner-shell ionization simultaneously exist in plasma. It should be taken into account that the maximal content of ions with a given degree of ionization can be observed both at the plasma heating stage and in the course of plasma cooling.

Let us determine the parameters of a femtosecond laser pulse for which the Al^{+8} content in aluminum plasma is maximal. The ionization of the Al^{+8} K shell is followed by the Al^{+9} $K\alpha$ emission resonant with the nuclear transition in $^{201}Hg_{80}$. We will also calculate the instants of time at which the Al^{+8} content is maximal. In so doing, we do not consider the satellites caused by the transitions from the Al^{+9} excited states, because the maximal fraction of these ions in a solid laser plasma is achieved at electron temperatures on the order of 70 eV, for which the electronic excitation from the ground state with $n = 2$ to the state with $n \geq 3$ ($\Delta E > 250$ eV) is

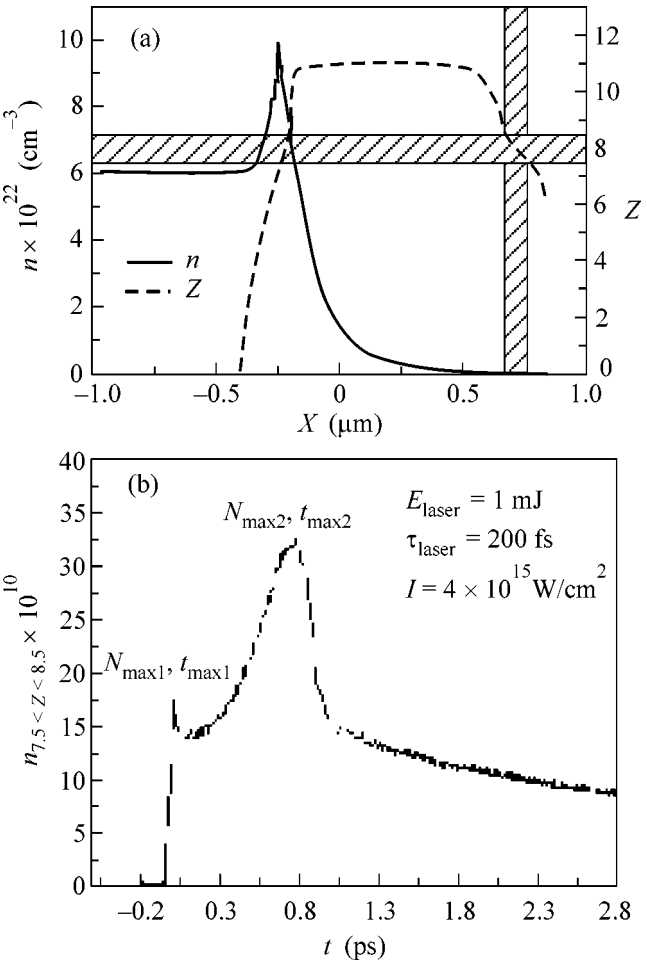

Fig. 2. (a) Spatial distributions of concentration n and degree of ionization Z of aluminum laser plasma at t = 1.34 ps after the laser shot ($I = 10^{16}$ W/cm^2, τ_{laser} = 200 fs). (b) Time dependence of the number N of aluminum ions with a charge of $7.5 < Z < 8.5$ in laser plasma (E_{laser} = 1 mJ, $I = 4 \times 10^{15}$ W/cm^2, τ_{laser} = 200 fs). The time $t = 0$ corresponds to the maximum of laser intensity.

inefficient. In particular, the satellite intensities in the $K\alpha$ spectra of the femtosecond aluminum plasma produced by pulses with $I \sim 3 \times 10^{16}$ W/cm^2 (100 fs, 1.5 mJ) [4] did not exceed the intensity of the main Al^{+9} $K\alpha$ line.

The laser plasma ionization state was analyzed using a one-dimensional code [14] that is designed to calculate the spatiotemporal plasma evolution with allowance for the ionization, heat conduction, and fluid dynamics of plasma produced at the solid target surface by a femtosecond laser pulse of moderate intensity. The typical spatial distributions calculated using the code [14] for the concentration and average charge in aluminum plasma at t = 1.34 ps after the pulse ($I = 10^{16}$ W/cm^2 and τ_{laser} = 200 fs; time is measured from the maximum of a Gaussian pulse envelope) are shown in Fig. 2a. The Al^{+8} ions of interest exist in two spatial

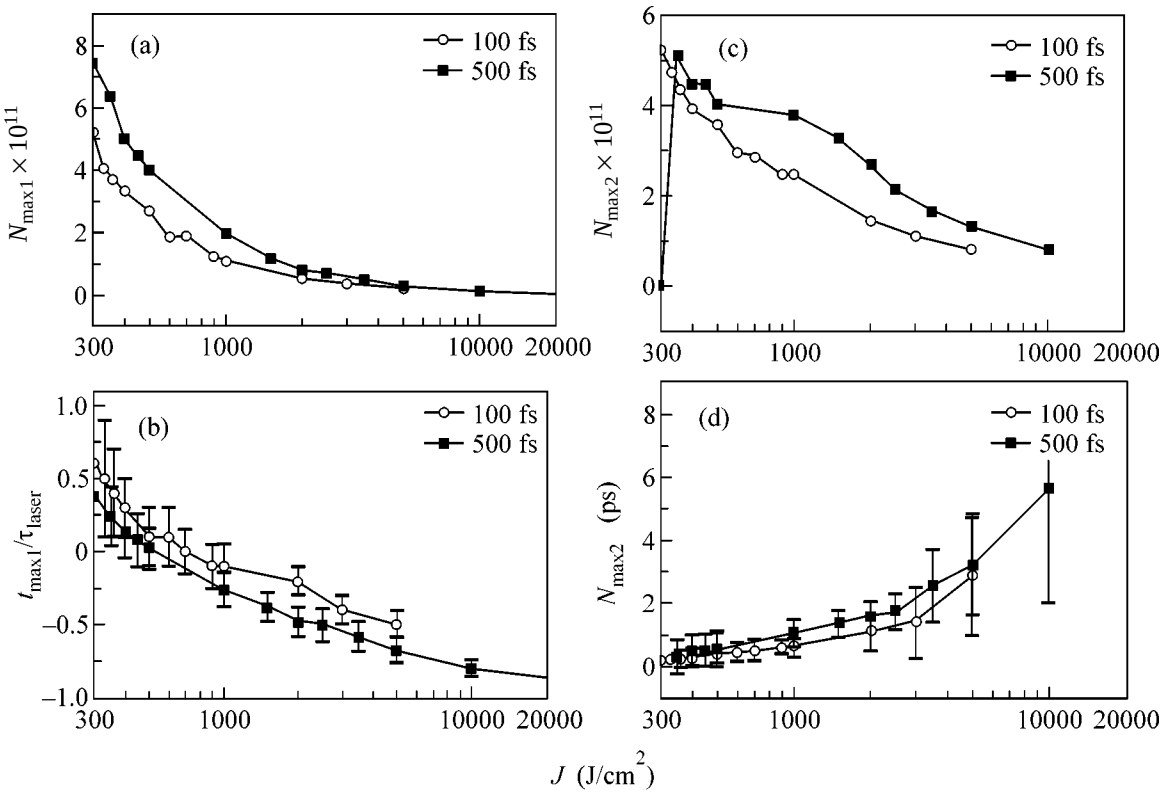

Fig. 3. The yields (N_{max1}, N_{max2}) and moments (t_{max1}, t_{max2}) of Al^{+8} ion formation as functions of laser fluence at the target surface. Calculations were carried out for a pulse energy of E_{laser} = 1 mJ.

regions: in the region of low plasma concentration at the leading front of expansion wave and deep within the target with a near-solid concentration. The time-dependent number of aluminum ions with charge $7.5 < Z < 8.5$ in plasma produced by a laser pulse with E_{laser} = 1 mJ, $I = 4 \times 10^{15}$ W/cm^2, and τ_{laser} = 200 fs is shown in Fig. 2b. One can see that the calculated curve has two maxima corresponding to the formation of ions of a given multiplicity at the instants of plasma heating N_{max1}, t_{max1} and cooling N_{max2}, t_{max2}. Due to the increase in the volume of the heated target region, the number of ions at the cooling stage may become greater than at the heating stage.

The dependences of yields N_{max1}, N_{max2} and instants t_{max1}, t_{max2} of Al^{+8} formation on the laser fluence J at the surface of the solid target were determined by varying the pulse parameters (Fig. 3). It was found that, for a laser pulse of duration τ_{laser} ~100–500 fs, the threshold of laser fluence J corresponding to the formation of aluminum ions Al^{+8} is 100–200 J/cm^2. The values of N_{max1} and N_{max2} reach their maxima of ~10^{11}–10^{12} ion/shot at fluences J ~ 300 J/cm^2 and decrease upon further increase in J. The value of t_{max1} and the lifetime (both normalized to the pulse duration τ_{laser}) of Al^{+8} ions formed at the plasma ionization stage decrease with increasing laser fluence J, because the plasma ionization rate increases. The plasma lifetime, the value of t_{max2}, and the total lifetime of Al^{+8} ions formed during the course of plasma cooling also increase with increasing fluence J.

It follows from these results that the maximum attainable amounts of Al^{+8} ions formed at the plasma ionization and cooling stages have the same order of magnitude. To generate the Al^{+9} $K\alpha$ line quasi-resonant with the nuclear transition in $^{201}Hg_{80}$, one must ionize the Al^{+8} K shell, which can be accomplished only by the hot electrons of laser plasma [4, 5]. It is known that the hot electronic component is formed mainly near the maximum of laser intensity [3, 10]. Therefore, one should provide conditions at which t_{max1} coincides with the instant t_{max1} = 0 of maximal pulse intensity; this is achieved for J ~ 500 J/cm^2 (Fig. 3). It follows from [4, 5] that the $K\alpha$ radiation is generated in laser plasma if the temperature of hot electrons reaches $T_h \sim 6E_{line}$, which corresponds to T_h ~ 9 keV for the aluminum $K\alpha$ line. To reach this temperature for hot electrons, it is necessary that the pulse intensity be ~10^{17} W/cm^2 [3], which corresponds to a pulse duration of ~5–10 fs for a fluence of J ~ 500 J/cm^2.

Although modern femtosecond laser technology can provide such radiation characteristics [15], the regime of plasma formation at the surface of a solid target by a

pulse as short as that is essentially different and nonadiabatic. In particular, the temperature of thermal electrons, the degree of ionization, etc., become appreciably lower. At the same time, the hot-electron generation by a pulse of a duration shorter than 10 fs may become as efficient as in the case of longer pulses. For this reason, it is necessary to use a two-pulse scheme with coinciding pulse-intensity maxima and appreciably different pulse durations; the "long" pulse (100–500 fs) produces plasma with a given degree of ionization, while the "short" pulse generates hot electrons at the instant of time $t_{\max 1}$.

A different situation occurs at the plasma cooling stage; the Al^{+8} lifetime is of the order of a few picoseconds. This also allows efficient Al^{+9} $K\alpha$ radiation in a two-pulse scheme, where the first pulse is used to form laser plasma, while the second serves for the efficient hot-electron generation at the instant the amount of Al^{+8} ions reaches its maximum at the plasma cooling stage. Note also that the optimal Al^{+9} $K\alpha$ radiation can be achieved by changing the energy and delay time of the second pulse, while the pulse duration is of little significance in this case.

5. Thus, high luminosity of the characteristic X-ray radiation allows the excitation efficiency of low-lying nuclear states to be increased by four to five orders of magnitude. High intensities of X-ray lines emitted by femtosecond laser plasma render it one of the most promising X-ray sources for nuclear excitation. The possibility of controlling the degree of laser-plasma ionization allows the use of X-ray lines from both neutral target atoms and various ions for these purposes. By controlling the degree of ionization, one can tune the ionic X-ray lines to the exact resonance with the nuclear transition energy and, thereby, greatly extend the potentialities of this method. In our opinion, the method with the use of two laser pulses is most promising—the heating pulse produces plasma with a given degree of ionization, while the ultrashort pulse generates hot electrons that create vacancies in the ion electronic shells; the latter are subsequently filled to emit X-ray quanta.

Note in conclusion that porous aluminum with mercury particles in its pores, a mercury–aluminum alloy in the form of amalgam, or the aluminum film applied to a substrate made of a material with a rather high mercury content can serve as targets in the experiments on the excitation of mercury nucleus $^{201}Hg_{80}$ by the $K\alpha$ radiation of aluminum laser plasma. Estimates show that, for an energy of ~20 mJ ($J \sim 500$ J/cm^2) of the heating pulse and an energy of ~1 J of the pulse generating hot electrons, the number of mercury $^{201}Hg_{80}$ nuclei excited by the Al^{+9} $K\alpha$ radiation is equal to ~10^2–10^3 nucleus/shot.

This work was supported by the ISTC–EOARD grant, no. 2651p.

REFERENCES

1. A. V. Andreev, V. M. Gordienko, and A. B. Savel'ev, Kvantovaya Élektron. (Moscow) **31**, 941 (2001).
2. A. V. Andreev, O. V. Chutko, A. M. Dykhne, *et al.*, Hyperfine Interact. **143**, 23 (2003).
3. A. Varanavichyus, T. V. Vlasov, R. V. Volkov, *et al.*, Kvantovaya Élektron. (Moscow) **30**, 523 (2000).
4. A. Rousse, P. Audebert, J. P. Geindre, *et al.*, Phys. Rev. E **50**, 2200 (1994).
5. D. Salzmann, Ch. Reish, I. Uschmann, *et al.*, Phys. Rev. E **65**, 036402 (2002).
6. V. S. Letokhov, Kvantovaya Élektron. (Moscow) **4**, 125 (1973).
7. V. S. Letokhov and E. A. Yukov, Laser Phys. **4**, 382 (1994).
8. Nucl. Data Sheets **85**, 415 (1998); Nucl. Data Sheets **62**, 101 (1991); Nucl. Data Sheets **71**, 421 (1994); Nucl. Data Sheets **69**, 679 (1993).
9. M. A. Blokhin and I. G. Shveĭtser, *X-ray Spectral Handbook* (Nauka, Moscow, 1982).
10. R. V. Volkov, V. M. Gordienko, P. M. Mikheev, and A. B. Savel'ev, Kvantovaya Élektron. (Moscow) **30**, 896 (2000).
11. A. A. Andreev, A. V. Charukchev, and V. E. Yashin, Proc. SPIE **4352**, 102 (2001).
12. G. C. Junkel-Vives, J. Abdallah, Jr., T. Auguste, *et al.*, Phys. Rev. E **65**, 036410 (2002).
13. I. M. Band and V. I. Fomichev, Preprint No. 498, LIYaF AN SSSR (Leningrad Inst. of Nuclear Physics, USSR Academy of Sciences, 1979).
14. V. M. Gordienko, M. A. Joukov, and A. B. Savel'ev, *Application of High Field and Short Wavelength Sources*, Ed. by L. DiMauro, M. Murnane, and A. H'Huiller (Plenum, New York, 1998), p. 155.
15. T. Brabec and F. Krausz, Rev. Mod. Phys. **72**, 545 (2000).

Translated by V. Sakun

JETP Letters, Vol. 79, No. 2, 2004, pp. 76–80. Translated from Pis'ma v Zhurnal Éksperimental'noĭ i Teoreticheskoĭ Fiziki, Vol. 79, No. 2, 2004, pp. 86–91.

BCS Instability of a Two-Layer System of Composite Fermions

Yu. E. Lozovik* and I. V. Ovchinnikov

Institute of Spectroscopy, Russian Academy of Sciences, Troitsk, Moscow region, 142190 Russia

**e-mail: lozovik@isan.troitsk.ru*

Received November 17, 2003

Pairing instability is considered for a two-layer electron system in a strong magnetic field with an even-fractional filling $\nu = 1/(2m)$ (m is an integer) of the lowest Landau level in each of the layers. The limit of large distance d between the layers is analyzed. Microscopic analysis is carried out in the eikonal approximation in the composite-fermion formalism. It is found that the condition for pairing instability in this model is independent of d. Due to the marginal character of the composite-fermion system, pairing instability in the particle–particle (BCS) channel arises only for $\eta < 2$ or $\eta = 2$, but $Mv_0 > 43$, where η and v_0 are the parameters of the assumed electron–electron interaction, $v \propto v_0/r^\eta$, and M is the band electron mass. In the particle–hole (isospin density wave) channel, instability is not observed. © *2004 MAIK "Nauka/Interperiodica".*

PACS numbers: 73.21.Ac; 73.43.-f

Two-layer systems under the conditions of fractional Hall effect have attracted considerable attention in the last decade [1, 2]. Such systems have much in common with a two-layer electron–hole system, in particular, in strong magnetic fields, for which superfluidity, the Josephson effect, and other phenomena were predicted (see [3] and the literature cited therein). The recent experimental observation of effects resembling the Josephson effect in a two-layer electron system [4] has additionally stimulated theoretical investigations in this field [5, 6].

The ground state of the system depends on the distance d between the layers and on tunneling between them, which can be characterized by the splitting Δ_{sas} of symmetric and antisymmetric one-particle states in the layers. The ground state of the system is clear in two limiting cases. For large values of Δ_{sas}, electrons occupy the lowest symmetric state, and the two layers behave as a single layer in the filling regime $\nu = m^{-1}$. In the absence of tunneling and for small values of d ($d \ll l_b$, where $l_b = \sqrt{\hbar c/eH}$ is the cyclotron radius), the Halperin state (m, m, m) plays the role of the ground state.

In actual situations, the value of Δ_{sas} decreases exponentially with increasing d. At present, the ground-state evolution with increasing d (without allowance for Δ_{sas}) is a matter of disagreement. Namely, it is not clear whether an increase in d causes a quantum transition from the Halperin (m, m, m) state to the Halperin ($2m$, $2m$, 0) state that is a state of uncorrelated layers each in the $\nu = 1/2m$ regime. In terms of composite fermions, such a transition would indicate the existence of a BCS instability at $d < d_c$, where d_c is a certain critical distance between the layers, and the absence of instability at $d > d_c$. To answer this question, we will study in this work the instability of the ($2m$, $2m$, 0) state to pairing of composite fermions from different layers with a large distance d between them. The main difficulty in the analysis of pairing of the two systems of composite fermions is that an individual layer of composite fermions is not *normal* but *marginal* Fermi liquid. This means that the decay of quasiparticles at the Fermi surface is on the same order of magnitude as the quasiparticle energy, which may prevent pairing. In the case of normal Fermi liquids, such a problem does not arise since a bound state always exists in the presence of an indefinitely weak attraction between two quasiparticles at the Fermi surface; at zero temperature, the system is always unstable to pairing.

It will be shown below that, in the long-wavelength limit, pairing and marginal corrections are determined by the same gauge-field propagator, which necessitates the inclusion of both of them in calculations. In addition, it is necessary to make allowance for the so-called "most intersecting" diagrams, which are most significant in this problem [7]. Both requirements can be taken into account by using the eikonal approximation [8] that was developed for 2D systems with a singular interaction of the current–current type [9].

Let us consider the ground state of a 2D electron system in a transverse magnetic field with filling $\nu = 1/2m$ in each layer. We disregard tunneling and assume that both layers have the same density ρ, electron mass M, and, hence, chemical potential μ. After the addition of $2m$ flux quanta to each electron, we arrive at the

Lagrangian density for composite fermions that are associated with the Chern–Simons gauge field [10]

$$\mathcal{L} = \psi^{(\alpha)\dagger}\left(i\mathcal{D}_0^{(\alpha)} - \frac{(-i\boldsymbol{\mathcal{D}}^{(\alpha)})^2}{2M}\right)\psi^{(\alpha)} + \zeta a_0^{(\alpha)}\boldsymbol{\partial}\times\mathbf{a}^{(\alpha)} - \frac{1}{2}\int d\mathbf{r}'|\psi^{(\alpha)}|^2(\mathbf{r})\,v^{(\alpha\beta)}(\mathbf{r}-\mathbf{r}')|\psi^{(\beta)}|^2(\mathbf{r}').$$

Here, the Greek indices, over which the summation is assumed, label the levels ($\alpha, \beta = 1, 2$); $\zeta = 1/4\pi m$; $(a_0^{(a)}, \mathbf{a}^{(\alpha)})$ are the gauge fields in the layers; $i\mathcal{D}_0^{(\alpha)} = i\partial_0 - a_0^{(\alpha)} + \mu$; $-i\boldsymbol{\mathcal{D}}^{(\alpha)} = -i\boldsymbol{\partial} - \mathbf{a}^{(\alpha)}$; and the second term on the right-hand side is the Chern–Simons term in the radiation gauge, $\boldsymbol{\partial}\mathbf{a}^{(\alpha} = 0$, which we use. The electron–electron interaction potential has the form $v^{(\alpha\beta)}(\mathbf{r}) \propto v_0/(r^2 + d^2(1-\delta_{\alpha,\beta}))^{\eta/2}$, where $\eta \geq 1$ (the cases $\eta = 1$ and $\eta \geq 2$ correspond to the Coulomb and short-range interaction, respectively). The Fourier components of the potentials have the form $v^{(\alpha\beta)} = v_0 e^{-qd(1-\delta_{\alpha,\beta})}/q^{2-\eta}$.

To find the gauge-field propagator, we will use the results obtained for a one-layer composite-fermion system[1] for $\nu = 1/(2m)$. In the low-frequency and long-wavelength limit, the time-like gauge-field component is screened and the behavior of the system is only determined by the transverse component, whose polarization operator is given by [12] $\Pi = -\gamma(i|q_0|/q) + \chi_0 q^2$, where $\gamma = 2\rho/k_F$; $k_F = \sqrt{4\pi\rho}$ and $v_F = k_F/M$ are the Fermi momentum and (nonrenormalized) velocity, respectively; and $\chi_0 = (24\pi M)^{-1}$ is the diamagnetic susceptibility of a 2D Fermi liquid. The propagator of the transverse part of gauge field has the following long-wavelength asymptotic form:

$$D = (D_0^{-1} - \Pi)^{-1} = \left(\gamma\frac{i|q_0|}{q} - \chi_0 q^2 - \chi q^\eta\right)^{-1}, \quad (1)$$

where D_0 is the "bare" field propagator: $D_0^{-1} = -\zeta^2 q^2 v(q) \equiv -\chi q^\eta$, $\chi = \zeta^2 v_0$. Hereinafter, when defining the transverse gauge-field propagators, we imply the presence of a factor $\Delta_{ij}(\mathbf{q}) = \delta_{ij} - q_i q_j/q^2$ reflecting the transverse nature of the gauge field, where indices i and j label the spatial coordinates $\{\hat{x}, \hat{y}\}$.

In a two-layer system, however, the transverse gauge-field propagator becomes a matrix relative to the layer indices (α, β), $D \longrightarrow \hat{D} \equiv D^{(\alpha\beta)}$. The bare propagator has the form $\hat{D}_0^{-1} = -\zeta^2 q^2 v^{(\alpha\beta)}(q)$. The polarization operator is diagonal relative to the layer indices, $\hat{\Pi} = \Pi\hat{E}$, where $\hat{E}$ is a unit 2×2 matrix. Thus, the transverse field propagator has the form

$$\hat{D} = [\hat{D}_0^{-1} - \hat{\Pi}]^{-1} = \frac{1}{2}\left(\frac{\hat{E}^+}{\gamma\frac{i|q_0|}{q} - \chi_0 q^2 - \chi q^\eta(1+e^{-dq})} + \frac{\hat{E}^-}{\gamma\frac{i|q_0|}{q} - \chi_0 q^2 - \chi q^\eta(1-e^{-dq})}\right),$$

$$\hat{E}^+ = \begin{bmatrix}1 & 1\\ 1 & 1\end{bmatrix}, \quad \hat{E}^- = \begin{bmatrix}1 & -1\\ -1 & 1\end{bmatrix}.$$

The diagonal elements in both terms are responsible for singular self-energy corrections, i.e., for the marginal character of Fermi liquid in both layers. The nondiagonal elements are responsible for the interlayer interactions between composite fermions. The nondiagonal elements of the first and second terms differ in sign and, accordingly, account for the repulsion and attraction between the composite fermions from different layers, which is associated with the in-phase and antiphase fluctuations of the fermion density.

The distance d between the layers is a natural scale of the system. In the limit $qd \gg 1$, the pattern of two noninteracting layers is restored, each layer being connected with its own gauge field,

$$\hat{D} = D\hat{E} + O(e^{-dq}) \quad (2)$$

with D from relation (1). These "fast" degrees of freedom ($q > d^{-1}$) in two "noninteracting" layers can be integrated; this preserves the layers as normal Fermi liquids but renormalizes the Fermi velocities and/or the coupling constant. It will be shown below that this short-wavelength renormalization does not affect our analysis; for this reason, we do not introduce additional notation for the renormalized Fermi velocity v_F.

It remains to make allowance for the gauge-field modes belonging to the opposite limit ($qd \ll 1$). In this case, the main singular part of the propagator depends on parameter η,

$$\hat{D} = \begin{cases}\dfrac{1}{2}\dfrac{\hat{E}^-}{\gamma\frac{i|q_0|}{q} - \chi' q^2}, & \eta < 2,\\ \dfrac{1}{2}\left(\dfrac{\hat{E}^+}{\gamma(i|q_0|/q) - (\chi_0 + 2\chi)q^2} + \dfrac{\hat{E}^-}{\gamma(i|q_0|/q) - \chi_0 q^2}\right), & \eta = 2,\\ \hat{E}D, & \eta > 2,\end{cases} \quad (3)$$

[1] A one-layer system of 2D composite fermions interacting with the gauge field belongs to the class of Fermi systems with a strong forward scattering (see, for example, the review [11]).

where $\chi' = \chi_0$ for $\eta > 1$ and $\chi' = \chi_0 + d\chi$ for $\eta = 1$, while the propagator D in the last line is defined by relation (1). It can be seen that, in contrast to the long-range interaction ($\eta < 2$), not only the term responsible for the interlayer attraction but also the term responsible for the interlayer repulsion is retained in the case of short-range interaction ($\eta = 2$). Consequently, the instability condition in this case may depend on the ratio of these terms, i.e., on the parameter $\chi/\chi_0 \propto Mv_0$ (see condition (8) below). In the case of $\eta > 2$, the pattern of noninteracting layers is restored. In the latter systems, the BCS instability cannot arise and we will no longer consider this case.

For a fermion existing near a certain point $k_F\mathbf{e}$ of the Fermi surface ($\mathbf{e}$ is a unit vector), we can linearize dispersion $\xi(\mathbf{p}) = p^2/2m - \mu \approx \mathbf{n}(\mathbf{p} - k_F\mathbf{e})$, where $\mathbf{n} \equiv v_F\mathbf{e}$. We also shift the origin of fermion momentum $\mathbf{p}$ to this point of the Fermi surface, so that $\xi(\mathbf{p}) = \mathbf{np}$ and $p/k_F \ll 1$. Henceforth, fermion momenta will be measured from the point of the Fermi surface near which a given fermion lives.

We are interested in the particle–particle and particle–hole channels. Instability (if it exists) must arise in one-time correlators with zero momentum transfer:

$$L^{\pm}_{\mathbf{p},\mathbf{p}'}(t) = \begin{cases} \langle \hat{\psi}_{1,\mathbf{p}}(t)\hat{\psi}_{2,\mathbf{p}'}(t)\hat{\psi}^{\dagger}_{1,\mathbf{p}}(0)\hat{\psi}^{\dagger}_{2,\mathbf{p}'}(0)\rangle, \\ \langle \hat{\psi}_{1,\mathbf{p}}(t)\hat{\psi}^{\dagger}_{2,\mathbf{p}'}(t)\hat{\psi}^{\dagger}_{1,\mathbf{p}}(0)\hat{\psi}_{2,\mathbf{p}'}(0)\rangle. \end{cases}$$

Here and below, the signs $\pm$ correspond to the particle–particle and particle–hole channels, while the primed and unprimed variables correspond to a particle in the first layer and a particle or a hole in the second layer, respectively.

It was mentioned above that we will use the eikonal approximation, which was developed in [8] for 2D fermion systems associated with the gauge field. This approach is similar to the one developed by Svidzinsky [13], who used the Fock method of intrinsic time to exactly solve the Bloch–Nordsieck model.

The expressions for the required correlators in the eikonal approximation with the notation introduced above have the form

$$L^{\pm}_{\mathbf{p},\mathbf{p}'}(t) = \pm\int_{\mathbf{r}} \exp\left\{-i(\mathbf{np} \pm \mathbf{n}'\mathbf{p}')t - i\iint_{\mathbf{q};\, t_1 t_1'} \mathrm{Tr}(\hat{D}(t_1' - t_1)\hat{S}\hat{\Theta})\right\}, \quad (4)$$

$$\hat{\Theta}^{\alpha\beta} = \mathrm{Diag}\{\theta(\mathbf{n}(\mathbf{p}-\mathbf{q})); \theta(\pm\mathbf{n}'(\mathbf{p}' \mp \mathbf{q}))\},$$

$$\hat{S}^{\alpha\beta} = \Delta_{ij}(\mathbf{q})a_i^{\alpha}(t_1')a_j^{\beta}(t_1)^*,$$

$$a_i^{\alpha}(t) = [\mathbf{n}_i e^{i\mathbf{nq}t}; \pm\mathbf{n}_i' e^{i\mathbf{n}'\mathbf{q}t}e^{i\mathbf{qr}}].$$

Here, the asterisk denotes complex conjugation, integration with respect to additional variable $\mathbf{r}$ ensured zero momentum transfer, the trace symbol refers to the layer indices, and $t > t_1 > t_1' > 0$.

Following [14], we note that the fermion propagator with a linearized fermion dispersion is independent of the momentum-transfer component $q_\perp$ perpendicular to $\mathbf{n}$. Thus, $q_\perp$ appears only via the propagator of virtual gauge-field quanta, and we can independently integrate all such propagators with respect to $q_\perp$. Introduce

$$\tilde{D}(q_0) = \frac{1}{2}\int_{q_\perp} \frac{(q_\perp/q)^2}{\gamma\frac{i|q_0|}{q} - \chi' q^{\tilde{\eta}}} \approx -C\left(\frac{i}{|q_0|}\right)^{\xi},$$

$$\tilde{D}(t) = \int_{q_0} e^{-iq_0 t}\tilde{D}(q_0) = -\tilde{C}i^{\xi}|t|^{\xi-1}, \quad (5)$$

where $C = \gamma^{\xi}\chi'^{-(1-\xi)}(1-\xi)/2\sin(\pi\xi)$, $\tilde{C} = C\sin\left(\frac{\pi}{2}\xi\right)\Gamma(1-\xi)/\pi$, and parameter $\xi = (\tilde{\eta}-1)/(\tilde{\eta}+1) = 1/3$ is introduced for convenience ($\tilde{\eta}$ is the power with which q appears in D definition (3); i.e., $\tilde{\eta} \equiv 2$ ($\tilde{\eta}$ differs from the parameter η of the initial interaction between electrons)).[2] The *averaged* propagator can be written in the form

$$\hat{\tilde{D}} = \tilde{D}(\hat{E}^{-} + \alpha\hat{E}^{+}). \quad (6)$$

Here, $\alpha = 0$ and $\alpha = (1 + 2\chi/\chi_0)^{-(1-\xi)}$ for the systems with long-range and short-range interactions, respectively. The use of the averaged propagator effectively reduces the problem to the 1D case; henceforth, we assume that all fermion momenta are one-dimensional ($p \equiv p_\parallel$).

In the particle–particle (+) and particle–hole (–) channels, we must set $\mathbf{n} = \mp\mathbf{n}'$, respectively. Using relations (4) and (6), we obtain the following expression for correlators:

$$L^{\pm}_{p,p'}(t) = \pm v_F e^{-i(p-p')t}\int_r e^{\phi^{\pm}_{p,p'}(t,r)}, \quad (7)$$

where function ϕ is defined by the expression

$$\phi^{\pm}_{p,p'}(t,r) = \frac{-v_F}{2\pi}\int_{t_1,t_1'}\int \tilde{D}(t_1' - t_1) \times \left\{(1+\alpha)\frac{e^{i\mathbf{np}(t_1'-t_1)} + e^{\pm i\mathbf{n}'\mathbf{p}'(t_1'-t_1)}}{(t_1'-t_1) - i\delta} + (1-\alpha)\left(\frac{e^{i\mathbf{np}(r\mp(t_1'\pm t_1))}}{r\mp(t_1'\pm t_1) - i\delta} \pm \frac{e^{i\mathbf{n}'\mathbf{p}'(r-(t_1'\pm t_1))}}{r-(t_1'\pm t_1)\pm i\delta}\right)\right\}$$

[2] The case of $\tilde{\eta} \neq 2$ does not correspond to any physical system; however, for generality, we retain parameters $\tilde{\eta}$ and/or ξ instead of their numerical values.

with $\tilde{D}$ from (5) (we also substituted $r/v_F \longrightarrow r$). This relation consists of two terms. The term independent of r corresponds to the diagonal elements of propagator; i.e., this term takes into account the marginal corrections caused by the virtual gauge-field quanta that begin and end at the same fermion line. The second term corresponds to the nondiagonal elements of gauge-field propagator; i.e., this term takes into account the exchange of quanta between fermion lines.

In order to reveal instability, it is sufficient to consider particles located directly at the Fermi surfaces, i.e., the case $p, p' \longrightarrow 0$ ($\phi^{\pm}(t, r) \equiv \phi^{\pm}_{0,0}(t, r)$):

$$\phi^{\pm}(t, r) = \tilde{g} t^{\xi} F^{\pm}(r/t - 1/2(1 \pm 1)),$$

$$F^{\pm}(x) = i^{\xi}\left[\frac{2(1+\alpha)}{\xi(\xi-1)} + (1-\alpha) f^{\pm}(x)\right],$$

$$f^{+}(x) = \frac{{}_2F_1(1, 1; 2+\xi|1/x) - (x \longrightarrow -x)}{\xi(\xi+1)x},$$

$$f^{-}(x) = \left(\frac{{}_2F_1(1, 1-\xi; 2-\xi|x)}{1-\xi}\right.$$

$$\left. - \frac{{}_2F_1(1, 1+\xi; 2+\xi|1/x)}{(\xi+1)x}\right) - (x \longrightarrow -x).$$

Here, $\tilde{g} = v_F \tilde{G}/2\pi$ and ${}_2F_1(x)$ is a hypergeometric function.

Instability arises if the real part of function ϕ tends to $+\infty$ at $t \longrightarrow +\infty$ for at least one value of ratio r/t. In this case, expression (7) exponentially diverges as $t \longrightarrow +\infty$. This criterion can be written in the form

$$\max_{x \in (-\infty, \infty)} \mathrm{Re}F^{\pm}(x) = \mathrm{Re}F^{\pm}(1) > 0.$$

The correctness of the equality sign in this expression (i.e., the fact that function $\mathrm{Re}F^{\pm}(x)$ assumes its maximal value at $x = 1$) can be directly seen from Fig. 1. One can see from the figure that the results of this work can be formulated as follows:

(i) a particle–particle (BCS) channel contains instability in the case of long-range interaction ($\tilde{\eta} = 2 < \tilde{\eta}_0 \approx 2.1988$, $\alpha = 0$), as well as in the case of short-range interaction ($\tilde{\eta} = 2 < \tilde{\eta}_0 \approx 2.1988$, $\alpha > 0$) but at $\alpha > \alpha_0 \approx 0.083$ or, which is the same, at

$$Mv_0 > \frac{\pi}{3}(\alpha_0^{-1/(1-\xi)} - 1) \approx 43; \quad (8)$$

(ii) a particle–hole channel (spin-density wave) does not contain instability.

The fact that the instability condition is independent of distance d between the layers is quite natural. The attraction between composite fermions from different layers is determined by the asymmetric density fluctuations and appears only at lateral distances considerably exceeding d. At such distances, the electron–electron interaction "does not distinguish" between the layers; consequently, the instability condition should be independent of d.

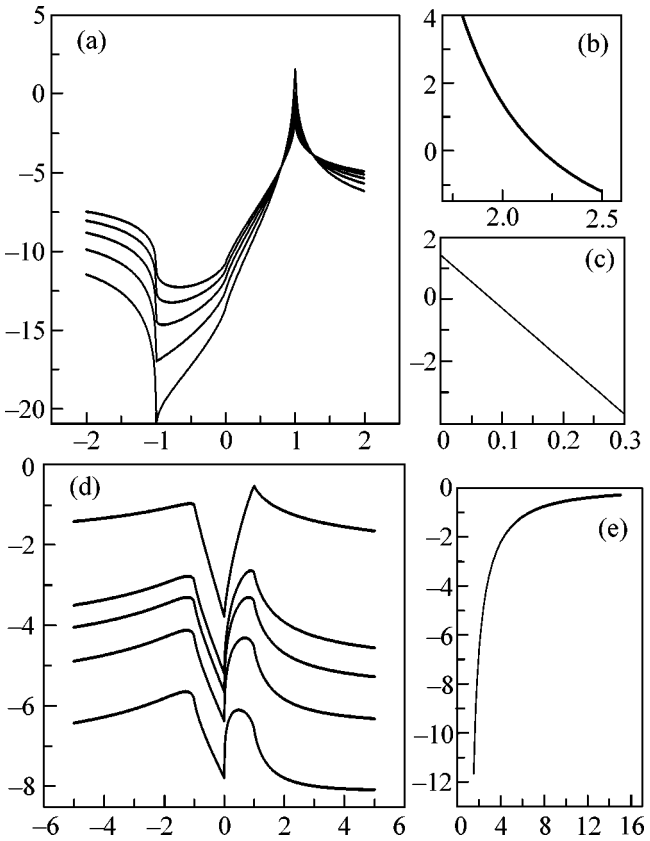

Fig. 1. (a) Long-range interaction ($\alpha = 0$). Function $\mathrm{Re}F^{+}(x)$ for $\tilde{\eta} = 1.8$, 2, 2.2, 2.4, and 2.6. (b) $\mathrm{Re}F^{+}(1)$ as a function of $\tilde{\eta}$; $\mathrm{Re}F^{+}(1) > 0$ for $\tilde{\eta} < \tilde{\eta}_0 \approx 2.1988$. (c) Short-range interaction ($\tilde{\eta} = 2$, $\alpha > 0$); $\mathrm{Re}F^{+}(1)$ as a function of $\alpha > 0$; $\mathrm{Re}F^{+}(1) > 0$ for $\alpha < \alpha_0 \approx 0.083$. (d) Function $\mathrm{Re}F^{-}(x)$ for $\tilde{\eta} = 2$, 2.5, 3, 3.5, and 10. (e) $\mathrm{Re}F^{-}(1)$ as a function of $\tilde{\eta}$.

The gap appearing due to pairing must decrease with increasing d [5]. In *normal* Fermi liquid, the gap can collapse (analogously to other two-layer Fermi systems; see, for example, [3] and the literature cited therein) in the presence of a disorder asymmetric relative to the layers. The gap can also collapse [15] due to the difference in the shapes of Fermi surfaces in the layers (e.g., due to anisotropy of the mass tensor [16]). Clearly, the pairing between two *marginal* Fermi liquids is even more fragile. Thus, in actual systems, the instability should disappear when d reaches a certain critical value d_c.

For $\eta = 2$, $Mv_0 < 43$, or at $\eta > 2$, a marginal liquid of composite fermions removes pairing instability of a two-layer system at large values of d. In particular,

instability must be absent in systems located close to metal surfaces, where, due to image forces, the effective electron–electron interaction becomes dipole–dipole interaction ($\eta = 3$). In such systems, at large interlayer distances, the ($2m$, $2m$, 0) state is stable (for this reason, the quantum transition ($2m$, $2m$, 0) $\leftrightarrow$ (m, m, m) must occur at intermediate distances).

This study was supported by the Russian Foundation for Basic Research and INTAS.

REFERENCES

1. J. P. Eisenstein, S. M. Girvin, and A. H. MacDonald, in *Perspectives in Quantum Hall Effects*, Ed. by S. Das Sarma and A. Pinczuk (Wiley, New York, 1997) and reference therein.
2. T. Chakraborty and P. Pietilainen, Phys. Rev. Lett. **59**, 2784 (1987); Y. W. Suen, L. W. Engel, M. B. Santos, *et al.*, Phys. Rev. Lett. **68**, 1379 (1992); J. P. Eisenstein, G. S. Boebinger, L. N. Pfeiffer, *et al.*, Phys. Rev. Lett. **68**, 1383 (1992); H. A. Fertig, Phys. Rev. B **40**, 1087 (1989); A. H. MacDonald, P. M. Platzman, and G. S. Boebinger, Phys. Rev. Lett. **65**, 775 (1990); R. Cote, L. Brey, and A. H. MacDonald, Phys. Rev. B **46**, 10239 (1992); X. G. Wen and A. Zee, Phys. Rev. Lett. **69**, 1811 (1992); Phys. Rev. B **47**, 2265 (1993); Z. Ezawa and A. Iwazaki, Phys. Rev. B **48**, 15189 (1993); S. He, S. Das Sarma, and X. C. Xie, Phys. Rev. B **47**, 4394 (1993); K. Moon, H. Mori, K. Yang, *et al.*, Phys. Rev. B **51**, 5138 (1995); A. Stern, S. Das Sarma, M. P. A. Fisher, and S. M. Girvin, Phys. Rev. Lett. **84**, 139 (2000).
3. Yu. E. Lozovik, O. L. Berman, and V. G. Tsvetus, Phys. Rev. B **59**, 5627 (1999); Yu. E. Lozovik and O. L. Berman, JETP Lett. **64**, 573 (1996); Yu. E. Lozovik and V. I. Yudson, JETP Lett. **22**, 274 (1975).
4. I. B. Spielman, J. P. Eisenstein, L. N. Pfeiffer, and K. W. West, Phys. Rev. Lett. **84**, 5808 (2000).
5. N. E. Bonesteel, Phys. Rev. B **48**, 11484 (1993); N. E. Bonesteel, I. A. MacDonald, and C. Nayak, Phys. Rev. Lett. **77**, 3009 (1996); T. Morinari, Phys. Rev. Lett. **81**, 3741 (1998).
6. L. Balents and L. Radzihovsky, Phys. Rev. Lett. **86**, 1825 (2001); A. Stern, S. M. Girvin, A. H. MacDonald, and N. Ma, Phys. Rev. Lett. **86**, 1829 (2001); M. M. Fogler and F. Wilczek, Phys. Rev. Lett. **86**, 1833 (2001); J. Schliemann, S. M. Girvin, and A. H. MacDonald, Phys. Rev. Lett. **86**, 1849 (2001); C. B. Hanna, Phys. Rev. B **66**, 165325 (2002); A. A. Burkov and A. H. MacDonald, Phys. Rev. B **66**, 115320 (2002); E. Demler, C. Nayak, H.-Y. Kee, *et al.*, Phys. Rev. B **65**, 155103 (2002); Y. B. Kim, C. Nayak, E. Demler, *et al.*, Phys. Rev. B **63**, 205315 (2001).
7. P. W. Anderson, Phys. Rev. Lett. **65**, 2306 (1990); Phys. Rev. Lett. **66**, 3226 (1991); Phys. Rev. Lett. **67**, 2092 (1991); P. C. E. Stamp, Phys. Rev. Lett. **68**, 2180 (1992).
8. D. V. Khveshchenko and P. C. E. Stamp, Phys. Rev. Lett. **71**, 2118 (1993); Phys. Rev. B **49**, 5227 (1994).
9. J. Gan and E. Wong, Phys. Rev. Lett. **71**, 4226 (1993); B. Blok and H. Monien, Phys. Rev. B **47**, 3454 (1993); C. Nayak and F. Wilczek, Nucl. Phys. B **417**, 359 (1994).
10. J. K. Jain, Phys. Rev. Lett. **63**, 199 (1989); Phys. Rev. B **40**, 8079 (1989); B. I. Halperin, P. A. Lee, and N. Read, Phys. Rev. B **47**, 7312 (1993).
11. W. Metzner, C. Castellani, and C. Di Castro, Adv. Phys. **47**, 317 (1998); cond-mat/9701012.
12. Y. B. Kim, A. Fukusaki, X.-G. Wen, and P. A. Lee, Phys. Rev. B **50**, 17917 (1994).
13. A. V. Svidzinsky, Zh. Éksp. Teor. Fiz. **31**, 324 (1957) [Sov. Phys. JETP **4**, 179 (1957)]; V. A. Fock, Phys. Z. Sowjetunion **12**, 404 (1937); F. Bloch and A. Nordsieck, Phys. Rev. **52**, 54 (1937).
14. C. Castellani, C. Di Castro, and W. Metzner, Phys. Rev. Lett. **72**, 316 (1994); B. L. Altshuler, L. B. Ioffe, and A. J. Millis, Phys. Rev. B **50**, 14048 (1994).
15. Yu. E. Lozovik and V. I. Yudson, Solid State Phys. **17**, 1613 (1975).
16. D. B. Balagurov and Yu. E. Lozovik, Phys. Rev. B **62**, 1481 (2000).

Translated by N. Wadhwa

JETP Letters, Vol. 79, No. 2, 2004, pp. 81–84. Translated from Pis'ma v Zhurnal Éksperimental'noĭ i Teoreticheskoĭ Fiziki, Vol. 79, No. 2, 2004, pp. 92–96.

Nature of the Magnetic Excitation Spectrum in (Sm,Y)S: CEF Effects or an Exciton?

P. A. Alekseev[1], J.-M. Mignot[2], E. V. Nefedova[1,*], K. S. Nemkovskiĭ[1], V. N. Lazukov[1], I. P. Sadikov[1], and A. Ochiai[3]

[1] *Russian Research Centre Kurchatov Institute, pl. Kurchatova 1, Moscow, 123182 Russia*
**e-mail: elene@isssph.kiae.ru*
[2] *Laboratoire Leon Brillouin, CEA/Saclay, 91191 Gif sur Yvette, France*
[3] *Tohoku University, Sendai 980, Japan*
Received November 26, 2003

The dynamic magnetic susceptibility spectrum in a single-crystal sample of the intermediate-valence compound $Sm_{0.67}Y_{0.33}S$ is studied by inelastic neutron scattering with neutron momentum transfer and sample temperatures varying over wide ranges. Two coupled collective modes have been found in the spectrum. Unlike the higher energy mode, whose intensity approximately follows the form factor of Sm^{2+}, the lower energy mode exhibits a stronger angular dependence than could be expected from the form factor for the localized *f* electrons. The total intensity of the inelastic component of the magnetic response decreases with increasing temperature; this is accompanied by the appearance of a broad quasi-elastic signal of a magnetic nature at significantly lower temperatures than follows from the calculated intensities of the transitions within the excited multiplet of the Sm^{2+} ion. An analysis of the observed features allows the suggestion to be made that the fine structure of the magnetic excitation spectrum in (Sm,Y)S is associated with the formation of an exciton-like intermediate-valence state on Sm ions rather than with the crystal-electric-field effects. © *2004 MAIK "Nauka/Interperiodica".*

PACS numbers: 75.30.Cr; 75.40.Gb; 61.12.Ex

Samarium sulfide SmS is a semiconductor-type compound that undergoes an isomorphic electronic phase transition either upon applying an external pressure (≥0.6 GPa) or due to the substitution of Y for Sm (so-called chemical pressure). In this case, a Sm *f* electron becomes partially delocalized; that is, the system passes from an integral valence state to an intermediate-valence (IV) state. One of the dispersion magnetic modes associated with the intermultiplet spin–orbit (SO) $J = 0 \longrightarrow J = 1$ transition of Sm^{2+} was detected in the energy range $E = 10$–45 meV in the magnetic excitation spectrum of a single-crystal SmS compound at normal pressure and low temperature by inelastic neutron scattering [1]. The presence of the dispersion is explained by the fact that the magnetic excitation spectrum is formed under the conditions of indirect exchange interaction between the magnetic moments of rare-earth ions through the *d* band.

Until recent work [2], detailed studies of the magnetic excitation spectrum in the IV phase of single-crystal (Sm,Y)S samples had not been carried out. The first results have shown that even a small chemical pressure leads to a qualitative rearrangement of the magnetic excitation spectrum of SmS. Thus, along with the excitation close to the intermultiplet SO transition (observed in stoichiometric SmS), a second magnetic mode is observed in the spectrum of a $Sm_{0.83}Y_{0.17}S$ single crystal [2]. This mode is also of the dispersion type but with a lower energy. The intensities of both magnetic modes depend strongly and in the opposite way on the wave vector. As the wave vector increases within the Brillouin zone, the modes exchange their intensities, evidencing their interaction.

At present, there exist two approaches to the explanation of the nature of the additional mode in an Y-diluted compound. The authors of [3] consider the occurrence of two peaks in the spectrum as the appearance of fine structure as a result of a change in the initial potential of the crystal electric field (CEF). In this work, it is suggested that the partial substitution of Y^{3+} for Sm^{2+} in the rare-earth sublattice leads to a change (reduction) in the local symmetry of the nearest environment of the Sm ion. As a result, a tetragonal component arises in the potential of the initially cubic CEF, leading to a noticeable splitting of the first excited state of the Sm^{2+} ion ($J = 1$) into a singlet and a doublet and, correspondingly, to the appearance of two peaks in the spectrum of intermultiplet magnetic transitions. Hence, both peaks detected in $Sm_{0.83}Y_{0.17}S$ are of the same nature and result from the CEF effects.

However, at the same time, it is known that even a small substitution of yttrium ions for Sm in SmS leads to a change of the valence state of Sm ions, and the valence in the $Sm_{0.83}Y_{0.17}S$ compound deviates from the

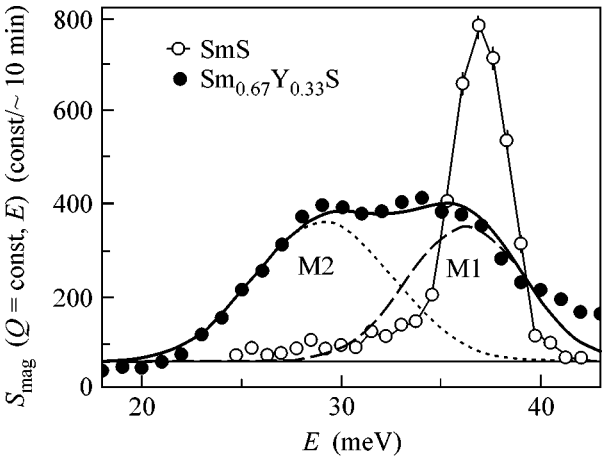

Fig. 1. Magnetic components in the spectra of $Sm_{0.67}Y_{0.33}S$ for Q = (1.35, 1.35, 1.35) (●) and SmS [7] for Q = (1.4, 1.4, 1.4) (○) obtained at T = 15 K. Lines correspond to fitting the $Sm_{0.67}Y_{0.33}S$ spectrum by two peaks.

integral value (~2.2 at T = 10–300 K [4]). The fact that Sm in $Sm_{0.83}Y_{0.17}S$ is in the IV state can affect the magnetic excitation spectrum of f electrons. Actually, the double-peak structure of the spectrum was described in [2] on the basis of an exciton model that implies the occurrence of a quantum-mechanically mixed electronic configuration (f^6 + a weakly bound state of a hole with the f^5 configuration and an f electron in the conduction band) in each ion. This approach was developed in [5] for the description of a homogeneous IV state of Sm in the SmB_6 compound. The main features of its magnetic and lattice excitation spectra, as well as the known phonon anomalies in (Sm,Y)S and SmS under pressure, were explained within this approach [6]. In [2], it was suggested that the mode with the higher energy was associated with an SO transition for the initial electronic configuration of the Sm^{2+} state in $Sm_{0.83}Y_{0.17}S$, and the mode with the lower energy was due to excitation from the new, exciton-like intermediate-valence ground state. Thus, this representation treats the experimental data as a result of the appearance of a qualitatively new mode differing from the single-ion SO excitation.

In order to answer the principal question as to whether the double-peak structure of the magnetic excitation spectrum in (Sm,Y)S is a result of the splitting of the state with J = 1 upon the reduction of the local symmetry of the nearest environment of Sm ions or a result of the formation of a new ground state of samarium with its specific excitation spectrum, new experimental facts are necessary.

In order to answer this question, one may try to increase the valence of the Sm ions by changing the concentration of Y in the $Sm_{1-x}Y_xS$ compound and, thus, enhance both the structural disorder and the valence instability effects. In particular, at low temperature, the valence of the Sm ions in $Sm_{0.67}Y_{0.33}S$ considerably differs from an integral value (~2.34), and an additional increase in the valence up to a value of ~2.4 is observed with increasing temperature (T > 200 K). On the one hand, the enhancement of valence instability can change the magnetic excitation spectrum. On the other hand, if the excitation spectrum is determined by the CEF effects, one should evidently expect the total suppression of any pronounced structure (or the appearance of a multiple-peak structure) in the spectrum because of an increase in the number of variants of various charge configurations in the environment of Sm ions.

In this work, the magnetic excitation spectrum of a $Sm_{0.67}Y_{0.33}S$ single crystal was studied in detail over a wide range of momentum transfer Q and temperatures.

A $Sm_{0.67}Y_{0.33}S$ single-crystal sample (NaCl-type structure) with a volume of ~0.17 cm^3 was grown by the Bridgeman method using isotopically enriched ^{154}Sm (98.6%). The single-crystal mosaic structure was no worse than 1°. The inelastic neutron scattering measurements were carried out in the Laboratoire Leon Brillouin on a 2T1 triple-axis spectrometer using a Cu(111) monochromator (a (002) pyrographite monochromator was used in measurements of a quasi-elastic signal), a (002) pyrographite analyzer, and a graphite filter for the suppression of higher order reflections. The inelastic neutron scattering spectra were obtained in the temperature range T = 12–200 K at a fixed energy of scattered neutrons E_f = 30.5 meV (in the case of the pyrographite monochromator, E_f = 14.7 meV) with a resolution of ~2 meV for the elastic line.

The magnetic excitation spectrum of $Sm_{0.67}Y_{0.33}S$ measured for the [111] direction is presented in Fig. 1. As in $Sm_{0.83}Y_{0.17}S$, the spectrum of $Sm_{0.67}Y_{0.33}S$ exhibits two peaks of magnetic nature (M1 and M2). These magnetic excitations demonstrate the presence of dispersion of the energies of peak maxima (Figs. 2a, 2b). Moreover, the intensities of these peaks depend substantially on the reduced wave vector. The peaks exchange their intensities as the wave vector advances from the center to the boundary of the Brillouin zone (Figs. 2c, 2d). However, two distinctive features of the $Sm_{0.67}Y_{0.33}S$ spectrum can be noted in comparison with $Sm_{0.83}Y_{0.17}S$ (the valences are ≈2.34 and 2.2, respectively). The energy dispersion of both magnetic excitations noticeably decreases, and its character changes. The dispersion minimum shifts from the center of Brillouin zone, which is possibly due to the enhancement of the antiferromagnetic component in the exchange coupling parameters. On the average, the difference in energy between the peaks increases with respect to the analogous data for $Sm_{0.83}Y_{0.17}S$ (≈2.5 meV) and equals ≈5 meV. Moreover, low-energy magnetic peak M2 becomes more pronounced and dominates almost in the entire Brillouin zone (Figs. 2c, 2d). At the same time, the peak widths in $Sm_{0.67}Y_{0.33}S$ increased only slightly.

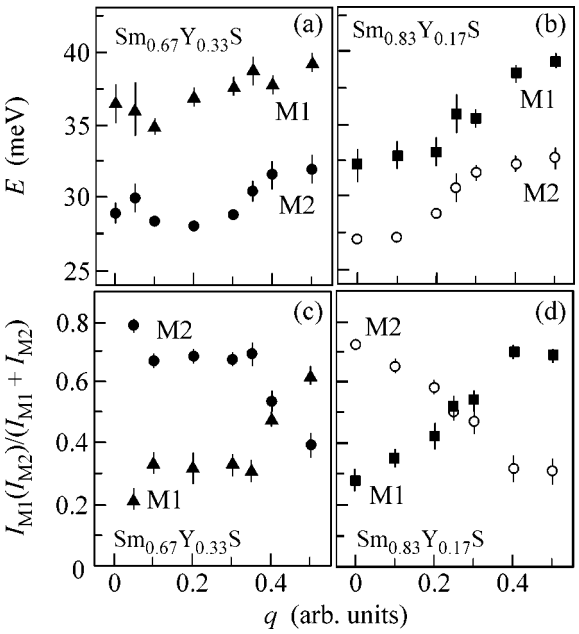

Fig. 2. Dispersion curves for the energies of the magnetic peak maxima for (a) $Sm_{0.67}Y_{0.33}S$ and (b) $Sm_{0.83}Y_{0.17}S$ [2] and the relative intensities of these peaks for (c) $Sm_{0.67}Y_{0.33}S$ and (d) $Sm_{0.83}Y_{0.17}S$ [2] in the [111] direction at $T = 15$ K.

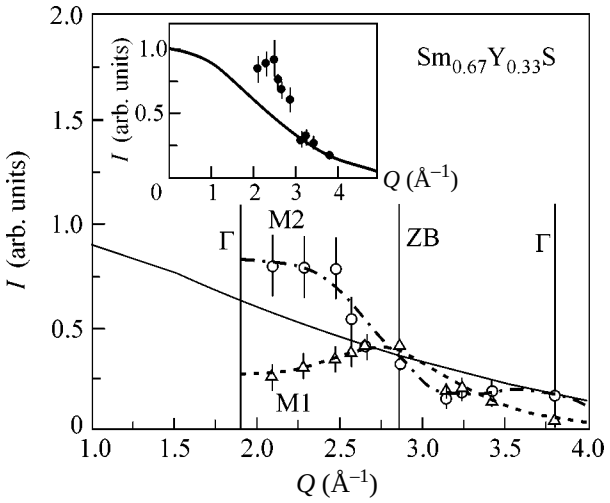

Fig. 3. Q dependence of the intensities of magnetic peaks for $Sm_{0.67}Y_{0.33}S$ (△ is M1, and ○ is M2) in the [111] direction at $T = 15$ K. The solid line corresponds to the form factor calculated for the $J = 0 \longrightarrow J = 1$ transition of the Sm^{2+} ion. The experimental intensities are reduced to the calculated form factor at $Q = 2.66$ Å^{-1}. The dashed lines are guides to the eye. Γ and BZ designate the center and boundaries of the Brillouin zone, respectively. The inset demonstrates the Q dependence of the total intensity of two magnetic peaks reduced to the Q dependence of the form factor for the maximum measured value of Q.

Figure 3 shows the Q dependences of the intensities of each magnetic excitation and the total intensity of the two peaks reduced to the Q dependence of the form factor for the $J = 0 \longrightarrow J = 1$ transition of the Sm^{2+} ion at the maximum measured value of Q (inset in Fig. 3). The partial intensities exhibit oscillatory behavior with a period equal to the size of the Brillouin zone. Unlike the intensity of high-energy excitation M1, the intensity of low-energy magnetic peak M2 exhibits, on the average, a sharper Q dependence compared to the normal form factor for the $J = 0 \longrightarrow J = 1$ transition of the Sm^{2+} ion. This leads to a situation where the total intensity also decreases with increasing Q more sharply than the normal form factor (inset in Fig. 3).

The temperature dependence of the total intensity of magnetic peaks for $Sm_{0.67}Y_{0.33}S$ also proved to be nontrivial. First, the intensity of the inelastic (M1 + M2) component of the $Sm_{0.67}Y_{0.33}S$ spectrum does not follow the temperature population factor in the energy level diagram for Sm^{2+} (the populations of the J_0, J_1, and J_2 multiplets are taken into account for the Sm^{2+} ion) but decreases much more rapidly with decreasing temperature (Fig. 4a). This cannot be explained on the basis of the formation of the excitation spectrum with regard to only the interaction with the CEF. Second, as the temperature increases, rather broad quasi-elastic scattering of the magnetic nature appears in the spectrum at a significantly lower temperature than might be expected from the calculation of the temperature population of multiplet levels for Sm^{2+} (Fig. 4b). It should be noted that an increase in temperature to 100 K still does not lead to the appearance of a quasi-elastic signal in divalent SmS. The halfwidth of the quasi-elastic peak in $Sm_{0.67}Y_{0.33}S$ is $\Gamma/2 \sim 6$ meV at $T = 70$ K. On the order of magnitude, this corresponds to the characteristic temperature T_0 of valence-unstable systems [8]. The appearance of the quasi-elastic component at a sufficiently low temperature can be explained by spin fluctuations that are characteristic for the new IV state of Sm.

The obtained experimental results indicate that the Sm transition to the IV state as a result of chemical pressure changes the magnetic excitation spectrum qualitatively; an additional collective low-energy magnetic mode appears in the spectrum. The properties of this mode (stronger temperature dependence of the intensity and the momentum transfer) and the appearance of the quasi-elastic component at temperatures considerably lower than might be expected from the calculation of the temperature population factor of single-ion states suggest that this additional low-energy mode in the excitation spectrum of (Sm,Y)S is associated with the excitation of electronic states that are delocalized more strongly than is typical of f electrons. Moreover, as the yttrium concentration increases ($Sm_{0.83}Y_{0.17}S \longrightarrow Sm_{0.67}Y_{0.33}S$), the intensity of high-energy excitation associated with an intermultiplet transition for the initial (partial) f^6 state of Sm^{2+}

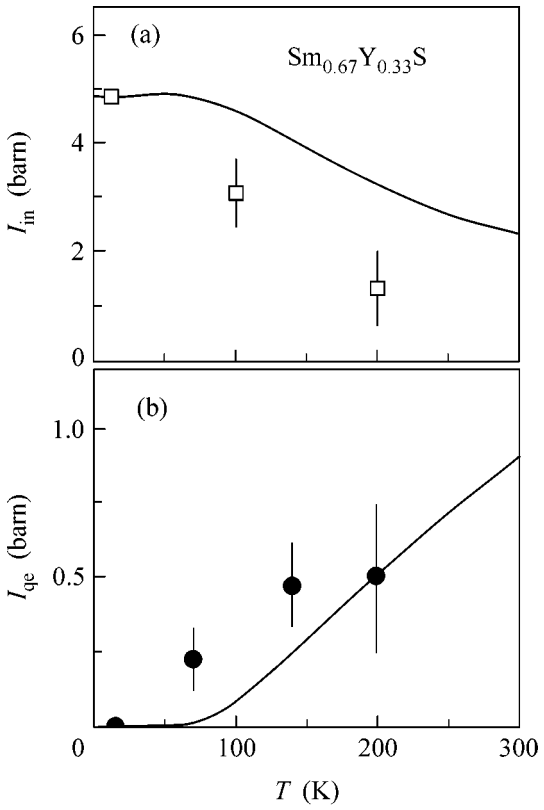

Fig. 4. Temperature dependence of the intensity of (a) integrated inelastic component of the magnetic excitation spectrum (□) and (b) quasi-elastic signal (●) for $Sm_{0.67}Y_{0.33}S$. Lines correspond to the calculated temperature dependence of the intensity for the multiplet energy levels of Sm^{2+} with regard to the change in valence. The experimental data are reduced to those calculated at T = 12 K in (a) and at T = 200 K in (b).

decreases and, simultaneously, the intensity of the low-energy excitation increases. This fact implies that the role of the exciton-like state in the formation of ground-state properties becomes more important as the valence increases. An increase in the Y concentration also enhances the disturbance of the regularity in the arrangement of rare-earth ions; however, this circumstance led only to a certain broadening of the peaks. The double-peak shape of the spectrum was retained, which is difficult to reconcile with the description of the excitation spectrum on the basis of the CEF effects. It should also be noted that the CEF effects are, as a rule, not observed at all in the systems in which the rare-earth ion is in an intermediate-valence state [8].

Thus, the intermediate-valence state of Sm ions in (Sm,Y)S can be presented as an exciton-like state similar to the state detected previously in intermediate-valence SmB_6. However, contrary to SmB_6, in which a local (on each Sm ion) IV state is formed through the hybridization of the *f* states of Sm ions with the *p* orbitals of the nearest boron atoms [5], a basically (qualitatively) new IV state has been detected in (Sm,Y)S. The IV state in (Sm,Y)S is formed under conditions of a rather strong interaction between Sm ions. Contrary to SmB_6, the Sm *f* electrons in (Sm,Y)S are hybridized with the *d* orbitals of the nearest Sm atoms; that is, a collective exciton mode is observed in (Sm,Y)S.

We are grateful to K.A. Kikoin for useful discussions and to M. Braden for assistance in performing experiments. P.A.A. and K.S.N. are grateful to L.L.B. for hospitality and support in the course of performing the experiments.

This work was supported by the Russian Foundation for Basic Research (project no. 02-02-16521), State Scientific and Technical Program "Topical Trends in the Physics of Condensed Matter," Federal Target Program "Integration," and SSh-2037.2003.2.

REFERENCES

1. S. M. Shapiro, R. J. Birgeneau, and E. Bucher, Phys. Rev. Lett. **34**, 470 (1975).
2. P. A. Alekseev, J.-M. Mignot, A. Ochiai, *et al.*, Phys. Rev. B **65**, 153201 (2002).
3. R. S. Fishman and S. H. Liu, Phys. Rev. Lett. **89**, 247203 (2002).
4. P. A. Alekseev, J.-M. Mignot, U. Staub, *et al.*, Physica B (Amsterdam) **312–313**, 333 (2002).
5. K. A. Kikoin and A. S. Mishenko, J. Phys.: Condens. Matter **7**, 307 (1995).
6. K. A. Kikoin and A. S. Mishchenko, Zh. Éksp. Teor. Fiz. **94** (11), 237 (1988) [Sov. Phys. JETP **67**, 2309 (1988)].
7. P. A. Alekseev, J.-M. Mignot, E. V. Nefeodova, *et al.*, in *Abstracts of International Conference on Magnetism* (Rome, 2003), p. 264.
8. E. Holland-Moritz, D. Wohlleben, and M. Loewenhaupt, Phys. Rev. B **25**, 7482 (1982).

Translated by A. Bagatur'yants

JETP Letters, Vol. 79, No. 2, 2004, pp. 85–87. Translated from Pis'ma v Zhurnal Éksperimental'noĭ i Teoreticheskoĭ Fiziki, Vol. 79, No. 2, 2004, pp. 97–99.

Viscosity of Oxide Melts in the Doremus Model

M. I. Ojovan

Sir Robert Hadfield Building, Sheffield, S1 3JD, United Kingdom

e-mail: M.Ojovan@sheffield.ac.uk

Received November 18, 2003; in final form, December 4, 2003

It is shown that a model recently proposed by R.H. Doremus for the viscosity of oxide melts correctly reproduces a two-exponential expression for viscosity, which is observed experimentally. For both low and high temperatures, the temperature dependence of viscosity is of the Arrhenius type. The viscosity activation energy at low temperatures is high and equal to the sum of enthalpies of defect formation and their motion. The temperature of transition from high to low viscosity-activation energies is determined by the enthalpy and entropy of defect formation and is not associated with configurational changes. © *2004 MAIK "Nauka/Interperiodica".*

PACS numbers: 66.20.+d; 66.30.Lw

A mechanism of a viscous flow in oxide melts concerns not only industrial processes such as glass production but also changes in the Earth's depths such as magma flow and movements of continents, as well as the safety of the disposal of radioactive waste and the structure of emulsions [1–6]. At the same time, the temperature dependence of the viscosity of oxide melts is not completely clear. The viscosity of oxide melts is of the activation or Arrhenius type. However, the activation energy is constant only at low and high temperatures. With an increase in temperature, the viscosity activation energy decreases in the technologically most interesting temperature range. The formula most extensively used to describe the viscosity of oxide melts in this range is the Vogel–Tammann–Fulcher empirical formula that describes the temperature dependence of the activation energy and involves three parameters determined by fitting to the experimental data [1, 2]. However, although this formula is meant for the description of experimental data, it, first, does not provide the correct asymptotic behavior of viscosity and, second, involves nonphysical parameters varying unpredictably and inexplicably from one melt to another.

Recently, Doremus [7] critically analyzed the available models of oxide viscosity and showed that none of the available theoretical approaches satisfactorily explains the temperature dependence of viscosity. Numerous works in this field have not provided considerable advance. The most popular current approaches use the temperature dependence of the entropy of melts. However, these models do not provide correct asymptotic values for viscosity. Moreover, in contrast to entropy, viscosity shows no discontinuities near the transition temperature to the glassy state [7].

It is known that the viscosity of oxide melts is most exactly described by the two-exponential expression [7, 8]

$$\eta(T) = A\exp\left(\frac{B}{RT}\right)\left[1 + C\exp\left(\frac{D}{RT}\right)\right], \qquad (1)$$

where T is temperature; R is the molar gas constant; and A, B, C, and D are the empirical fitting parameters. The constant B and the sum $B + D$ are the viscosity activation energies at high and low temperatures, respectively. For oxide melts, B = 80–300 kJ/mol for $\log\eta < 3$ and $B + D$ = 400–800 kJ/mol for $\log\eta > 10$ [8].

Doremus [7] attempted to explain observed empirical dependence (1) on the basis of the Mott hypothesis about the forming role of defects in the melt structures. However, he obtained the temperature dependence of viscosity with only one exponential term. To explain observed dependence (1), Doremus assumed the possible defect condensation at high temperatures with the formation of more complicated structures similar to dislocations in crystals, which facilitate the viscous flow. This work aims to show that the Doremus model does provide the experimentally observed two-exponential temperature dependence of viscosity given by Eq. (1).

The viscosity of melts is related to the diffusion coefficient by the Stokes–Einstein relation $\eta(T) = kT/6\pi rD$. For this reason, following Doremus, we analyze the temperature dependence of the diffusion coefficient. The diffusion coefficient of defects with concentration C_d in a lattice with concentration C_0 is equal to [9–11]

$$D(T) = f\alpha\lambda^2\nu\left(\frac{C_d}{C_0}\right)\exp\left(\frac{S_m}{R}\right)\exp\left(-\frac{H_m}{RT}\right), \qquad (2)$$

0021-3640/04/7902-0085$26.00 © 2004 MAIK "Nauka/Interperiodica"

where f is the correlation factor ($f = 1$ for uncorrelated hopping); α is the lattice parameter ($\alpha = 1/6$ for the fcc lattice); λ is the hopping distance ($\lambda = a\sqrt{3/4}$ in the fcc lattice with edge a); ν is the vibration frequency; and S_m and H_m are the entropy and enthalpy of defect motion.

According to the Gibbs distribution, the concentration of defects involved in the diffusion is equal to

$$C_d = C_0 \frac{\exp(S_d/R)\exp(-H_d/RT)}{1 + \exp(S_d/R)\exp(-H_d/RT)}, \quad (3)$$

where H_d and S_d are the enthalpy and entropy of defect formation. The entropy of defect formation is not associated with the configuration, but it is a disorder entropy and is associated with lattice vibrations [9].

Let us define Doremus' temperature T_D as

$$T_D = H_d/(R + S_d). \quad (4)$$

If $T \ll T_D$, formula (3) is simplified to the expression that was used by Doremus in [7] and provided the one-exponential formula for viscosity. Thus, Doremus [7] obtained the asymptotic formula for viscosity at low temperatures, where it has high activation energy. The formula for viscosity in this limit corresponds to low defect concentrations.

Substituting Eq. (3) into Eq. (2) and using the Stokes–Einstein relation, we arrive at the following formula for viscosity in the Doremus model for any temperatures:

$$\eta(T) = \frac{kT}{6\pi r D_0}\exp\left(-\frac{S_m}{R}\right) \times \exp\left(\frac{H_m}{RT}\right)\left[1 + \exp\left(-\frac{S_d}{R}\right)\exp\left(\frac{H_d}{RT}\right)\right], \quad (5)$$

where $D_0 = f\alpha\lambda^2\nu$. Comparison of Eq. (5) with Eq. (1) gives the following expressions for coefficients A, B, C, and D in empirical formula (1):

$$A = \frac{kT}{6\pi r D_0}\exp\left(-\frac{S_m}{R}\right), \quad B = H_m,$$

$$C = \exp\left(-\frac{S_d}{R}\right), \quad D = H_d. \quad (6)$$

Formula (5) can be simplified at low and high temperatures. For $T \ll T_D$, Eq. (5) gives the one-exponential formula derived for viscosity by Doremus. In this limit, the viscosity activation energy is high and equal to $H_m + H_d$. For $T \gg T_D$, Eq. (5) also gives a one-exponential formula for viscosity but with low viscosity activation energy H_m. The viscosity of oxide melts can be calculated by Eq. (5) over the entire temperature range. The temperature T_D determines the region of transition from one activation energy to another. Thus, the Doremus model of viscosity exactly leads to the empirical expression for the temperature dependence (1) of viscosity, which properly describes the experimental data.

As is seen, the two-exponential formula for viscosity follows from the Doremus model without allowance for the defect aggregation into linear structures. Nevertheless, the assumption about the defect condensation in a melt cannot be completely excluded. Moreover, the condensation of excitations with the formation of condensed excited states has long been known and has been intensely studied recently in [12–15]. Linear structures formed by defects can promote a viscous melt flow, as occurs in crystalline substances upon the formation of dislocations. Indeed, the defect concentration in the melt increases at high temperatures. Therefore, the probability of forming cluster structures consisting of several elementary defects also increases. However, the stability of such structures cannot increase with temperature, and the concentration of linear structures cannot, thereby, increase monotonically with the melt temperature. In view of this circumstance, the defect condensation must be analyzed in more detail.

According to Eqs. (5) and (6), the temperature dependence of the melt viscosity is determined by the enthalpy and entropy of formation and motion of the defects promoting viscous flow. Depending on the nature of the melt, various structures can play the role of defects; e.g., these are nonbridged oxygen atoms or SiO molecules in silicate melts [7]. The main thermodynamic parameters of defects—H_d, S_d, H_m, and S_m—can be determined from the experimental data on the temperature dependence of viscosity by using Eqs. (5) and (6). Note also that the Doremus model describes the continuity of glass viscosity near the melting temperature, in contrast to the viscosity of crystals. In crystal melting, the Gibbs free energy $G_m = H_m - TS_m$ of defect motion decreases stepwise, which is manifested by the stepwise decrease in viscosity. In contrast, melting of glasses is not accompanied by stepwise changes in G_m, which explains the continuity of viscosity according to Eq. (5).

I am grateful to R.H. Doremus and W.E. Lee for valuable remarks and support of this work.

REFERENCES

1. Ya. I. Frenkel', *Kinetic Theory of Liquids* (Nauka, Leningrad, 1975; Clarendon Press, Oxford, 1946).
2. A. A. Appen, *Chemistry of the Glass* (Khimiya, Leningrad, 1974).
3. A. V. Byalko, *Nuclear Waste Disposal: Geophysical Safety* (CRC Press, London, 1994).
4. L. Vocaldo and D. Dobson, Philos. Trans. R. Soc. London, Ser. A **357**, 3335 (1999).
5. A. Sipp, Y. Bottinga, and P. Richet, J. Non-Cryst. Solids **288**, 166 (2001).

6. M. I. Ojovan, Zh. Éksp. Teor. Fiz. **104**, 4021 (1993) [JETP **77**, 939 (1993)].
7. R. H. Doremus, J. Appl. Phys. **92**, 7619 (2002).
8. M. B. Volf, *Mathematical Approach to Glass* (Elsevier, Amsterdam, 1988).
9. S. Mrowec, *Defects and Diffusion in Solids* (Elsevier, Amsterdam, 1980).
10. P. M. Fahey, P. B. Griffin, and J. D. Plummer, Rev. Mod. Phys. **61**, 289 (1989).
11. F. Faupel, W. Frank, M.-P. Macht, *et al.*, Rev. Mod. Phys. **75**, 237 (2003).
12. É. A. Manykin, M. I. Ojovan, and P. P. Poluéktov, Zh. Éksp. Teor. Fiz. **102**, 804 (1992) [Sov. Phys. JETP **75**, 440 (1992)].
13. G. É. Norman, Pis'ma Zh. Éksp. Teor. Fiz. **73**, 13 (2001) [JETP Lett. **73**, 10 (2001)].
14. L. Holmlid, J. Phys.: Condens. Matter **14**, 13 469 (2002).
15. E. A. Manykin, Laser Phys. **12**, 435 (2002).

Translated by R. Tyapaev

JETP Letters, Vol. 79, No. 2, 2004, pp. 88–90. Translated from Pis'ma v Zhurnal Éksperimental'noĭ i Teoreticheskoĭ Fiziki, Vol. 79, No. 2, 2004, pp. 100–103.

Electron Pairs for HTSC

A. F. Andreev

Kapitza Institute for Physical Problems, Russian Academy of Sciences, ul. Kosygina 2, Moscow, 119334 Russia
e-mail: andreev@kapitza.ras.ru

Received December 5, 2003

A simple physical picture of superconductivity is proposed for extremely doped CuO_2 planes. It possesses features that are observed for HTSC, such as a high superconducting transition temperature, the $d_{x^2-y^2}$ symmetry of order parameter, and the coexistence of a one-electron Fermi surface and the Bose–Einstein condensate of preformed electron pairs. © *2004 MAIK "Nauka/Interperiodica".*

PACS numbers: 74.20.-z; 74.78.-w

In addition to high superconducting transition temperatures, high-T_c superconductors are distinguished by the unusual *d* symmetry of order parameter (see [1]) and the coexistence of a well-defined one-electron Fermi surface and a pseudogap [2]. The latter phenomenon is usually attributed to the presence of preformed (i.e., in the normal state) electron pairs (in particular, bipolarons [3–7]).

In this work, we demonstrate the existence of a simple physical picture of superconductivity for the extremely doped CuO_2 planes (in the vicinity of the maximum hole-doping level compatible with superconductivity), which possesses the aforementioned characteristic features of HTSC.

Paired quasiparticles. The key point is the existence of peculiar "paired" quasiparticles in crystals in conditions where the tight-binding approximation applies, i.e., if the energy of electron–electron interaction at a distance on the order of atomic spacing considerably exceeds the electron-tunneling amplitude to neighboring lattice cites. Quasiparticles of this type were studied earlier [8] in helium quantum crystals and recently by Alexandrov and Kornilovitch [6] as a model of bipolarons in HTSC (see also [9]).

Let us consider two electrons localized at neighboring (1 and 2 in the figure) copper atoms (to be more precise, in unit cells containing these atoms) forming a square lattice in the CuO_2 plane. The electron tunneling from 2 to 4 or 6 does not change the energy of the system in view of the crystal lattice symmetry. The same is true for the electron tunneling from 1 to 3 or 5. Owing to this type of transitions, an electron pair can move as a whole over the entire plane, since the $2 \longrightarrow 4$ transition can be followed by the transition $1 \longrightarrow 7$ or $1 \longrightarrow 3$, and so on. Since the transitions do not change the energy of the system, the motion is fully coherent. An electron pair behaves as a delocalized Bose quasiparticle.

To calculate the quasiparticle spectrum, we consider the localized states of a pair,

$$|\mathbf{r}, \mathbf{r}', \alpha\beta\rangle = c^+_{\mathbf{r}\alpha} c^+_{\mathbf{r}'\beta}|0\rangle, \quad (1)$$

where $c^+_{\mathbf{r}\alpha}$ are the electron creation operators at point $\mathbf{r}$ with spin projection $\alpha = \uparrow, \downarrow$ and $|0\rangle$ is the electron vacuum.

The effective tunneling Hamiltonian H_{eff} is defined by the matrix elements of the operator

$$H = t\sum_{\mathbf{r}\mathbf{r}'\alpha} c^+_{\mathbf{r}'\alpha} c_{\mathbf{r}\alpha}, \quad (2)$$

which correspond to the transitions of one of the electrons to copper atoms that are next-to-nearest neighbors of the initial atom, in such a way that the energy of the system of two electrons remains unchanged. Here, *t* is

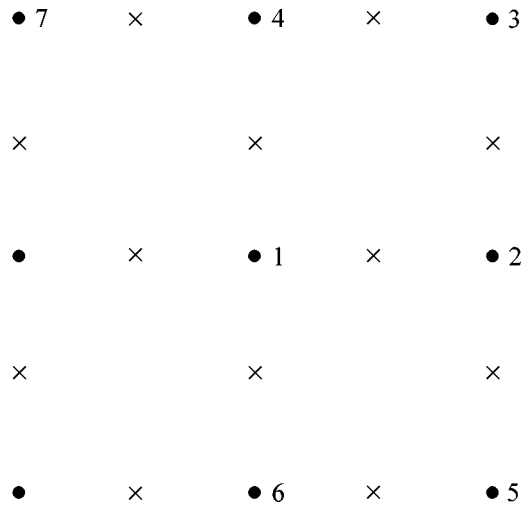

CuO_2 plane: (●) Cu atoms and (×) O atoms.

0021-3640/04/7902-0088$26.00

the tunneling amplitude, which is known to be positive (see [1], p. 1004).

Let $\mathbf{a}_n$ ($n = x, y$) be the square-lattice periods directed from point 1 to point 2 and from point 1 to point 4, respectively. We have

$$\begin{aligned} H_{\text{eff}}|\mathbf{r}, \mathbf{r}+\mathbf{a}_x, \alpha\beta\rangle &= t(|\mathbf{r}+\mathbf{a}_x+\mathbf{a}_y, \mathbf{r}+\mathbf{a}_x, \alpha\beta\rangle \\ &+ |\mathbf{r}+\mathbf{a}_x-\mathbf{a}_y, \mathbf{r}+\mathbf{a}_x, \alpha\beta\rangle \\ &+ |\mathbf{r}, \mathbf{r}+\mathbf{a}_y, \alpha\beta\rangle + |\mathbf{r}, \mathbf{r}-\mathbf{a}_y, \alpha\beta\rangle) \\ &= t(-|\mathbf{r}+\mathbf{a}_x, \mathbf{r}+\mathbf{a}_x+\mathbf{a}_y, \beta\alpha\rangle \\ &+ |\mathbf{r}+\mathbf{a}_x-\mathbf{a}_y, \mathbf{r}+\mathbf{a}_x, \alpha\beta\rangle \\ &+ |\mathbf{r}, \mathbf{r}+\mathbf{a}_y, \alpha\beta\rangle - |\mathbf{r}-\mathbf{a}_y, \mathbf{r}, \beta\alpha\rangle), \end{aligned} \tag{3}$$

where we used the antisymmetry of quantities (1) with respect to arguments ($\mathbf{r}$, α) and ($\mathbf{r}'$, β). Analogously,

$$\begin{aligned} H_{\text{eff}}|\mathbf{r}, \mathbf{r}+\mathbf{a}_y, \alpha\beta\rangle &= t(-|\mathbf{r}+\mathbf{a}_y, \mathbf{r}+\mathbf{a}_x+\mathbf{a}_y, \beta\alpha\rangle \\ &+ |\mathbf{r}-\mathbf{a}_x+\mathbf{a}_y, \mathbf{r}+\mathbf{a}_y, \alpha\beta\rangle \\ &+ |\mathbf{r}, \mathbf{r}+\mathbf{a}_x, \alpha\beta\rangle - |\mathbf{r}-\mathbf{a}_x, \mathbf{r}, \beta\alpha\rangle). \end{aligned} \tag{4}$$

The complete set of localized states of an electron pair is determined by the state vectors

$$|\mathbf{r}, n, \alpha\beta\rangle \equiv |\mathbf{r}, \mathbf{r}+\mathbf{a}_n, \alpha\beta\rangle, \tag{5}$$

where $\mathbf{r}$ labels unit cells of the square lattice.

The problem obviously splits into two independent problems for singlet and triplet pairs that are characterized by quantities (5), respectively, antisymmetric and symmetric about the spin indices α, β. Assuming that the required stationary states of a pair are superpositions of localized states,

$$\sum_{\mathbf{r}, n} \psi^{(n)}_{\alpha\beta} e^{i\mathbf{k}\mathbf{r}} |\mathbf{r}, n, \alpha\beta\rangle, \tag{6}$$

with coefficients $\psi^{(n)}_{\alpha\beta}$ independent of $\mathbf{r}$ (this corresponds to a definite quasimomentum $\mathbf{k}$), we obtain

$$\begin{aligned} \epsilon(\mathbf{k})\psi^{(x)} &= t\psi^{(y)}(1 \pm e^{-i\kappa_x})(1 \pm e^{i\kappa_y}), \\ \epsilon(\mathbf{k})\psi^{(y)} &= t\psi^{(x)}(1 \pm e^{i\kappa_x})(1 \pm e^{-i\kappa_y}), \end{aligned} \tag{7}$$

where the upper or lower sign corresponds to a singlet or triplet state, respectively. The conditions for the existence of a nontrivial solution $\psi^{(x)}$, $\psi^{(y)}$ to system (7) defines the energy $\epsilon(\mathbf{k})$ of a paired quasiparticle, measured from the energy ϵ_0 of the initial localized state; $\kappa_x = \mathbf{k} \cdot \mathbf{a}_x$ and $\kappa_y = \mathbf{k} \cdot \mathbf{a}_y$. Everywhere in formulas (7), we omitted identical spin indices $\alpha\beta$.

The minimal energy $\epsilon_m = -4t$ of a singlet pair is attained for $\kappa_x = \kappa_y = 0$. The same minimal energy of a triplet pair is attained for a nonzero quasimomentum ($\kappa_x = \kappa_y = \pi$). This degeneracy is removed by taking into account the electron exchange in the initial localized pair. It is well known that this exchange is of an antiferromagnetic nature and, hence, singlet pairs possess the minimal energy.

Thus, solitary Bose quasiparticles can exist in the CuO_2 plane; these particles are characterized by a doubled electric charge and by zero momentum and spin in the ground state. It can readily be seen from Eqs. (7) that the effective mass of quasiparticles is $m = \hbar^2/ta^2$, where $a = |\mathbf{a}_x| = |\mathbf{a}_y|$. In addition, quasiparticles possess a specific quantum number $n = x, y$, which determines the orientation of a two-electron "dumbbell." Substituting $\epsilon = \epsilon_m$ into Eqs. (7), we obtain $\psi^{(x)} = -\psi^{(y)}$ in the ground state. Since orientations $n = x$ and $n = y$ are transformed into each other upon the lattice rotation through an angle of $\pi/2$ and upon the reflection in the diagonal plane passing through points 1 and 3 in the figure, the ground-state wave function $\psi \equiv \psi^{(x)} = -\psi^{(y)}$ of quasiparticles transforms in accordance with the 1D representation (usually denoted by $d_{x^2-y^2}$) of the symmetry group of CuO_2 plane (see [1]).

Superconductivity. We further assume that all other two-, three-, etc., electron configurations localized at distances on the order of atomic spacing are energetically disadvantageous as compared to the paired configuration considered above. In addition, we assume that electrons are repulsed at large distances such that the electron–electron interaction energy is on the order of the one-electron tunneling amplitude. Under these conditions, only one-electron Fermi particles and the paired Bose particles considered above play a significant role. The analysis carried out by Alexandrov and Kornilovitch in [6] shows that the conditions formulated above are likely to be realistic.

Finally, we assume that the minimal energy $\epsilon_0 + \epsilon_m$ of a paired quasiparticle is such that $(1/2)(\epsilon_0 + \epsilon_m)$ is within the one-electron energy band. In this case, upon an increase in the number of electrons at $T = 0$ (decrease in the hole-doping level), only one-electron quasiparticles are present and the system behaves as an ordinary Fermi liquid until $(1/2)(\epsilon_0 + \epsilon_m) > \epsilon_F$. The condition $(1/2)(\epsilon_0 + \epsilon_m) = \epsilon_F$ determines the minimal hole-doping level compatible with the state of a normal Fermi liquid. Denote by n_c the corresponding electron density n. Upon a further decrease in the hole-doping level, all additional $n - n_c$ electrons (we everywhere consider the case of small $n - n_c$ values, for which the concentration of pairs is low and their interaction can be disregarded) will pass into a Bose–Einstein (BE) condensate of paired quasiparticles. The system becomes a superconductor. The superconducting order parameter represents the boson ground-state wave function $\psi \equiv \psi^{(x)}$ normalized by the condition $|\psi|^2 = (n - n_c)/2$; wave function ψ transforms in accordance with the $d_{x^2-y^2}$ representation of the symmetry group of CuO_2 plane.

Properties of superconductors. It is important to note the following. In the system ground state (i.e., for

complete filling of all fermion states with an energy smaller than ϵ_F), the uncertainty in the energy of a boson quasiparticle with low excitation energy $\epsilon = k^2/2m$, arising due to its collisions with one-electron Landau quasiparticles, is proportional to ϵ^2. As in the conventional theory of Fermi liquid, this is due, first, to the fact that the density of fermions, which correspond to the vicinity on the order of ϵ near ϵ_F and with which the given boson can collide due to energy conservation, is low. Second, the statistical weight of the final states, to which fermionic transitions are possible, is small. The probability of boson decay into two fermions per unit time is also small as compared to ϵ, because of the limitations posed by the energy and momentum conservation. Thus, the proposed picture of superconductivity in the vicinity of maximal doping level remains valid even for an appreciable density of fermions, if the interaction between bosons and fermions is significant. The critical electron density n_c is determined from the condition that the electron chemical potential is equal to half of the minimal boson energy. In the general case, the latter is a functional of the distribution function for one-electron Landau quasiparticles.

In calculating the superconducting transition temperature, the fermion distribution function may be considered as corresponding to $T = 0$, since the temperature corrections (proportional to T^2) to the thermodynamic functions of Fermi liquid are considerably smaller than the corrections included below.

The density of noncondensed bosons at a finite temperature $T < T_c$ is

$$N' = \int \frac{2\pi k dk}{(2\pi\hbar)^2} \frac{1}{e^{\epsilon/T} - 1} = \frac{mT}{2\pi\hbar^2} \ln \frac{T}{\tau}. \quad (8)$$

The integral in Eq. (8) diverges at small ϵ, so that it is cut off at $\epsilon \sim \tau$, where τ is a small tunneling amplitude of an electron pair in the direction perpendicular to the CuO_2 plane.

The excess number $n - n_c$ of electrons in the system is equal to the doubled sum of N' and number N_0 of bosons in the condensate. This leads to the dependence of the superconducting transition temperature on the doping level for small values of $n - n_c$

$$n - n_c = \frac{mT_c}{\pi\hbar^2} \ln \frac{T_c}{\tau} \quad (9)$$

and the number of pairs in the condensate

$$N_0 = \frac{n - n_c}{2} \left(1 - \frac{T}{T_c} \frac{\ln T/\tau}{\ln T_c/\tau}\right), \quad (10)$$

which determines the modulus of order parameter $|\psi|^2 = N_0$ at finite temperatures. The superconducting transition temperature defined by Eq. (9) is quite high. To within the logarithmic term, this temperature is on the order of one-electron tunneling amplitude t at the boundary of the applicability region (i.e., for $n - n_c \sim a^{-2}$). The possibility that the superconducting transition temperature may have such an order of magnitude was pointed out in the aforementioned paper by Alexandrov and Kornilovitch [6].

The interaction of fermions with the BE condensate (effective electron–electron interaction) that is described by the order parameter ψ creates an effective potential $\Delta_{\mathbf{k}}$ acting on fermions as in conventional superconductors:

$$H_{\text{int}} = \sum_{\mathbf{k}} (\Delta_{\mathbf{k}} c^+_{\mathbf{k}\uparrow} c^+_{-\mathbf{k}\downarrow} + \text{h.c.}). \quad (11)$$

In view of the symmetry of ψ, we have

$$\Delta_{\mathbf{k}} = V(\hat{k}_x^2 - \hat{k}_y^2)\psi, \quad (12)$$

where $\hat{\mathbf{k}} = \mathbf{k}/|\mathbf{k}|$ and V is the invariant interaction constant.

Owing to this interaction, fermions in the superconducting state considered acquire features typical of an ordinary superconductor with the $d_{x^2-y^2}$ symmetry.

The total number of pairs at $T < T_c$ is independent of temperature and equal to $(n - n_c)/2$. As the temperature in the normal state increases ($T > T_c$), the number of pairs first decreases in proportion to $\ln T_c/(T - T_c)$ at $\tau \ll T - T_c \ll T_c$ and then increases at $T_c \ll T \ll t$ in proportion to T.

This study was supported by INTAS (grant no. 01-686), CRDF (grant no. RP1-2411-MO-02), Leverhulme Trust (grant no. S-00261-H), the Russian Foundation for Basic Research (grant no. 03-02-16401), and the President Program Supporting Leading Scientific Schools.

REFERENCES

1. C. C. Tsuei and J. R. Kirtley, Rev. Mod. Phys. **72**, 969 (2000).
2. T. Timusk and B. Statt, Rep. Prog. Phys. **62**, 61 (1999).
3. A. S. Alexandrov, Phys. Rev. B **48**, 10571 (1993).
4. V. Emery and S. Kivelson, Phys. Rev. Lett. **74**, 3253 (1995); Nature **374**, 434 (1995).
5. V. B. Geshkenbein, L. B. Ioffe, and A. I. Larkin, Phys. Rev. B **55**, 3173 (1997).
6. A. S. Alexandrov and P. E. Kornilovitch, J. Supercond. **15**, 403 (2002).
7. T. Domanski and J. Ranninger, Physica C (Amsterdam) **387**, 77 (2003).
8. A. F. Andreev, *Quantum Crystals*, in *Progress in Low Temperature Physics*, Ed. by D. F. Brewer (North-Holland, Amsterdam, 1982), Vol. 8, Sect. 4.4.
9. K. P. Sinha, Indian J. Phys. **35**, 434 (1961).

Translated by N. Wadhwa

JETP Letters, Vol. 79, No. 2, 2004, pp. 91–97. From Pis'ma v Zhurnal Éksperimental'noĭ i Teoreticheskoĭ Fiziki, Vol. 79, No. 2, 2004, pp. 104–110.

Comparative Study of ESR Spectra in Incommensurate Antiferromagnets¶

S. S. Sosin[1, *], L. A. Prozorova[1], and M. E. Zhitomirsky[2]

[1] *Kapitza Institute for Physical Problems, Russian Academy of Sciences, ul. Kosygina 2, Moscow, 117334 Russia*

[2] *Commissariat á l'Energie Atomique, DMS/DRFMC/SPSMS, 38054 Grenoble, France*

**e-mail: sosin@kapitza.ras.ru*

Received December 9, 2003

The electron spin resonance is studied for noncollinear low-dimensional antiferromagnets $RbMnBr_3$ and $RbFe(MoO_4)_2$ in a wide range of frequencies and fields. Both compounds have incommensurate spin structures appearing due to a low-symmetry distortion of an ideal hexagonal crystal lattice. Magnetic field applied in the spin plane induces a first-order transition into the commensurate phase. The low-energy resonance branch corresponding to a uniform oscillation of the spin system in the easy plane is observed in the two compounds in both incommensurate and commensurate phases, with a dramatic change of the spectra taking place near the transition field. The resonance spectrum of a nearly commensurate spin structure with long-wave modulations is analyzed in clean and dirty limits in the framework of a hydrodynamic approach. The resonance branch with steep field dependence in the incommensurate state is attributed to the acoustic mode with the gap resulted from pinning of local domain walls (discommensurations) on defects of the crystal structure. © *2004 MAIK "Nauka/Interperiodica".*

PACS numbers: 75.50.Ee; 76.50.+g

1. INTRODUCTION

Helical spin structures with incommensurate long-wavelength modulations is an interesting type of magnetic ordering [1]. They appear, generally, for two reasons: (i) when the symmetry of the crystal structure allows the Lifshitz invariant (of exchange or relativistic origin) or (ii) in the case of an "accidental" instability of a commensurate state due to competing exchange interactions. The compound $RbMnBr_3$ studied in this work belongs to the systems of the first type, while the origin of the low temperature incommensurate state in $RbFe(MoO_4)_2$ is still under debate.

The two materials crystallize into a hexagonal structure belonging to the same class of the point symmetry $\bar{3}m1$ (D_{3d}), space group $P6_3/mmc$ (D^4_{6h}) for $RbMnBr_3$ [2] (as for other ABX_3 systems) and $P\bar{3}m1$ (D^3_{3d}) for $RbFe(MoO_4)_2$, which undergoes phase transitions into different low-symmetry states on cooling. The crystal structure of $RbMnBr_3$ below $T_c = 220$ K is characterized by weak orthorhombic distortions with zigzags of magnetic ions shifted alternately up and down from the basal plane (space group *Pbca*) [3]. An incommensurate helical structure with magnetic Bragg peaks at $\mathbf{Q} = (h/8 + \xi, h/8 + \xi, l)$, where h and l are integers and $\xi = 0.0183 \pm 0.0004$, has been observed in the neutron scattering experiment below $T_N = 8.5$ K in zero magnetic field [4]. Microscopically, it can be described in terms of the row model assuming exchange interaction along zigzags to be somewhat different from those in other two in-plane directions [5, 6]. The initial high symmetry structure of $RbFe(MoO_4)_2$ also reveals distortions below $T_c = 180$ K [7], but the space group for this structure is not exactly determined. The ordered magnetic phase forming at $T_N = 3.8$ K appears to be an incommensurate helix with the wavevector $\mathbf{Q} = (1/3, 1/3, 0.41)$ [8]. Presumably, it results from inequality of the transversal exchange bonds between magnetic ions in neighboring planes.

Both structures have a strong easy-plane anisotropy keeping all spins inside the basal plane. Magnetic field applied in this plane gradually makes the incommensurate structure unfavorable and produces the first-order transition into the commensurate phase at $H_c \simeq 29$ kOe for $RbMnBr_3$ and 39 kOe for $RbFe(MoO_4)_2$. The resonance spectra of these multisublattice systems consist of several branches. Their distinct feature is the behavior of a low-energy acoustic branch, which corresponds to uniform oscillations of the spin system in the easy plane. For triangular antiferromagnets, it has a dependence $\nu \propto H^3$ valid until the exchange structure is weakly distorted by magnetic field. This branch has been observed in $RbMnBr_3$ only in the commensurate phase and disappeared below H_c [9]. Such an end point in $\nu(H)$ was explained by the appearance of the Goldstone mode related to spontaneous translational symmetry breaking in the incommensurate phase [10]. A similar resonance branch was found in $RbFe(MoO_4)_2$

¶ This article was submitted by the authors in English.

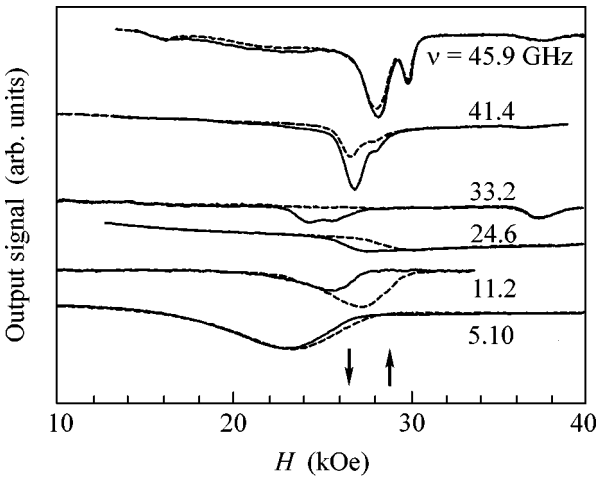

Fig. 1. Field dependence of the resonance absorption in $RbMnBr_3$ (T = 1.3 K); (dashed lines) forward field sweep, (solid lines) backward sweep; ↑ and ↓ mark the transitions for the forward and backward scans, respectively.

[11]. A finite frequency resonance mode can, however, be excited at the wavevector of incommensurate modulations. We have performed a search for such a low-energy mode starting from the frequency of 3 GHz. A new resonance branch has been found in the incommensurate phase with a very steep increase towards the transition field H_c. We also present theoretical calculations for the resonance in the incommensurate phase and discuss their relation to the observed branch.

2. EXPERIMENT

The Bridgman method was used to grow single crystals of $RbMnBr_3$. Samples 10–100 mm^3 in size were cut along binary planes (perpendicular to the basal plane of the crystal), so that one could easily orient them with respect to the magnetic field. The crystals of $RbFe(MoO_4)_2$ were grown from the flux. The resulting thin plates of 1–2 mm^3 had planes perpendicular to the C_3 axis.

We performed a series of electron spin resonance (ESR) measurements on single crystals of both compounds in a frequency range from 3.5 to 50 GHz. Three transmission-type spectrometers with various types of resonators (toroidal, rectangular, and cylindrical) were used in the experiment. Magnetic field up to 6 T was created by a cryomagnet. All experiments were carried out in a well-ordered antiferromagnetic phase at temperatures of 1.2–2.5 K significantly below the corresponding Néel temperatures.

The typical absorption lines in $RbMnBr_3$ for the magnetic field applied in the basal plane are shown in Fig. 1. The records were taken in both directions of the field sweep. At the lowest resonance line ν = 5.10 GHz (the low curve), the absorption appears to be almost without hysteresis, as the main part of the resonance line is far from the transition. On increasing the frequency, we approach the critical field and the hysteresis becomes more pronounced. The resonance exists below the transition and then sharply disappears at $H >$ 29 kOe. In the opposite direction, it is restored only at $H <$ 26.5 kOe, indicating the return to the incommensurate phase. These fields are marked by arrows in Fig. 1. Obviously, this means that the signal observed in the frequency range 5–20 GHz corresponds to the low field phase. Subsequently, this resonance absorption is replaced by singularities in the transmitted signal at the critical fields (ν = 24.6 GHz). The resonant signal is restored at higher frequencies with the inverse hysteresis. For example, at the frequency ν = 33.2 GHz, no signal is observed for a forward field sweep, while a resonance absorption reveals itself on the backward scan. Further increase in frequency allows one to detect a signal in both directions, with the hysteresis vanishing completely above ν = 46 GHz. In contrast to the low frequency signal, this resonance may obviously be attributed to the high field (commensurate) phase. This effect was first described in work [9] and was interpreted as an absence of an acoustic resonance mode until the transition into a commensurate spin structure [10].

The main difference with the previous results is that this branch at $H > H_c$ is split into two lines. The splitting results from orthorhombic distortions of the crystal structure removing degeneracy of the high symmetry hexagonal plane. Obviously, there should be three equivalent directions $\mathbf{x}_{1,2,3}$ (domains) of such distortions at an angle of 120° to each other. This weak anisotropy contributes to the potential energy of the spin system, thus originating the dependence of the AFMR frequency on the angles between $\mathbf{x}_i$ and the magnetic field. We have studied this effect in more detail by measuring the dependence of the resonance line in the large sample (containing all domains in roughly equal parts) on the direction of the magnetic field in the easy plane. The sample was initially oriented by one of the basal planes perpendicular to the field. In this orientation, one of the domains lies in the rational direction, while the other two deviate by ±60°. For this reason, two lines are observed with the relative intensity 1 : 2. Rotating the sample in the easy plane, one obtains the full picture including all three lines as shown in Fig. 2. Their angular dependences are shifted by ±60° to each other, as expected from the domain structure of the sample. The fits in the inset of Fig. 2 are harmonic functions with amplitudes determined by the value of the in-plane anisotropy.

Note that the resonance lines observed at low frequencies (5.10 GHz) demonstrate a strong temperature dependence most likely associated with the hyperfine interaction inside Mn^{2+} ions. The hyperfine interaction leads to hybridization of nuclear and electron spin resonance modes and to the appearance of the gap in the mixed spectrum $\nu^2 = \nu_e^2 + A/T$ (ν_e is the initial reso-

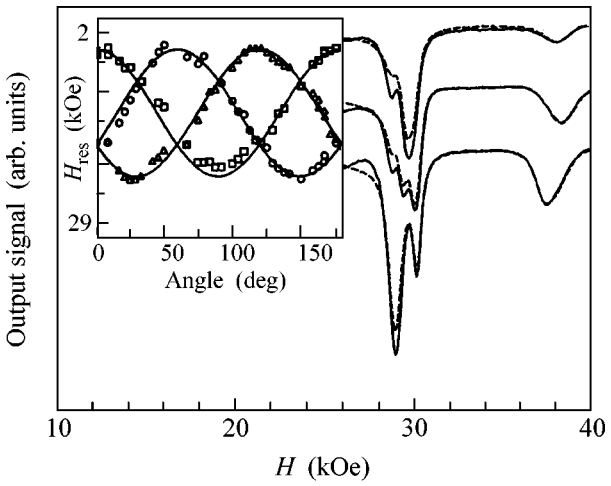

Fig. 2. Resonance absorption at ν = 44.7 GHz for three orientations of the crystal in the magnetic field (T = 1.3 K). Inset shows the angle dependence of the resonance field for each of the three domains; solid lines are sinusoidal fits (see text).

nance frequency; for similar compounds $CsMnBr_3$ and $CsMnI_3$, $A \sim 50$ GHz^2 K [12, 13]). On increasing the temperature by 0.5 K, the maximum of the absorption slides from 25 to 18 kOe, after which the line strongly broadens and disappears (see Fig. 3). The resonance at 3.47 and 7.11 GHz demonstrates qualitatively the same behavior, while, at other frequencies, it becomes almost temperature-independent in this range.

The low-frequency part of the resonance spectrum of $RbFe(MoO_4)_2$ was studied at T = 1.3 K (well below T_N = 3.8 K). The results obtained in the same frequency range as for $RbMnBr_3$ are represented in Fig. 4. The magnetic field was applied perpendicular to the C_3 axis. The spectrum in this frequency range consists of one low-energy relativistic and one high-energy exchange branch corresponding to the in-phase (as in $RbMnBr_3$) and out-of-phase oscillations of the spin planes, respectively. The intensity of the latter mode was very weak (one of the corresponding peaks is shown in Fig. 4 by the stroke, the other points are invisible in this scale).

The evolution of the acoustic resonance line on increasing the frequency is very similar to what has been observed in $RbMnBr_3$. Namely, there is a hysteresis in the absorption depending on the position of the resonance field at a given scan. At lower frequencies, the absorption corresponds to the low field phase and vice versa. In the intermediate range, the signal is replaced by nonresonance singularities at the transition fields 39.5 and 37.5 kOe for forward and backward scans, respectively (indicated by up and down arrows in Fig. 4). For the details of the high frequency part of the spectrum, see work [11].

3. THEORY

An incommensurate spin structure in a magnetic system with the Lifshitz invariant can be described by long-wavelength modulations of a commensurate state corresponding to a certain wavevector $\mathbf{k}_0$. In the case when a commensurate structure is noncollinear, a pair of orthogonal vectors $\mathbf{l}_1$ and $\mathbf{l}_2$ has to be used to describe both commensurate and incommensurate states:

$$\mathbf{S} \sim \mathbf{l}_1 \cos \mathbf{k}_0 \mathbf{r} + \mathbf{l}_2 \sin \mathbf{k}_0 \mathbf{r}. \quad (1)$$

The commensurate wavevector $\mathbf{k}_0 = (4\pi/3a, 0, \pi/c)$ appropriate for both compounds corresponds to a triangular 120° spin structure in the basal plane with antifer-

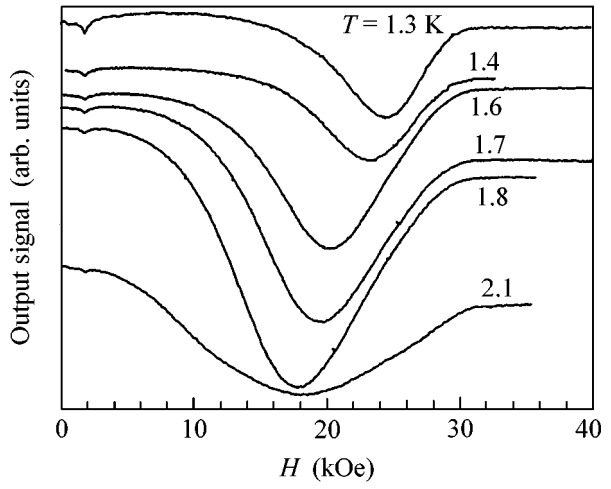

Fig. 3. Temperature dependence of the resonance absorption (forward field sweep) in $RbMnBr_3$ at ν = 5.10 GHz.

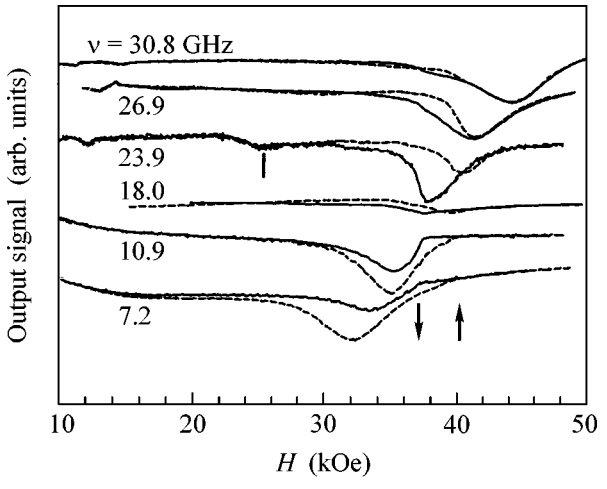

Fig. 4. Field dependence of the resonance absorption in $RbFe(MoO_4)_2$ at T = 1.3 K; (dashed lines) forward field sweep, (solid lines) backward sweep; ↑ and ↓ mark the transitions for the forward and backward scans, respectively.

romagnetically correlated layers giving six sublattices in total. Strong easy-plane anisotropy confines spins to the basal plane; hence, slow rotations of $\mathbf{l}_1$, $\mathbf{l}_2$ can be parameterized by an in-plane angle φ. In $RbMnBr_3$, such modulations propagate along the a axis, $\varphi(x)$, while for $RbFe(MoO_4)_2$, modulations are along the c axis, $\varphi(z)$. In the following, we denote the propagation direction of incommensurate modulations as x and write the corresponding hydrodynamic energy functional with the Lifshitz term in a general form [14] which is applicable to many other incommensurate systems:

$$E = \int dx\left[\frac{M}{2}(\partial_t\varphi)^2 + \frac{B}{2}(\partial_x\varphi)^2 - b(\partial_x\varphi) + A\cos n\varphi\right]. \quad (2)$$

Six sublattice antiferromagnets have a field induced anisotropy with $n = 6$ and $A \sim H^6$, while a weekly incommensurate two-sublattice antiferromagnet would have $n = 2$ and $A \sim H^2$. For vanishing anisotropy, the Lifshitz term stabilizes incommensurate sinusoidal modulations with $\varphi = bx/B$. Sufficiently strong anisotropy stabilizes commensurate domains with $\varphi = (\pi/n)(2m + 1)$. The transition into the commensurate state takes place when the energy of a single domain wall (also called soliton, kink, or discommensuration) of a width d

$$\varphi_s(x) = -\frac{\pi}{n} + \frac{4}{n}\arctan e^{x/d}, \quad d = \frac{1}{n}\sqrt{\frac{B}{A}}, \quad (3)$$

becomes positive. Such a lock-in transition occurs at the critical anisotropy

$$A_c = \frac{\pi^2 b^2}{16B}. \quad (4)$$

Below the lock-in transition, a static long-wavelength modulation of the $\mathbf{k}_0$ structure satisfies

$$\frac{B}{2A}(\partial_x\varphi)^2 = \frac{1}{\kappa^2} - 1 + \cos n\varphi \quad (5)$$

and has the form of a soliton lattice $\varphi_0(x) = (2/n)\mathrm{am}(x/d\kappa)$, where $\mathrm{am}(z)$ is the elliptic amplitude and κ is the modulus of the elliptic functions. The distance between solitons is $l = 2d\kappa K(\kappa)$, where $K(\kappa)$ ($E(\kappa)$) denote the complete elliptic integrals of the first (second) kind. Minimization of the energy of the soliton lattice yields

$$\frac{E(\kappa)}{\kappa} = \sqrt{\frac{A_c}{A}}, \quad (6)$$

which implicitly determines the field dependence of κ. For small anisotropy $A \ll A_c$, the soliton lattice transforms into a sinusoidal modulation with a period of $L = nl = (2\pi B/b)(1 + A^2B^2/2b^4)$, whereas, near A_c, the intersoliton distance grows logarithmically, $l = d\ln[8A_c/(A_c - A)]$.

The dynamics of the model Eq. (2) has been studied in many applications, e.g., for Josephson junctions [15] and for charge-density waves [16, 17]. The excitation spectrum is obtained in the linear approximation with respect to small oscillations $\varphi(x, t) = \varphi_0(x) + \psi(x, t)$. With $\psi(x, t) \sim e^{-i\Omega t}$, the equation of motion is reduced to the Lamé equation

$$\frac{d^2\psi}{dz^2} + \kappa^2\left[1 + \frac{\Omega^2}{\omega_c^2} - 2\mathrm{sn}^2(z)\right]\psi(z) = 0, \quad (7)$$

where $z = x/d\kappa$, $\omega_c^2 = n^2A/M$ is the resonance ($q = 0$) frequency in the commensurate state for vanishing incommensuration $b = 0$, and $\mathrm{sn}(z)$ is the elliptic sine. The general solution of the Lamé equation is given by [18]

$$\psi(z) = e^{Z(\alpha)z}\frac{H(z-\alpha)}{\Theta(z)}, \quad (8)$$

where $Z(u)$, $H(u)$, and $\Theta(u)$ are the Jacobi functions and α is an arbitrary parameter. The excitation energy Ω is related to a constant α as $\Omega = \omega_c\mathrm{dn}(\alpha)/\kappa$. An effective potential $2\mathrm{sn}^2(z)$ in Eq. (7) has a period of the intersoliton distance in rescaled units $l = 2K(\kappa)$. Using translational properties of the Jacobi functions $\Theta(u + 2K) = \Theta(u)$ and $H(u + 2K) = -H(u)$, one can show that solution (8) has the form of a Bloch wave with a quasimomentum

$$q = \frac{\pi}{2K(\kappa)} - iZ(\alpha). \quad (9)$$

The condition that propagating states have a real wavevector q specifies the allowed values for the parameter: $\alpha = iy + K(\kappa)$ and $\alpha = iy$ with $0 < y < K' = K(\kappa')$, $\kappa' = \sqrt{1-\kappa^2}$. The former branch is called the acoustic or soliton branch; it corresponds to $0 < q < \pi/l = \pi/2K$ and has $\Omega_s(0) = 0$, $\Omega_s(\pi/l) = \omega_c\kappa'/\kappa$. The latter optic or phason branch corresponds to $q > \pi/l$ and has $\Omega > \Omega_p(\pi/l) = \omega_c/\kappa$. Thus, the spectrum of (7) exhibits a jump at the first Brillouin zone boundary, remaining continuous for all other values of q. Using the series expansions [18]

$$Z(u) = \frac{2\pi}{K}\sum_{n=1}^{\infty}\frac{r^n}{1-r^{2n}}\sin\frac{n\pi u}{K},$$

$$\mathrm{dn}(u) = \frac{\pi}{2K} + \frac{2\pi}{K}\sum_{n=1}^{\infty}\frac{r^n}{1+r^{2n}}\cos\frac{n\pi u}{K} \quad (10)$$

with $r = \exp(-\pi K'/K)$, one can calculate spectrum in the incommensurate state for all values of anisotropy (magnetic field). At $A = A_c$, the soliton branch disappears, whereas the phason branch merges with the excitation spectrum in the commensurate state. The edge frequency of the phason branch, being a monotonically

increasing function of A, exhibits a universal ratio $\Omega_p(\pi/l)|_{A=0}/\Omega_p(\pi/l)|_{A=A_c} = 2/\pi$.

A weak uniform homogeneous microwave field polarized perpendicular to the direction of an applied field H generates a time-dependent force $f(t)\cos[n\varphi_0(x)]$ in the equation of motion of the phase variable $\psi(x, t)$. In the commensurate phase at $A > A_c$ when $\varphi_0(x) \equiv \pi/n$, such a force induces a conventional resonance at $\omega_c(A)$. Spatial harmonics, which can be excited by a uniform microwave field in the incommensurate state, are obtained by a Fourier decomposition of $\cos[n\varphi_0(x)] = 1 - 2\mathrm{sn}^2(z)$. They correspond to $q = 0, 2\pi/l, \ldots$. The acoustic branch has a Goldstone mode at $q = 0$ related to spontaneous breaking of translational symmetry by a soliton lattice. A finite frequency resonance can occur at the wavevector of incommensurate modulations $q^* = 2\pi/l$. The corresponding frequency $\Omega^p(q^*) = \omega_c\mathrm{dn}(iy^*)/\kappa$ has been calculated by numerically solving equation $Z(iy^*) = i\pi/2K$. The field dependence of $\Omega^p(q^*)$ is presented in Fig. 5. It is a monotonously decreasing function of field, which approaches the commensurate resonance frequency $\omega_c(A_c)$ at the lock-in transition with an infinite slope due to a logarithmic divergence of the intersoliton distance l. Similar to the edge frequency, a $q = 2\pi/l$ mode has a universal ratio $\Omega_p(q^*)|_{A=0}/\Omega_p(q^*)|_{A=A_c} = 4/\pi$. The flat behavior of $\Omega_p(q^*)$ as a function of h in a wide range of magnetic fields is explained by small deviations on an incommensurate helix from ideal sinusoidal modulations, which transform into a soliton lattice only in a narrow region near the lock-in transition. Close to H_c, the coupling strength of a microwave field to the corresponding spatial harmonics becomes, however, vanishingly small: $\int_0^l \cos[6\varphi_0(x)]e^{2\pi ix/l}dx/l \simeq d/l \sim 1/\ln(H_c - H)$. This confirms the conclusion of [10] about an abrupt termination of the resonance line in the commensurate state $\omega_c(H)$ at $H = H_c$. Away from H_c deep in the incommensurate state, a finite frequency resonance should reappear again, although an experimental observation of this line is hindered by its weak field dependence.

Various vacancies and crystal defects, which break translational symmetry of the lattice, should destroy the $q = 0$ Goldstone mode. Here, we propose a simple model to describe oscillations of individual solitons in a field of weak pinning potential in the limit $H \longrightarrow H_c$, where solitons are well separated from each other. The profile of a single soliton (3) is written as $\varphi_s(x - x_0)$, where $x_0(t)$ is a time-dependent soliton position. After taking the time derivative and subsequent spatial integration, the kinetic energy of a soliton is found to be

$$T = \frac{4M}{n^2 d}\left(\frac{dx_0}{dt}\right)^2. \qquad (11)$$

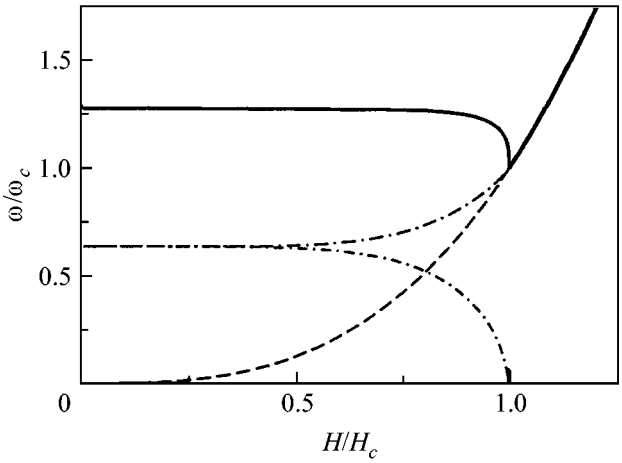

Fig. 5. Field dependence of various characteristic frequencies in the incommensurate state. Anisotropy in Eq. (2) is taken to be $A \sim H^6$. Solid lines are frequencies excited by a uniform microwave field. Dashed line is the resonance in the commensurate phase for $b = 0$. Dot-and-dash lines are the frequencies of the soliton (lower) and phason branches at the Brillouin zone boundary $q = \pi/l$.

We model a weak and local pinning potential by

$$U[\varphi_s(x)] = -Va_p^2\left(\frac{d\varphi_s}{dx}\right)^2\Bigg|_{x=0}, \qquad (12)$$

where $a_p \ll d$ is the characteristic spatial extension of the pinning center. In view of Eq. (5), the other possible form of the pinning energy as, e.g., $\sim\cos(n\varphi)$ is reduced to the above expression; however, it is difficult to exclude *a priori* presence of higher-order gradient terms as, e.g., $(d\varphi_s/dx)^4$. Equation (12) is easily transformed into

$$U(x_0) = \frac{4V^2a_p^2}{n^2d^2}\left(\tanh^2\frac{x_0}{d} - 1\right). \qquad (13)$$

The resonance frequency of small oscillations is

$$\Omega_s = \frac{2Va_p}{\sqrt{Md^3}} = 2Va_p\left(\frac{n^6A^3}{M^2B^3}\right)^{1/4}. \qquad (14)$$

The field dependence of the oscillation frequency is determined by field variations of the width of a domain wall and has a faster increase with magnetic field $\Omega_s \sim H^{9/2}$ than the commensurate resonance frequency $\omega_c \sim \sqrt{A} \sim H^3$. Due to the spread of characteristic pinning energies V, which depend on the microscopic structure of defects, the resonance at Ω_s should be observed as a broad line in the absorption spectrum. Note also that higher-order gradients in Eq. (12) produce a steeper increase of the oscillation frequency with magnetic field.

Finally, the microscopic row model [5, 6, 10] or the zigzag row model [3] can be used to derive the effective

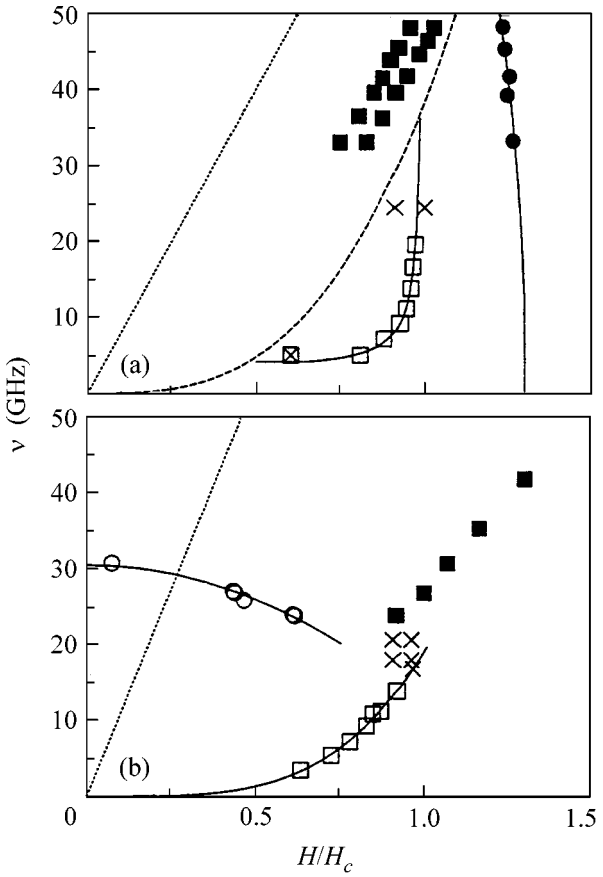

Fig. 6. Frequency–field diagram $\nu(H)$ of (a) $RbMnBr_3$ and (b) $RbFe(MoO_4)_2$ at $T = 1.3$ K; open and close symbols correspond to the resonance in the incommensurate and commensurate phases, respectively; (squares) the relativistic branch, (circles) the exchange mode, (×) nonresonant singularities; (⊠) resonance field at $T = 2.1$ K, (solid lines) see text, (dashed line) $\nu \propto H^3$ as in Fig. 5, (dotted line) a paramagnet with $\gamma = 2.8$ GHz/kOe.

hydrodynamic functional (2). We modify the previous analysis by introducing an additional in-plane anisotropy induced by an orthorhombic distortion in the form $D_1\Sigma(S_i^x)^2$. Then, the classical energy is expressed as a functional of in-plane angle φ:

$$E = \frac{\chi_\parallel}{2\gamma^2}(\partial_t\varphi)^2 + \frac{3}{4}J'a^2S^2(\partial_x\varphi)^2 - \sqrt{3}J'aS^2\delta\partial_x\varphi + \frac{\chi_\perp}{24H_e^4}(H^2 \pm H_{sf}^2)^3\cos 6\varphi, \quad (15)$$

where $\chi_\parallel = 2\chi_\perp = 1/8J$ are two principal components of the susceptibility tensor (J is the exchange constant inside chains), $\delta = J'/J_1' - 1$ is the relative change of the interchain exchange interaction, $H_e^2 = 48JJ'S^2$ is the field of a transition into the collinear phase, and $\gamma = g\mu_B/2\pi\hbar$ is the gyromagnetic ratio. Parameter $H_{sf}^2 = 16JD_1S^2$ denotes a field at which the magnetic energy becomes equal to the in-plane anisotropy energy. Signs "+" and "–" are chosen for $\mathbf{H} \parallel \mathbf{x}$ and $\mathbf{H} \perp \mathbf{x}$, respectively. The transition field of the commensurate–incommensurate transition in $RbMnBr_3$ is found from Eq. (4),

$$H_c = (\pi\delta)^{\frac{1}{3}}\sqrt{H_e^2 \pm H_{sf}^2}, \quad (16)$$

and the resonance frequency above the transition is given by the expression

$$\left(\frac{\omega}{\gamma}\right)^2 = \frac{3}{4H_e^4}(H \pm H_{sf})^6. \quad (17)$$

The value H_{sf} (and, consequently, D_1) can be estimated from the splitting of the relativistic branch above the transition. Taking the difference of the resonance fields at the utmost angles of rotation at a given frequency (see inset in Fig. 2), one obtains $H_{sf} \simeq \sqrt{H_{\rm res}\Delta H_{\rm res}} \simeq 7.5$ kOe. The value of the small in-plane anisotropy constant is estimated as $D_1 = (g\mu_B H_c)^2/16JS^2 \simeq 0.02$ GHz.

4. DISCUSSION

The results obtained in the experiment are summarized on two frequency–field diagrams (see Fig. 6). Two branches of the AFMR spectrum (exchange and relativistic) have been observed in each material in the experimental frequency range. The observed optic exchange modes have a different origin in the two compounds. In $RbMnBr_3$, such a mode appears due to the noncollinear spin structure and softens at the transition into the collinear phase $H = H_e \simeq 39$ kOe [9], while in $RbFe(MoO_4)_2$, an optic branch corresponds to uniform out-of-phase oscillations of weakly interacting neighboring spin planes [11]. Corresponding field dependences are shown in Fig. 6 by solid lines. Further, we shall discuss only the behavior of the relativistic branch.

First of all, one should note that the field dependences of the relativistic branches found in both structures are quite similar: steep increase of the gap in the incommensurate phase in the vicinity of the transition field followed by a jump to a commensurate resonance frequency. As the observed resonance mode at $H > H_c$ both in $RbMnBr_3$ and in $RbFe(MoO_4)_2$ is associated with the uniform oscillations of the spin system in the easy plane, one can also suggest this branch at $H < H_c$ to have the same nature in both compounds.

We can, however, exclude this interpretation on the basis of our theoretical calculations of the long-wave oscillation spectrum in the weakly modulated triangular spin system with the strong easy-plane anisotropy (see Fig. 5). The energy of the "phason" branch at the wavevector $q = 2\pi/l$ excited by a uniform SHF-field

decreases in magnetic field and is, in addition, practically dispersionless except for a small region near H_c. A similar mode has recently been observed in the collinear antiferromagnet CuB_2O_4 in one of the low-field phases which has a long-wave modulation of the spin structure [19]. At the same time, oscillations at $q = 0$ remain gapless because they correspond to uniform shifts of the whole soliton lattice at no energy cost.

We suggest a different interpretation of the observed resonance mode in the incommensurate states of both compounds. The field-increasing gap of the magnetic resonance may be attributed to the local domain walls at various defects of the crystal lattice (vacancies, dislocations, etc.). Local oscillations of domain walls have a characteristic frequency of $\nu(H) \sim H^{9/2}$ instead of a less steep dependence $\sim H^3$ usual for triangular antiferromagnets in weak magnetic fields. This is in qualitative agreement with the experimental result obtained for $RbFe(MoO_4)_2$: the guide-to-eye line in Fig. 6b fits the data by formula $\nu \sim (H/H_c)^4$, which agrees well with the exponent $n = 9/2$ suggested from the theoretical study. We find, however, a strong discrepancy with the experimental behavior of the resonance mode in $RbMnBr_3$. First, the observed field dependence is much steeper, $\sim H^n$, with $n = 10$–12, and second, it has a gap at $H = 0$ due to the hyperfine interaction in Mn^{2+} ions. Moreover, we have observed a strong temperature evolution of the resonance line in the temperature range 1.3–2.2 K (well below $T_N = 8.5$ K). On heating, the absorption maximum shifts to lower fields (see Fig. 3), which is unusual for field-increasing branches in the presence of a hyperfine gap reduced by temperature. Thus, the origin of the field and temperature-dependent gap of the acoustic resonance branch in $RbMnBr_3$ requires further discussion.

ACKNOWLEDGMENTS

The authors are grateful to V. Glazkov, V. Marchenko, A. Smirnov, and L. Svistov for useful discussions. The work of L.A.P. and S.S.S. was partially supported by the Russian Foundation for Basic Research (grant no. 04-02-17294). S.S.S. also thanks the National Science Support Foundation for financial help.

REFERENCES

1. I. E. Dzyaloshinskiĭ, Zh. Éksp. Teor. Fiz. **46**, 1420 (1964) [Sov. Phys. JETP **19**, 960 (1964)].
2. D. Visser, G. C. Verschoor, and D. J. W. Ijdo, Acta Crystallogr. B **36**, 28 (1980).
3. T. Kato, J. Phys. Soc. Jpn. **71**, 300 (2002).
4. L. Heller, M. F. Collins, Y. S. Yang, and B. Collier, Phys. Rev. B **49**, 1104 (1994).
5. W. Zhang, W. M. Saslow, and M. Gabay, Phys. Rev. B **44**, 5129 (1991); W. Zhang, W. M. Saslow, M. Gabay, and M. Benakli, Phys. Rev. B **48**, 10204 (1993).
6. M. E. Zhitomirsky, Phys. Rev. B **54**, 353 (1996).
7. S. A. Klimin, M. N. Popova, B. N. Mavrin, *et al.*, Phys. Rev. B **68**, 174408 (2003).
8. G. Gasparovic, M. Kenzelmann, C. Broholm, *et al.* (unpublished).
9. I. M. Vitebskii, O. A. Petrenko, S. V. Petrov, and L. A. Prozorova, JETP **76**, 178 (1993).
10. M. E. Zhitomirsky, O. A. Petrenko, and L. A. Prozorova, Phys. Rev. B **52**, 3511 (1995).
11. L. E. Svistov, A. I. Smirnov, L. A. Prozorova, *et al.*, Phys. Rev. B **67**, 094434 (2003).
12. I. A. Zaliznyak, N. N. Zorin, and S. V. Petrov, JETP Lett. **64**, 473 (1996).
13. L. A. Prozorova, S. S. Sosin, D. V. Efremov, and S. V. Petrov, JETP **85**, 1035 (1997).
14. I. E. Dzyaloshinskiĭ, Zh. Éksp. Teor. Fiz. **47**, 992 (1964) [Sov. Phys. JETP **20**, 665 (1965)].
15. P. Lebwohl and M. J. Stephen, Phys. Rev. **163**, 376 (1967); A. L. Fetter and M. J. Stephen, Phys. Rev. **168**, 475 (1968).
16. W. L. McMillan, Phys. Rev. B **16**, 4655 (1977).
17. V. L. Pokrovsky and A. L. Talapov, Sov. Phys. JETP **48**, 579 (1978).
18. E. T. Whittaker and G. N. Watson, *A Course of Modern Analysis* (Cambridge Univ. Press, London, 1963).
19. A. I. Pankrats, G. A. Petrakovskiĭ, M. A. Popov, *et al.*, Pis'ma Zh. Éksp. Teor. Fiz. **78**, 1058 (2003) [JETP Lett. **78**, 569 (2003)].

JETP Letters, Vol. 79, No. 2, 2004, pp. 98–99. Translated from Pis'ma v Zhurnal Éksperimental'noĭ i Teoreticheskoĭ Fiziki, Vol. 79, No. 2, 2004, pp. 111–112.

On the Origin of Ferromagnetism in Semiconducting $TiO_{2-\delta}$: Co Oxide

L. A. Balagurov[1], S. O. Klimonsky[1], S. P. Kobeleva[1], A. F. Orlov[1,*], N. S. Perov[2], and D. G. Yarkin[1]

[1] *State Research Institute for the Rare-Metal Industry "Giredmet," Moscow, 119017 Russia*
**e-mail: rmdp@girmet.ru*
[2] *Moscow State University, Moscow, 119899 Russia*
Received December 11, 2003

In Co-doped $TiO_{2-\delta}$ oxide films deposited on $SrTiO_3$(100) substrates, a room-temperature ferromagnetism is found to occur only in a limited charge-carrier concentration interval from 2×10^{18}–5×10^{22} cm^{-3}. This indirectly testifies that ferromagnetism in the aforementioned *n*-type semiconductor is associated with the exchange interaction of magnetic ions via conduction electrons rather than with the formation of Co clusters in the material. The magnetic moment per Co atom is $0.87\mu_B$ in the TiO cubic phase and $0.57\mu_B$ in the anatase tetragonal phase of TiO_2. © *2004 MAIK "Nauka/Interperiodica".*

PACS numbers: 75.70.Ak; 75.50.Pp; 75.60.Ej

The observation of ferromagnetism (FM) at room temperature in the anatase phase of $Ti_{1-x}Co_xO_2$ oxide [1, 2] has excited considerable interest in studying the properties of this semiconducting material because of its possible applications in spintronics. Later, a room-temperature FM was also observed in the rutile phase of this compound [3–5]. However, the origin of FM rise in these *n*-type semiconductors remains unclear. Some experimental data testify to the exchange mechanism of FM in a homogeneous material [6, 7], while other data suggest that the magnetic phase results from the formation of Co clusters [4, 5, 8, 9]. The revelation of the nature of FM in these materials is important in connection with the prospects of obtaining an effective spin polarization in them.

We studied the structure and magnetic properties of $Ti_{0.92}Co_{0.08}O_{2-\delta}$ (where $0 \le \delta \le 2$) films deposited on $SrTiO_3$(100) substrates by magnetron sputtering of an alloyed metal target in an argon–oxygen atmosphere with different partial oxygen pressures from 2×10^{-6} to 2×10^{-4} mm Hg. The temperature of the substrates during the sputtering process was 550°C, the film growth rate was 0.05–0.09 nm/s, and the film thickness was 0.2–0.3 μm.

The X-ray diffractometry of the resulting films showed that the films grown with a low partial oxygen pressure consisted of an amorphous metal phase. As the oxygen content in the gas mixture increased, polycrystalline films with a cubic TiO oxide structure were formed, and a further increase in the oxygen content led to the formation of tetragonal TiO_2 phases, namely, anatase and rutile. It is well known that the anatase and rutile phases are semiconductors with band gaps of 3.2 and 3.0 eV, respectively, and the TiO monoxide is an ionic crystal with metallic conductivity [10].

The figure shows the changes in the magnetic characteristics of $Ti_{0.92}Co_{0.08}O_{2-\delta}$ films, namely, the coercive force H_c and the remanent magnetization in zero magnetic field M_0 as functions of resistivity. Measurements were performed with a vibrating-coil magnetometer in a magnetic field up to 10 kOe directed along the film plane. At room temperature, the films exhibit ferromagnetic behavior with a pronounced magnetic hys-

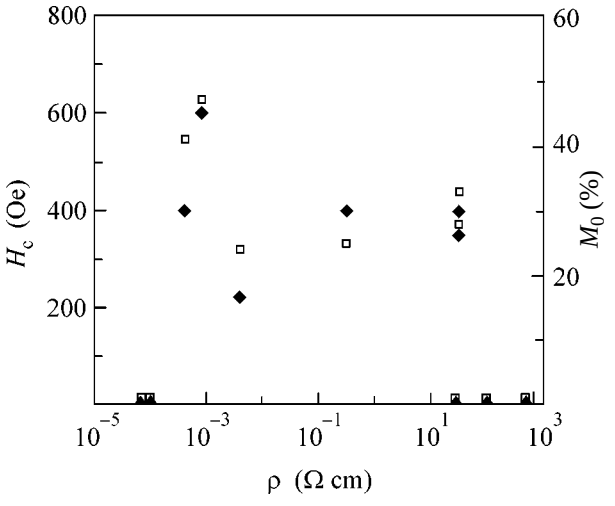

Coercive force H_c (◆) and remanent magnetization in zero magnetic field M_0 (□) of $Ti_{0.92}Co_{0.08}O_{2-\delta}$ films versus their resistivity ρ.

teresis loop that covers a resistivity range of more than four orders of magnitude. The magnetic moment calculated from the saturation magnetization is equal to $0.87\mu_B$ per Co atom in the TiO cubic phase and $0.57\mu_B$ in the anatase phase with compositions close to their stiochiometric values. As to the single-phase rutile samples, none of them were observed within the aforementioned range. From Hall measurements, we estimated the interval of charge-carrier concentrations within which the ferromagnetic phase was observed: the limiting values were found to be 2×10^{18} and 5×10^{22} cm^{-3}, respectively, for a charge-carrier mobility of 0.3 cm^2/(V s).

One should notice a sharp drop of magnetic characteristics to zero at the boundaries of the aforementioned resistivity range. Ferromagnetism is absent in both $Ti_{0.92}Co_{0.08}$ metal films and $Ti_{0.92}Co_{0.08}O_2$ high-resistance semiconductor films. This behavior of magnetic characteristics testifies to the exchange mechanism of FM in the material [11] rather than to the FM caused by the Co magnetic clusters. Indeed, photoelectron spectroscopy of the ferromagnetic samples showed that whole of cobalt was oxidized (the spectral line energy of Co $2p_{3/2}$ is 781.0 ± 0.5 eV). The value obtained for the magnetic moment per Co atom in the ferromagnetic films is much smaller than the corresponding value for metallic cobalt ($1.71\mu_B$). As a possible mechanism of the FM rise in an *n*-type $TiO_{2-\delta}$:Co semiconductor, Chambers [11] proposed the exchange interaction of magnetic Co ions via the conduction electrons corresponding to the excessive oxygen vacancies in the crystal lattice. The absence of FM in the metal phase of Ti–Co is presumably explained by the amorphization of the material.

In $Ti_{0.92}Co_{0.08}O_{2-\delta}$ films deposited on a Si(100) substrate, a weak FM was observed only near the resistivity of 1 Ω cm. In this case, the films were mainly amorphous with inclusions of anatase and rutile phases.

We are grateful to Yu.B. Patrikeev for preparing the targets for magnetron sputtering and to O.P. Sideleva for testing the film composition by local X-ray spectroscopy.

REFERENCES

1. Y. Matsumoto, M. Murakami, T. Shono, *et al.*, Science **291**, 854 (2001).
2. S. A. Chambers, S. Thevuthasan, R. F. C. Farrow, *et al.*, Appl. Phys. Lett. **79**, 3467 (2001).
3. W. K. Park, R. J. Ortega-Hertogs, J. S. Moodera, *et al.*, J. Appl. Phys. **91**, 8093 (2002).
4. A. Punnoose, M. S. Seehra, W. K. Park, and J. S. Moodera, J. Appl. Phys. **93**, 7867 (2003).
5. P. A. Stampe, R. J. Kennedy, Yan Xin, and J. S. Parker, J. Appl. Phys. **93**, 7864 (2003).
6. J. R. Simpson, H. D. Drew, S. R. Shinde, *et al.*, cond-mat/0205626 (2002).
7. T. Fukumura, Y. Yamada, K. Tamura, *et al.*, Jpn. J. Appl. Phys. **42**, L105 (2003).
8. S. A. Chambers, T. Droubay, C. M. Wang, *et al.*, Appl. Phys. Lett. **82**, 1257 (2003).
9. J. Y. Kim, J. H. Park, B. J. Park, *et al.*, Phys. Rev. Lett. **90**, 017401 (2003).
10. T. Suzuki and R. Souda, Surf. Sci. **445**, 506 (1999).
11. S. A. Chambers, Mater. Today **5** (4), 34 (2002).

Translated by E. Golyamina